

# Stretchable metallization technologies for skin-like transducers

THÈSE N° 7848 (2017)

PRÉSENTÉE LE 6 OCTOBRE 2017

À LA FACULTÉ DES SCIENCES ET TECHNIQUES DE L'INGÉNIEUR  
CHAIRE FONDATION BERTARELLI DE TECHNOLOGIE NEUROPROSTHÉTIQUE  
PROGRAMME DOCTORAL EN MICROSYSTÈMES ET MICROÉLECTRONIQUE

ÉCOLE POLYTECHNIQUE FÉDÉRALE DE LAUSANNE

POUR L'OBTENTION DU GRADE DE DOCTEUR ÈS SCIENCES

PAR

**Hadrien Olivier MICHAUD**

acceptée sur proposition du jury:

Prof. M. Gijs, président du jury  
Prof. S. Lacour, directrice de thèse  
Prof. M. Dickey, rapporteur  
Prof. I. Graz, rapporteuse  
Prof. F. Sorin, rapporteur



ÉCOLE POLYTECHNIQUE  
FÉDÉRALE DE LAUSANNE

Suisse  
2017



Hâtez-vous lentement, et sans perdre courage,  
Vingt fois sur le métier remettez votre ouvrage  
— Nicolas Boileau, *L'Art poétique*



# Acknowledgements

Many persons made my journey to the PhD extremely fruitful not only on a scientific standpoint, but also more importantly on the personal side.

First and foremost, I would like to acknowledge Prof. Stéphanie Lacour who gave me the chance to start and conduct my research in first-class conditions. I deeply acknowledge her scientific advice, decisive support, trust, and genuinely optimistic and curious nature.

I am also grateful to Prof. Michael Dickey, Prof. Ingrid Graz and Prof. Fabien Sorin for accepting to be the examiners of my work, and to Prof. Martinus Gijs for accepting to preside the jury.

Next, I would like to thank my colleagues at the Laboratory for Soft Bioelectronic interfaces with whom I had the chance to collaborate, which included debugging projects, sharing desperation and eureka moments, brainstorming, and correcting typos. First was Aaron: working with you was an extremely formative experience as a student, thank you for sharing your insights and high quality standards. Then came Arthur who embarked me in one of his crazy "rock 'n'roll" concepts, for the best of course. I hope to continue the adventure with both of you. Next in line was Laurent whose contribution was fundamental in obtaining rapid results for the epidermal strain sensors. Your patience during the diverse recording sessions was much welcomed.

I would like to thank all the others who worked in the lab with me, including those who came before and did a lot to set-up the laboratory in Lausanne: Alessia, Kate, Amélie, Ivan M., Cédric, Tero, Douglas, and Anna. And those who came after and, for some of them, worked hard to transfer the lab to Geneva in the best conditions possible: Sandra, Fred, Swati, Nicolas, Alba, Yi-Lin, Jennifer, Giuseppe, Aaron L., Florian, Ivan F, Liz, and Michael. Of course there was more than work during these four years and the CNP retreats, snowshoe sessions, after-work drinks and lakeside BBQs will remain superb memories; and the California road-trip with Aaron, Arthur and Ivan was a once-in-a-lifetime experience.

I'm seriously indebted to all the staff from the EPFL Center for MicroNanoTechnologies (CMi) who, since my first days there in 2011, constantly helped me in experimenting new processes and are maintaining a renowned know-how in microfabrication. I also warmly thank Mickaël Stoeckel and Anthony Guillet from the Wyss Center for Bio and Neuroengineering for deliver-

## Acknowledgements

---

ing a top-class cleanroom at the Campus Biotech in Geneva.

I would also like to thank all my colleagues from the WiseSkin collaboration with whom I add the chance to work on a truly ambitious multidisciplinary project: Eleni Daskalaki, Jacek Baborowski, Oleksandr Vorobyov, and John Farserotu from CSEM, Huaqi Huang, Tao Li and Prof Volker Koch from BFH, Camillo Rojas and Prof Jean-Dominique Decotignie from CSEM/EPFL-LAMS, and Vladimir Kopta and Prof Christian Enz from EPFL-ICLALAB.

I am grateful to Nicolas Sommer and Prof Aude Billard from EPFL-LASA for helping me access to and use the iCub robot, Prof Silvestro Micera from EPFL-TNE for giving access to the Vicon system, and to Prof Paul Muralt from EPFL-LC for the use of the diffraction machine. I also warmly welcomed the help of Dr Claudia Baumgartner from Unil, and Blaise Rubinstein and Jakob Mallmann from Olympus who organized the measurement session with the confocal laser microscope. I acknowledge Mikaël Sturny from EPFL-LHTC for graciously machining the first version of the POM molds, and Roland Dupuis from the EPFL Additive Manufacturing Workshop for his expertise and availability.

I also acknowledge Raphael Daimel and Prof Oliver Brock from TU Berlin for their warm welcome there. I sincerely hope that sensors from EPFL will one day equip your robotic hand!

Of course, I would like to express my gratitude to all the students I supervised for their genuine enthusiasm and their hard work: Joan Teixidor, Laurent Dejace (again), Séverine de Mulatier, Carlos Senz Caldero and Carlos Nunez.

EPFL and Lausanne were not just about work, thanks to Thomas who was always up for a lunch or a concert, Katilin for a power session in Rocspot or the Cube (and a lot of proofreading!), Clémentine and Bruno for a drink, a dinner or a football game. I also had the chance to share some memorable moments in the mountains with Nico who took me as his rope partner in spite of my comparatively ridiculous climbing abilities. Last but not least, I'm seriously indebted to Robin for his material science and fashion insights (among other things) all along the two years we've shared a flat: *ipsa scientia potestas est*.

Now comes the moment to go back in time and thank the friends with whom I had the chance to sit at the university, high-, middle-, and even elementary school and thus contributed (sometimes very indirectly I must say) to my education: "la Famille" from Polytechnique with Cyril, Jef, Marc, Pierre, Thomas and Jean-Eudes, and the (future) doctors Matthieu, Julien and Robin; "les HX4" from Lycée du Parc, with Pierre-Benoît, Claire, Yohan, Camille, Gauthier, Stéphane, Pierre; "les Culoziens", with Guillaume, Alex, Nico, Loïc and Lilian.

And at the origin was my family. I would like to express all my gratitude to my grandparents Gabrielle, Jeanne, Robert and Marcel. Je ne mesure pas la chance de vous avoir tous. I also thank my brothers Xavier and Laurent for all the wonderful moments we have lived together,

## **Acknowledgements**

---

in the cities and into the wild. I'm finally extremely thankful to my mother Nicole and my father Jean-Marie for their loving support through the years, during the ups and during the downs. Merci!

Finally, I don't have words strong enough to express my profound gratitude and affection to Martina for her constant love and support: you turn complexity into simplicity, anxiety into serenity, and quietly revolutionize my life. Sei il sale della mia vita.

*Geneva, July 2017*

H. M.





# Abstract

The skin is the largest human organ, capable of accomplishing distributed and multimodal sensing functions. Replicating the versatility of skin artificially is a significant challenge, not only in terms of signal processing but also in mechanics. Stretchable electronics are an approach designed to cover human and artificial limbs and provide wearable sensing capabilities: motion sensors distributed on the hand of neurologically impaired patients could help therapists quantify their abilities; prostheses equipped with multiple tactile sensors could enable amputees to naturally adjust their grasp force.

Skin-like electronic systems have specific requirements: they must mechanically adapt to the deformations imposed by the body they equip with minimal impediment to its natural movements, while providing sufficient electrical performance for sensor transduction and passing electrical signals and power. A metallization ensuring stable conductivity under large strains is a prerequisite to designing and assembling wearable circuits that are integrated with several types of sensors.

In this work, two innovative metallization processes have been developed to enable scalable integration of multiple sensing modalities in stretchable circuits.

First, stretchable micro-cracked gold (Au) thin films were interfaced with gallium indium eutectic (EGaIn) liquid metal wires. The Au films, thermally evaporated on silicone elastomer substrates, combined high sheet resistance (9 to 30  $\Omega$ /sq) and high sensitivity to strain up to 50%. The EGaIn wires drawn using a micro-plotting setup had a low gauge factor (2) and a low sheet resistance (5 m $\Omega$ /sq).

Second, a novel physical vapor deposition method to deposit of thin gallium-based biphasic (solid-liquid) films over large areas was achieved. The obtained conductors combined a low sheet resistance (5  $\Omega$ /sq), a low gauge factor (1 up to 80% strain), and a failure strain of more than 400%. They could be patterned down to 10  $\mu$ m critical dimensions.

Skin-like sensors for the hand were assembled using the two processes and their capabilities were demonstrated. Thin (0.5 mm) silicone strips integrating EGaIn wires and micro-cracked Au strain gauges were mounted on gloves to encode the position of a biomimetic robotic finger and a human finger. In combination with soft pressure sensors, they enabled precise grasp

## Acknowledgements

---

analysis over a limited range of motion. Then, biphasic films were micro-patterned on silicone to assemble 50  $\mu\text{m}$  thin epidermal strain gauges. The strain gauges were attached on a user's finger and accurately encoded fine grasping tasks covering most of the human hand range of motion. The films were also used to power wireless MEMS pressure sensors integrated in a rubber scaffold. The device was mounted on a prosthetic hand to encode normal forces in the 0 N to 20 N range with excellent linearity.

The epidermal strain sensors are currently being used to quantify the tremors of patients with Parkinson's disease. In the future, the unique properties of the biphasic films could enable advanced artificial skins integrating a high density of soft transducers and traditional high-performance circuits.

Key words: electronic skin, stretchable conductors, thin films, liquid metals, gallium, strain gauges, motion sensing, prosthesis, robotic hands, wearable transducers.

# Résumé

La peau n'est pas seulement l'organe le plus étendu mais remplit aussi des fonctions sensorielles multimodales et distribuées. Reproduire artificiellement ces capacités est un défi considérable, non seulement en terme de traitement du signal, mais aussi en terme de mécanique. Les circuits électroniques étirables sont conçus pour couvrir des membres humains ou artificiels et offrir des capacités sensorielles portables : des capteurs de mouvement distribués sur la main de patients neurologiquement diminués pourraient aider les thérapeutes à quantifier leurs capacités; des prothèses équipées de multiples capteurs tactiles pourraient permettre aux amputés d'ajuster leur force de façon naturelle.

Les peaux électroniques ont des prérequis spécifiques : elles doivent s'adapter mécaniquement aux déformations imposées par le corps qu'elles équipent sans affecter ses mouvements, tout en fournissant des performances électriques suffisantes pour capter et transmettre des signaux électriques. Une métallisation garantissant une conductivité stable sous de grandes déformations est un prérequis pour concevoir et assembler des circuits portables intégrant divers capteurs.

Deux processus de métallisation innovants ont été développés pour permettre l'intégration à grande échelle de multiples capteurs dans des circuits étirables.

Des couches minces d'or micro-fracturées ont d'abord été interfacées avec des fils de métal liquide formés de l'alliage eutectique de gallium et d'indium (EGaIn). Les couches d'or évaporées thermiquement sur des substrats de silicone possédaient une grande résistivité (de 9 à 30  $\Omega$ /carré) et une grande sensibilité à la déformation. Les fils d'EGaIn déposés à l'aide d'un dispositif de micro-traçage avaient un faible facteur de jauge (2) et une faible résistivité (0.5 m $\Omega$ /carré).

Puis une nouvelle méthode pour déposer des couches minces biphasiques (solides-liquides) à base de gallium par dépôt physique en phase vapeur a été introduite. Les conducteurs obtenus possédaient à la fois une faible résistivité (0.5  $\Omega$ /carré), un faible facteur de jauge (1 jusqu'à 80% de déformation), et un allongement à la rupture supérieur à 400%. Ils ont été définis jusqu'à une dimension critique de 10  $\mu$ m.

Des capteurs pour la main ont été assemblés en utilisant les deux procédés et testés fonction-

## Résumé

---

nellement. De fines (0.5 mm d'épaisseur) bandes de silicone intégrant des fils en EGalN et des jauges de déformation en or micro-fracturé ont été montées sur des gants pour encoder la position de doigts robotiques et humains. Combinées à des capteurs de pressions, elles ont permis une analyse précise de la préhension dans une gamme de mouvements limitée. Ensuite, les couches biphasiques ont été micro-structurées sur silicone pour assembler des jauges de déformation épidermiques de 50  $\mu\text{m}$  d'épaisseur. Les jauges ont été attachées sur le doigt d'un utilisateur pour encoder avec précision des gestes couvrant une large gamme de mouvements. Les couches minces biphasiques ont également été utilisées pour alimenter des capteurs de pression MEMS intégrés dans une structure en silicone. Le dispositif a été monté sur une prothèse de main pour encoder des forces normales entre 0 N et 20 N avec une excellente linéarité.

Les jauges de contrainte épidermiques sont actuellement utilisées pour quantifier les tremblements de patients atteints de la maladie de Parkinson. À l'avenir, les propriétés uniques des couches biphasiques pourraient permettre de produire des peaux artificielles intégrant une grande densité de capteurs étirables et de circuits traditionnels haute performance.

Mots clefs : peau électronique, conducteurs étirables, couches minces, métaux liquides, gallium, jauges de déformation, capteurs de mouvement, prothèses, mains robotiques, transducteurs.

# Contents

<b>Acknowledgements</b>	<b>i</b>
<b>Abstract (English/Français)</b>	<b>v</b>
<b>List of figures</b>	<b>xiii</b>
<b>List of tables</b>	<b>xvii</b>
<b>Introduction</b>	<b>1</b>
<b>1 Specifications, technologies, and selected applications for skin-like transducers</b>	<b>7</b>
1.1 Specifications for skin-like electronic transducers . . . . .	7
1.1.1 Motivation . . . . .	7
1.1.2 Mechanical specification . . . . .	7
1.1.3 Electrical specifications . . . . .	8
1.1.4 Process specification . . . . .	8
1.1.5 Conclusion . . . . .	8
1.2 Basic components for skin-like electronic transducers . . . . .	8
1.2.1 Motivation . . . . .	8
1.2.2 Substrate material . . . . .	8
1.2.3 Stretchable electronic conductors . . . . .	10
1.2.4 Conclusion . . . . .	13
1.3 Skin-like motion and tactile transducers for the hand . . . . .	14
1.3.1 Motivation . . . . .	14
1.3.2 The human hand . . . . .	14
1.3.3 Hand motion encoding . . . . .	15
1.3.4 Tactile sensing for the hand . . . . .	16
1.3.5 Conclusion . . . . .	18
1.4 Summary and outlook . . . . .	18
<b>2 Stretchable conductors from thin metal films and liquid metals</b>	<b>19</b>
2.1 Electro-mechanical characterization of stretchable micro-cracked gold films on PDMS . . . . .	20
2.1.1 Motivation . . . . .	20

## Contents

---

2.1.2	Evaluation of the gauge factor . . . . .	21
2.1.3	Evaluation of sensitivity to strain direction . . . . .	24
2.1.4	Conclusion . . . . .	25
2.2	Liquid metal micro-plotting . . . . .	26
2.2.1	Motivation . . . . .	26
2.2.2	Deposition and characterization of micro-plotted wires . . . . .	27
2.2.3	Connection of micro-plotted EGaIn wires to micro-cracked Au tracks . . . . .	29
2.2.4	Conclusion . . . . .	31
2.3	Gallium-based biphasic (liquid-solid) and intrinsically stretchable thin films . . . . .	32
2.3.1	Motivation . . . . .	32
2.3.2	Growth of the films . . . . .	32
2.3.3	Electromechanical characterization . . . . .	40
2.3.4	Micro-patterning . . . . .	47
2.3.5	Investigation of other solid metallic under-layers . . . . .	50
2.3.6	Liquid electromigration under DC current in biphasic thin films . . . . .	53
2.3.7	Conclusion . . . . .	58
2.4	Summary and outlook . . . . .	59
2.5	Contributions . . . . .	62
<b>3</b>	<b>Skin-like strain sensors from stretchable conductors</b>	<b>63</b>
3.1	Liquid metal wires and microcracked gold thin films for robotic hand motion encoding . . . . .	64
3.1.1	Motivation . . . . .	64
3.1.2	Design and fabrication of the sensors . . . . .	64
3.1.3	Results and discussion . . . . .	66
3.1.4	Conclusion . . . . .	70
3.2	Liquid metal wires and microcracked gold thin films for motion encoding on a glove . . . . .	71
3.2.1	Motivation . . . . .	71
3.2.2	Design and fabrication of the sensors . . . . .	71
3.2.3	Characterization . . . . .	71
3.2.4	Coupling with soft-pressure sensor for grasp encoding . . . . .	74
3.2.5	Conclusion . . . . .	78
3.3	Epidermal strain sensors from biphasic thin films . . . . .	79
3.3.1	Motivation . . . . .	79
3.3.2	Design and fabrication of the sensors . . . . .	79
3.3.3	Response to uni-axial strain, normal force, and temperature variation . . . . .	80
3.3.4	Benchmarking as finger tracking sensors . . . . .	82
3.3.5	Comparison with the video-tracking system during grasping tasks . . . . .	84
3.3.6	Conclusion . . . . .	88
3.4	Combining micro-cracked gold and micro-plotted liquid metal wires for skin-like multidirectional strain sensors . . . . .	89

3.4.1	Motivation . . . . .	89
3.4.2	Design and fabrication of the sensors . . . . .	89
3.4.3	Detection of uniaxial strain magnitude and orientation . . . . .	90
3.4.4	Detection of isotropic strain magnitude . . . . .	91
3.4.5	Conclusion . . . . .	93
3.5	Summary and outlook . . . . .	94
3.6	Contributions . . . . .	94
<b>4</b>	<b>Tactile sensors and micro-heaters with biphasic film metallization</b>	<b>97</b>
4.1	Powering miniaturized wireless sensor nodes . . . . .	98
4.1.1	Context and motivation for the study . . . . .	98
4.1.2	Materials and methods . . . . .	99
4.1.3	Results and discussion . . . . .	102
4.1.4	Conclusion . . . . .	103
4.2	Skin-like resistive micro-heaters array . . . . .	105
4.2.1	Context and motivation for the study . . . . .	105
4.2.2	Materials and methods . . . . .	105
4.2.3	Results and discussion . . . . .	106
4.2.4	Conclusion . . . . .	108
4.3	Summary and outlook . . . . .	108
4.4	Contributions . . . . .	108
<b>5</b>	<b>Conclusion</b>	<b>109</b>
5.1	Summary and impact of the contribution . . . . .	109
5.1.1	Stretchable metallization technologies . . . . .	109
5.1.2	Skin-like sensors . . . . .	110
5.2	Future perspectives and challenges . . . . .	111
5.2.1	Technological improvements . . . . .	111
5.2.2	Future applications for stretchable motion and tactile sensors . . . . .	112
5.2.3	From discrete sensors to distributed network . . . . .	113
5.2.4	Industrialization . . . . .	113
<b>Appendix</b>		<b>117</b>
A.1	Detailed fabrication methods . . . . .	117
A.1.1	Micro-cracked gold thin films deposition on PDMS . . . . .	117
A.1.2	EGaIn wires micro-plotting . . . . .	117
A.1.3	Biphasic gallium based thin film deposition and patterning . . . . .	118
A.2	Four point probe measurement . . . . .	120
A.3	Calibration of the gallium thermal evaporator. . . . .	121
A.4	Methodology and additional data for determination of biphasic film thickness	123
A.5	Additional plot for electromigration study in biphasic films . . . . .	125
A.6	Calculation of joints' angles using the camera tracking system . . . . .	126
A.7	Determination of orientation angle in the rosette configuration . . . . .	127

## Contents

---

A.8 Thermal coefficient of resistance (TCR) of the biphasic thin films . . . . .	128
<b>Bibliography</b>	<b>144</b>
<b>Glossary</b>	<b>145</b>
<b>Curriculum Vitae</b>	<b>147</b>



# List of Figures

I.1	Young's moduli of human tissues. . . . .	2
I.2	Mechanoreceptors and proprioceptors in the human skin. . . . .	3
I.3	Examples of application for skin-like transducers. . . . .	4
1.1	Scale of motion for reversible strain accomodation in various stretchable electronic conductors. . . . .	11
1.2	Anatomy of the human hand. . . . .	14
1.3	Example of a commercially available wearable motion sensing sensing for the hand. . . . .	15
1.4	Example of a available tactile sensing systems for the hand. . . . .	17
2.1	SEM picture of the surface of micrco-cracked gold thin films deposited on PDMS. . . . .	20
2.2	Sample fabrication to evaluate the gauge factor of stretchable micro-cracked film . . . . .	21
2.3	Set-up for gauge factor measurements. . . . .	22
2.4	SEM images of micro-cracked Cr/Au surface for various deposited Au thicknesses . . . . .	23
2.5	Sheet resistance and gauge factor of micro-cracked gold thin films . . . . .	23
2.6	Sensitivity to strain direction for micro-cracked Cr/Au thin films . . . . .	24
2.7	EGaIn microwires plotting set-up. . . . .	26
2.8	Characterization of micro-plotted EGaIn wires . . . . .	28
2.9	Electro-mechanical characterization of micro-plotted EGaIn wires . . . . .	29
2.10	Connection between microplotted EGaIn wires and micro-cracked gold traces . . . . .	30
2.11	Diffusion of EGaIn into micro-cracked gold traces . . . . .	31
2.12	Process flow for the deposition of gallium-based biphasic thin films . . . . .	33
2.13	Thermal evaporation of gallium on bare and gold-coated PDMS substrates . . . . .	34
2.14	Growth of biphasic gold-gallium thin films on a PDMS membrane . . . . .	35
2.15	X-Ray diffraction analysis of biphasic gold-gallium thin film . . . . .	36
2.16	EDS-SEM analysis of the gold-gallium films . . . . .	37
2.17	SEM picture of the cross-section of the SEM of the biphasic gold-gallium films on a PDMS substrate. . . . .	38
2.18	Topography of a biphasic film track. . . . .	39
2.19	Samples and setup for electromechanical characterization of biphasic thin films. . . . .	41
2.20	Relative change in electrical resistance as a function of applied engineering strain $\epsilon$ of biphasic conductive tracks . . . . .	41

## List of Figures

---

2.21 SEM images of the surface of biphasic gold-gallium thin films prepared with atomic ratio $\beta$ of 3.9 and 13 on PDMS substrates. . . . .	43
2.22 Initial sheet resistance, gauge factor, and relative change in electrical resistance after cycling to 0.5 maximum applied strain for increasing $\beta$ ratios . . . . .	44
2.23 Fatigue test for the biphasic gold-gallium thin films . . . . .	44
2.24 Test to very large ( $>2$ ) strains for the biphasic gold-gallium thin films . . . . .	45
2.25 Radial stretching of the biphasic gold-gallium thin films conductors on a PDMS substrate . . . . .	46
2.26 Micropatterning of biphasic gold-gallium conductors on PDMS substrates with lift-off processing . . . . .	48
2.27 3D reconstruction of micro-patterned biphasic gold-gallium tracks from optical profilometer measurement . . . . .	48
2.28 Electromechanical characterization of micro-patterned biphasic gold-gallium tracks . . . . .	49
2.29 Biphasic gallium-based thin films on PDMS substrates with Au, Pd, Pt and Ir underlayers . . . . .	51
2.30 Electromechanical characterization of biphasic films with Au, Pd, Pt and Ir underlayers . . . . .	52
2.31 Test set-up for liquid electro-migration measurement. . . . .	54
2.32 Resistance of test tracks as a function of time and failure time as a function of DC current. . . . .	55
2.33 Biphasic film aspect before and after electrical failure. . . . .	56
2.34 EDS-SEM analysis of the cathode and anode areas after failure . . . . .	57
2.35 SEM image of the metallic clusters . . . . .	57
2.36 Overview of published results on thin, intrinsically stretchable conductors patterned over large area . . . . .	61
3.1 Sensing principle and design of the soft flexion sensing strip with soft interconnects for humanoid fingers. . . . .	65
3.2 Equivalent electrical circuit of the soft integrated flexion sensing strip for humanoid fingers. . . . .	66
3.3 Soft flexion sensing strip after mounting on a textile glove and worn on the iCub robot with its finger fully flexed. . . . .	67
3.4 Response of sensor 1 to flexion of the MCP joint. . . . .	67
3.5 Acquisition of robotic index finger position with the soft sensor strip. . . . .	69
3.6 Soft resistive sensor for transducing the relative motion of the first two phalanx of a human finger . . . . .	72
3.7 Characterization of the sensors as goniometer . . . . .	73
3.8 Thermal response of a resistive sensor strain sensor . . . . .	74
3.9 Coupling soft strain sensors with soft tactile force sensors on a glove . . . . .	75
3.10 Grasp transduction using a glove equipped with soft strain sensors and soft tactile sensors . . . . .	77

---

3.11 Design of a single sensor for characterization and sensor pair for on-finger flexion and extension sensing. . . . .	80
3.12 Fabricated epidermal soft strain sensors . . . . .	81
3.13 Relative change in resistance of a single strain gauge as a function of longitudinal strain, transverse strain, and normal pressure. . . . .	82
3.14 Experimental set-up for joints angle recording and sensor readout. . . . .	83
3.15 Calibration of a pair of epidermal strain sensors . . . . .	84
3.16 Evaluation of the accuracy of the epidermal strain sensors for joint motion encoding . . . . .	87
3.17 Picture of a rosette made of stretchable gold thin film connected with EGaIn wires. 90	90
3.18 Rosette under 0% and 50% uniaxial strain and orientation of the two principal strains relative to the branches of the rosette. . . . .	90
3.19 Detection of principal strains magnitudes and directions with a stretchable strain gauge rosette. . . . .	91
3.20 Set-up for isotropic deformation of the rosette . . . . .	92
3.21 Detection of isotropic strain using with a stretchable strain gauge rosette. . . .	92
4.1 The Otto Bock Michelangelo myoelectric prosthetic hand. . . . .	98
4.2 The WiseSkin sensory feedback system. . . . .	99
4.3 Desing of the WiseSkin sensor nodes. . . . .	100
4.4 Conformal power distribution system for the WiseSkin project. . . . .	100
4.5 Process-flow for the integration of the WiseSkin sensor node into the soft strip system. . . . .	101
4.6 Rigid sensor node integrated in a the soft strip. . . . .	102
4.7 Characterization of the sensor nodes inserted in the finger-sized power distribution system and mounted on the Ottobock prosthesis . . . . .	103
4.8 Relative increase in resistance . . . . .	106
4.9 Characterization of a soft micro-heaters matrix. . . . .	107
4.10 Optical and infrared imaging of the soft heaters matrix. . . . .	107
A.1 Set-up for the measurement of 4-wire resistance. $L_w$ is the length of the section of the wire under measurement. . . . .	120
A.2 Calibration of gallium thermal evaporation and computation of the Ga/Au atomic ratio $\beta$ . . . . .	122
A.3 Image processing method for bulges detection in biphasic thin films. . . . .	123
A.4 Determination of biphasic film thickness. . . . .	124
A.5 Resistance of tests tracks as a function of time and failure time as a function of DC current. . . . .	125
A.6 Resistance of a self-heated biphasic gold-gallium track as function of temperature of the track. . . . .	128



# List of Tables

I.1	Young's moduli and thicknesses for a three layer mechanical model of the human skin. . . . .	1
1.1	Properties of Sylgard 184 silicone elastomere. Young's modulus is given for curing temperatures of 25 °C to 100 °C. . . . .	9
1.2	Typical properties of representative stretchable conductors. . . . .	12
1.3	Properties of liquid metals used in this work, and comparison with water. . . .	13
2.1	Comparison between the three stretchable metallization techniques on stretchable PDMS substrates reported in this chapter. NC: Not Characterized. . . . .	59
3.1	Type and number of tasks for all data acquisition sessions. . . . .	85
3.2	Mean absolute errors and baseline resistances through all trials, with 100 μm and 50 μm wide gauge tracks. . . . .	86



# Introduction

## Mechanics and sensory function of human skin

The human skin is a large organ with a surface area between  $1.5 \text{ m}^2$  and  $2 \text{ m}^2$  and varies between 0.2 mm (eye-lids) and 6 mm (foot sole) in thickness [1]. Figure I.1 illustrates that skin tissues are among the softest in the body and can experience strains greater than 30% without plastic deformation [2–4]. It is composed of three main layers: the dermis, the epidermis and the hypodermis. Table I.1 summarizes typical mechanical parameters for each layer. Young's modulus values should be considered orders of magnitude since biological tissues are fibrous, with non-isotropic, non-linear elastic properties that highly depend on water content [1, 5, 6].

The skin is not only a soft barrier protecting our organs but also contributes to our environmental and self-perception through sensing. It contains a very large number of distributed cutaneous receptors, which are visualized in Figure I.2. They convert tactile, thermal and noxious mechanical stimuli into digital electrical signals (action potentials) which are conveyed to the central nervous system via the dorsal root ganglia (DRG) neurons [7, 8]. In particular, the mechanoreceptors involved in tactile sensation are situated in the dermis and epidermis. Approximately 17 000 mechano-receptive units are distributed on the surface of the skin [7], with densities greater than  $100 \text{ cm}^{-2}$  at the finger tips [9]. Each receptor is specialized and responds preferentially to a certain type of stimulus (pressure, stretch, vibrations or edge detection).

Layer	E (MPa)	t (mm)
Stratum corneum	6.0	0.015
Living epidermis and subepidermal nonechogenic band	0.05	0.05
Deep dermis	0.6	1.235

Table I.1 – Young's moduli E and thicknesses t for a three-layer mechanical model of the human skin. From [1].

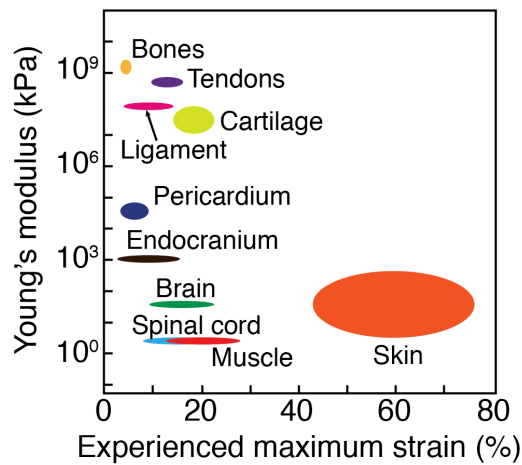


Figure I.1 – Young's modulus of human tissues as a function of experienced maximal strain. Adapted from [4].

Other receptors in the muscles and tendons specialize in proprioception, which is the sense of static position and motion of the limbs and body [10]. Muscle spindles are parallel to the muscle fibers and respond to muscle stretch. Golgi tendon organs are situated at the junction between the muscle and the tendon and respond to muscle stretch and contraction. Signals from the cutaneous receptors, proprioceptors and motor neurons are processed by the central nervous system to build a self representation of the body. This representation is used to adjust movement and force in the limbs in order to perform complex tasks [11].

From an engineer's perspective, the skin mechanoreceptors suffer from low accuracy, non-linear, time-varying and hysteretic response [12]. However, the large number and variety of mechanoreceptors distributed across the body surface enables extraction of rich tactile and proprioceptive information during environment exploration and manipulation.

The possibility to distribute receptors within a soft organ that can move with the body has been an inspiration for artificial systems. The next section shows that many applications can benefit from structures mimicking the sensing and mechanical properties of the skin.

## Artificial skin: vision and applications

The concept of a nature-inspired sensitive skin integrating tactile, temperature and chemical/biological sensors emerged in the popular science-fiction of the 1970s before developing as a research area in the early 2000s [15, 16]. Large area active flexible electronics transitioned from academia to industry at that time [17]. Researchers had already identified electronics materials that can stretch, and not only bend, as a critical technology to realize the vision of an



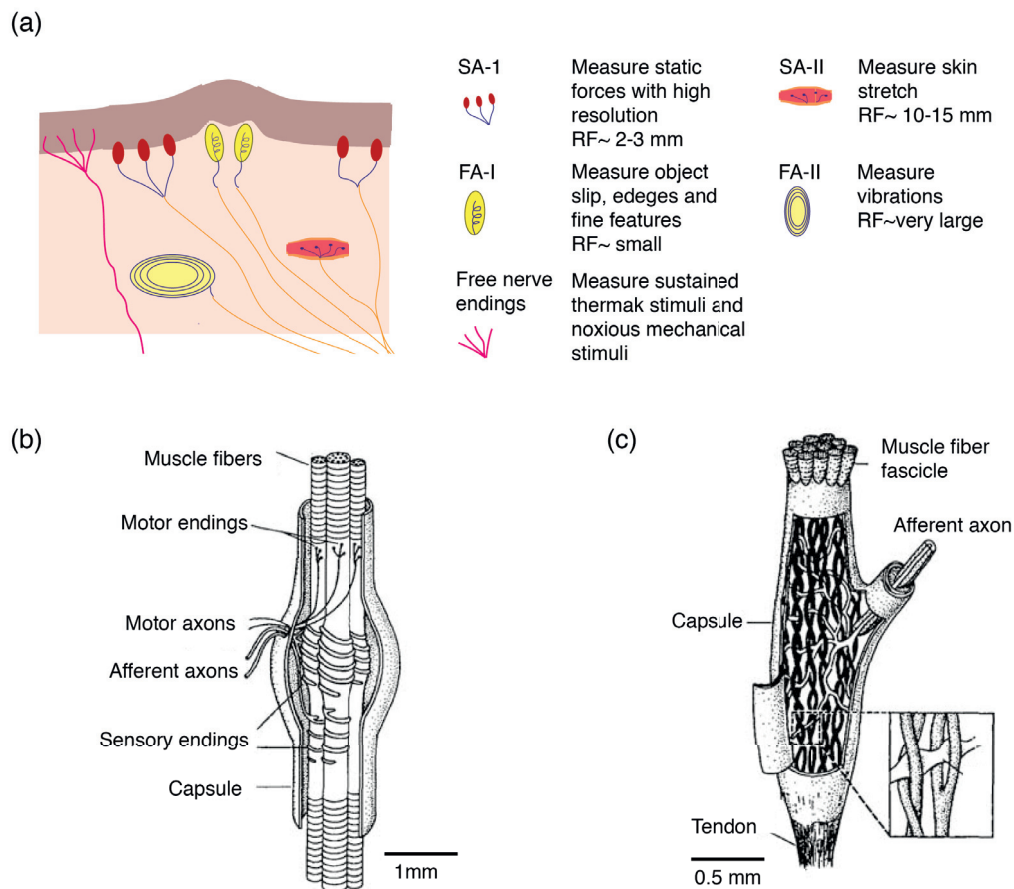


Figure I.2 – Mechanoreceptors in the human skin. **a)** Types, function, temporal response and density of mechanoreceptors in the human skin. RF, receptive field; SA-I and SA-II, slow adapting receptors; FA-I and FA-II, fast adapting receptors. Adapted from [13]. **b)** Mammalian muscle spindle respond to muscle stretch and **c)** Golgi tendon organ respond to muscle stretch and contraction. Adapted from [14].

artificial skin covering robotic or human bodies. The ability to stretch is required to conform to multiple radii of curvature and cover articulated joints without motion impediment or device failure[16]. Since then, extensive research effort has been conducted to design substrates, conductors, semi-conductors, opto-electronic materials, and system integration strategies for stretchable electronics[15].

Comprehensive reviews and textbooks on applications of artificial skin have been recently published [18–24]. Some examples are illustrated in Figure I.3 and include:

- replacement of a missing sensory function such as tactile sensing or proprioception in prosthesis.

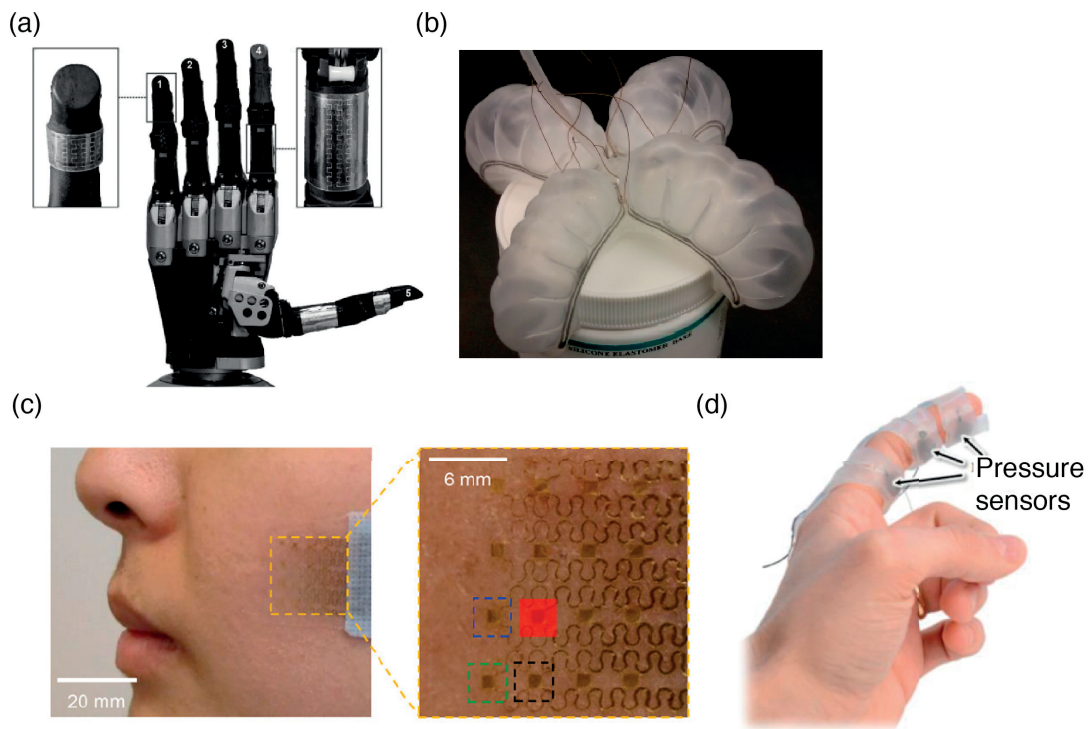


Figure I.3 – Examples of application for skin-like transducers. a) Flexible graphene capacitive sensors based on interdigitated electrodes integrated at the intermediate and proximal phalanges of an i-Limb prosthetic hand. From [25]. b) Soft pneumatic robot gripping a cylindrical container. Liquid-metal strain gauges are visible around the outside edges of the pneumatic channels (dark against the white background). From [26]. c) Ultrathin, conformal device for evaluating thermal transport characteristics and validation on human skin. Magnified view showing the location of a heater (red), a sensing element (blue, black and green). From [27]. d) A soft sensor finger glove with pressure and strain sensors worn by a user. From [28].

- sensing for control in robotics.
- recording body-related parameters such as grasping force, motion, skin hydration, or sweat analysis for physiological studies.

Scientific and technological challenges remain before man-made electronic skins can be on a par with their natural counterpart and are discussed in the next section.

## Challenges for skin-like transducers and systems

Future multi-sensory and large area electronic skins would rely on a combination of soft and rigid integrated components distributed within a stretchable matrix to achieve powering, sensing and signal conditioning [20, 29]. For instance, an electronic skin could combine soft transducers (e.g. rubber-based strain or pressure sensors), rigid sensors (e.g. thermocouple

or hearth rate counter), rigid integrated circuits for signal processing and management (e.g. analog to digital converters or multiplexers) and powering elements (e.g. batteries or solar cells).

One the most crucial element in such hybrid system is the interconnect network that must distribute electrical power and signals between all the elements over a large area and under potentially extreme and repeated mechanical deformation [13]. The conductive tracks must combine:

- a high conductivity to enable design of low power wearable devices.
- a limited sensitivity to strain to guarantee circuit functionality even under large deformations.
- compatibility with high density arbitrary patterning to handle a large number of inputs and outputs.

The metallization technology selected to define the interconnects should also facilitate the integration of stretchable electronic sensors such as capacitive sensors or strain gauges. Ideally, it should be possible to define the sensors' electrodes and the interconnects using the same technology so that both are fabricated in a single metallization run.

Finally, it is also critical that the interconnects technology is compatible with high throughput deposition and patterning methods for translation to large area and large scale production.

### **Contribution of this thesis**

In this work, I designed stretchable metallization methods enabling ultra-compliant systems integrating soft and rigid transducers. The technologies were applied to produce soft sensors that are mechanically comparable to the human skin and provide motion and tactile perception capabilities.

The experimental studies on stretchable metallization technologies resulted in:

- an original combination of intrinsically stretchable conductors providing local contrast in terms of conductivity and strain sensitivity.
- a novel thin film metallization process combining low resistance up to large strains and high density patterning over large areas.

Then, I applied the obtained technologies to:

- 
- fabricate skin-like strain sensors that can be mounted on the hand to encode fingers' motion.
  - power rigid tactile sensor nodes integrated in a skin-like elastomer scaffold.
  - assemble a soft multilayer matrix of micro-heating elements.
  - characterize the performance of all the obtained transducers in realistic use cases.

## **Outline of the thesis**

In the first chapter, I present the state of the art for stretchable interconnects' technologies, and their applications to hand-worn motion transducers. The second chapter covers experimental investigations of deposition, patterning and electromechanical characterization of micro-cracked chromium/gold thin films, micro-plotted gallium indium eutectic (EGaIn) wires, and biphasic (liquid-solid) gallium-based thin films. The third chapter contains characterization of hand-worn strain sensors fabricated with these metallization technologies. Finally, in the fourth chapter I report on a wireless MEMS tactile sensing system and micro-heaters enabled by biphasic gallium-based thin films.

# 1 Specifications, technologies, and selected applications for skin-like transducers

In this chapter, technical requirements to design and assemble skin-like sensors are first presented. Then, I give an overview of the state of the art for stretchable electronics conductors and justify why stretchable thin films and liquid metals can meet the prerequisites to the fabrication of electronic skins. Finally, I present how hand-worn sensors are advantageous for some neuro-rehabilitation applications and the possible benefits from artificial skins in this context.

## 1.1 Specifications for skin-like electronic transducers

### 1.1.1 Motivation

Certain general specifications guide the choices of materials and methods to construct electronic sensors or actuators mimicking skin properties such as extreme conformability and stretchability [30, 31]. I report below mechanical, electrical, and processing requirements that are common to all types of skin-inspired transducers.

### 1.1.2 Mechanical specification

A skin-like device should have a low elastic modulus (of the order of 1 MPa or less) to avoid impediment to motion and conform to the body in three dimensions. It must be thin to minimize its stiffness, defined by the product of the elastic modulus by the thickness. Reducing the stiffness also results in less stress in the layers deposited on top of the substrate when devices are bent [32]. The substrate's elastic regime should at least match that of the skin (0-60% strain) to reversibly accommodate repeated stretching. Finally, it must be biocompatible when worn on the skin for extended periods of time. As the substrate is usually dominant in the mechanical response of a stretchable electronic device, these specification should guide the choice of the substrate.

---

### **1.1.3 Electrical specifications**

Stretchable conductors should match the mechanical specifications of the substrate (maximum elongation), without increasing its stiffness or decreasing its elastic regime. They must have stable electrical and electro-mechanical properties (conductivity, strain sensitivity) to enable rational circuit design. They should also be easily shaped to arbitrary, high density multilayer patterns over large areas to produce transducers and connect standard components in complex hybrid (rigid-soft) circuits. Finally and as for the substrate material, they must not be toxic or hazardous.

### **1.1.4 Process specification**

Since skin-like electronics promise to be ubiquitous and cover large areas, their fabrication process should combine batch or high speed processing, high yields, and compatibility with mass-production requirements (automation, transfer to large production volumes).

### **1.1.5 Conclusion**

I highlighted some key specifications for skin-like transducers:

- the substrate material should combine a low stiffness and a large elastic regime.
- the conductive material should match the elastic regime of the substrate without adding stiffness to the assembly.
- both the substrate and the conductive material should be non-toxic and compatible with high throughput deposition and patterning methods.

In the next section, current technological solutions from the literature are briefly reviewed.

## **1.2 Basic components for skin-like electronic transducers**

### **1.2.1 Motivation**

In this section, the main technological orientations of my work are justified. Namely, I present the rationales that guide the choice of the substrate and stretchable conductive materials to meet the specifications for skin-like transducers established in the section above.

### **1.2.2 Substrate material**

Various rubber materials such as polyurethanes or silicones have been used as substrates for stretchable electronics thanks to their large elastic regimes (> 100% strain), low elastic moduli

## 1.2. Basic components for skin-like electronic transducers

Property	Value
Viscosity (uncured, mixed) (cP)	3500
Color	Transparent
Working time at RT (h)	>2
Young's modulus (MPa)	1.3-2 [42]
Tear strength (Nmm <sup>-1</sup> )	2.6
Elongation at break (%)	140
Linear CTE (ppm K <sup>-1</sup> )	310
Resistivity (Ω cm)	1.2 × 10 <sup>14</sup>
Water diffusion coefficient (m <sup>2</sup> s <sup>-1</sup> )	10 × 10 <sup>-9</sup> [40]

Table 1.1 – Properties of Sylgard 184 silicone elastomere. Young's modulus is given for curing temperatures of 25 °C to 100 °C. From [43] unless stated otherwise.

(of the order of 1 MPa), and resistance to fatigue[33]. Hydrogels might also be used as coating for even softer interfaces with skin (elastic moduli <100 kPa) but must be kept swollen by a solvent [34].

In this work, I chose silicone, and in particular polydimethylsiloxane (PDMS), as a substrate material. Indeed, it offers a combination of mechanical properties and processability which makes it suitable as a support and encapsulation material in micro-fabricated soft circuits.

PDMS is a polymer with formula  $\text{CH}_3\text{-}[(\text{CH}_3)_2\text{Si-O-}]_n\text{Si}(\text{CH}_3)_3$ , where  $n$  is the number of repetition of the  $(\text{CH}_3)_2\text{Si-O-}$  monomer [35]. When exposed to an oxygen plasma,  $\text{-OH}$  silanol groups develop at the elastomere surface to the expense of  $\text{-CH}_3$  methyl group [36]. When two plasma activated PDMS layer are brought into contact, irreversible  $\text{Si-O-Si}$  bonds are formed after the loss of a water molecule. This is especially convenient to create multilayer structures or permanently encapsulate conductive traces deposited on PDMS [37, 38].

PDMS is commercially available from various suppliers. Sylgard 184 (Dow Corning) is a popular grade since it is supplied in small quantities suitable for academic research and I report some of its properties in Table 1.1. It is obtained by mixing a prepolymer base and a platinum-based curing agent, and contains silica nanoparticles fillers [39]. When using PDMS as a substrate, one must take into account its very large coefficient of thermal expansion (CTE), hydrophobicity, moisture absorption [40] and large swelling ratio for some common solvents such as acetone [41].

---

### 1.2.3 Stretchable electronic conductors

Inorganic electronic conductor materials such as metals or conductive oxides usually fracture or experience plastic deformation at low strains (<5%) and are not suitable to form stretchable conductors in the bulk or plane film form [30]. Conductive polymers such as PEDOT:PSS are also brittle[44]. Hence, strategies must be developed to engineer electronic conductive materials that can reversibly sustain large strains [13, 45–48]. It usually involves reversible motion of the conductive material at the molecular, nano, micro or mesoscopic scale.

Figure 1.1 summarizes different approaches reported in the literature:

- molecular scale motion occurs in liquid metals such as gallium-indium eutectic (EGaIn) where weak molecular bonds allow for material rearrangement without catastrophic fracture [49, 50].
- blends of conductive polymers allow the crystalline conductive domains to accommodate large strains without fracturing [51]. To this respect, blends of poly(3,4-ethylenedioxythiophene) polystyrene sulfonate (PEDOT:PSS) and ionic liquids offer the best electro-mechanical performance [44, 52].
- percolating composites of conductive nano-particles and elastomers maintain conductivity thanks to relative motion of the conductive fillers at the nanoscopic scale and tunneling [53, 54]. High aspect ratio conductive fillers typically raise higher electro-mechanical properties (conductivity, stretchability) [55, 56], enabling complex circuits integration [57].
- micro-cracked thin metal films on rubber substrates accommodate large (>30%) strains thanks to out-of-plane deflection and twisting of the metal ligaments [58].
- net-shaped metal thin films, which are the negative of micro-cracked structures, also accommodate strain by out of plane bending and twisting [59].
- metals, organic or inorganic semi-conductors are deposited or laminated on prestretched substrates and form wrinkles when the substrate is released. The amplitude of the wrinkles depends on the mechanical and geometrical properties of the stack materials [60–62]. The deposited materials sustain strains corresponding to the direction and magnitude of the pre-stretch.
- plastic-metal-plastic meander-shaped structures or conductive sheets cut with specific patterns can buckle out of plane to accommodate large deformations[63–65].

Non-electronic conductors such as ionic liquids offer interesting features for selected applications such as a very high transparency [66]. However they are more resistive (e.g.  $1 \times 10^3 \Omega/\text{sq}$  for 100  $\mu\text{m}$  thickness [67]), and require special interfacing as well as careful management of the electrical potentials to avoid electro-chemical reactions[68].



## 1.2. Basic components for skin-like electronic transducers

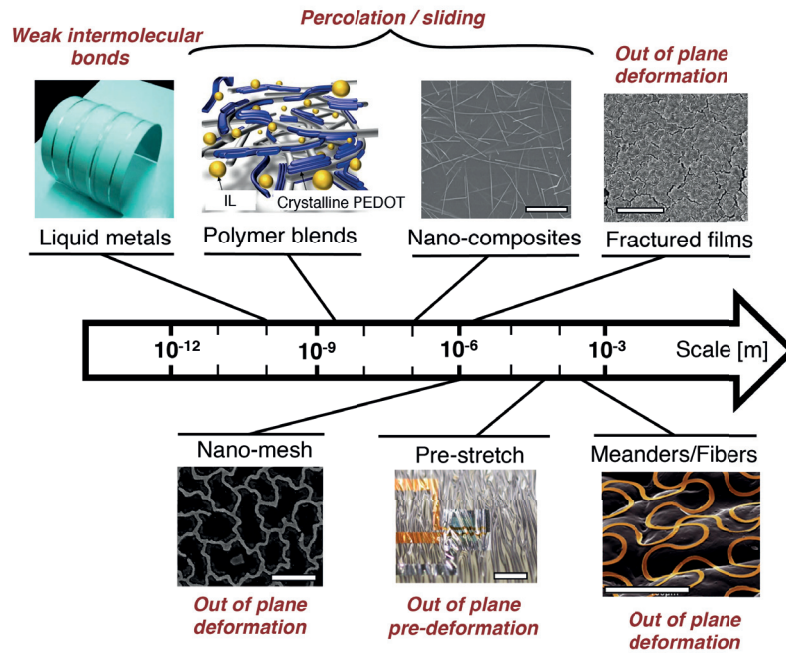


Figure 1.1 – Scale of motion for reversible strain accommodation in various stretchable electronic conductors. Illustrations include from left to right and top to bottom gallium-indium eutectic printed on a sheet of paper [69], ionic liquid and poly(3,4-ethylene-dioxythiophene):poly(styrenesulfonate) (PEDOT:PSS) blend [52], Ag nanowires-PDMS composite [55] (scale bar: 5  $\mu\text{m}$ ), Cr/Au micro-cracked thin films [70] (scale bar: 1  $\mu\text{m}$ ), Au nano-mesh pattern by grain boundary lithography [59] (scale bar: 2  $\mu\text{m}$ ), ultrathin thin film transistor stack on relaxed pre-stretched elastomer substrate [62] (scale bar: 200  $\mu\text{m}$ ), polyimide-Cr/Au-polyimide meander patterns on skin replica [71] (scale bar: 200  $\mu\text{m}$ ).

### Liquid metals and stretchable thin metal films

In this work, I investigated two metallization approaches offering superior electromechanical characteristics compared to other solutions as summarized in Table 1.2: liquid metals and micro-cracked thin metal films. I detail their advantages further below.

Micro-cracked thin films are nearly discontinuous percolating networks of metal ligaments that accommodate large strains by bending and twisting out of plane at the micron scale [58, 70]. They enable micro-patterning - including photolithographic masking [38] - and compact multilayer structures [79]. They can maintain their electro-mechanical properties up to a million stretch cycles [80]. In addition, their intrinsic stretchability guarantees straightforward design and processing for arbitrary circuit layouts. This technology has been used to produce stretchable circuits [81], capacitive sensors [82–84] or electrodes for biological recording and stimulation [80, 85], but were not investigated as sensing material for resistive strain gauges prior to this work to my knowledge. For this type of sensors, the high resistivity of the metal

	Thin metal films	Silver-based composites	Conductive polymers	Liquid alloys
Conductive material	Au or Cu	AgNW or flakes	PEDOT:PSS	EGaIn
Initial conductivity (S cm <sup>-1</sup> )	>4 × 10 <sup>5</sup>	8100 NW 738 flakes	3100	3.4 × 10 <sup>4</sup>
Maximum strain	20% $\mu$ -cracked 300% meanders	50% NW 215% flakes	600%	700%
Resistance R or resistivity $\rho$ increase @ max strain	4X R $\mu$ -cracked 0X R meanders	0X R NW 4X $\rho$ flakes	30X $\rho$	55X R
Cycles without electrical failure	1 × 10 <sup>6</sup> @20% $\mu$ -cracked 110 @20% meanders	1000 @20% NW 100 @20% flakes	1000 @100%	4000 @50%
Limitations	Sheet resistance $\mu$ -cracked Cycling meanders	Resistivity	Resistivity	Patterning
References	[64, 70, 72, 73]	[55, 74, 75]	[52]	[76, 77]

Table 1.2 – Typical properties of representative stretchable conductors, excluding pre-stretch strategies. Partially adapted from [78].

films is an advantage since it results in high strain sensitivity and straightforward readout.

Liquid metals have a melting point below or near room temperature and appear as natural candidates to form stretchable conductive tracks. Mercury was indeed proposed in the 1950s for body worn stretchable strain gauges [86]. Non-toxic liquid metals that are more suitable for electronic skins applications, such as gallium-indium eutectic, attracted interest in the late 2000s as silicone microchannels filled with the alloy were demonstrated [49, 87]. They offer a very low electrical resistivity (about 10 times that of aluminum, see Table 1.3) and can sustain strains greater than 700% [77]. A few nanometers thick oxide skin forms spontaneously at the surface of gallium-based liquid metals in contact with air. The oxide skin makes it challenging to print the metals using conventional approaches like inkjet or screen-printing and strategies have been developed to circumvent these limitations [88, 89]. These include injection in microfluidic channels, imprinting, selective wetting, and direct writing in 2D or 3D [50, 78, 90–92]. However, none of these methods combines batch processing and micron-scale patterning over large surface areas (>50 cm<sup>2</sup>) [78].

## 1.2. Basic components for skin-like electronic transducers

	Gallium	EGaIn	Water
Melting point (°C)	29.8	15.5	0
Boiling point (°C)	2402	2000	100
Vapor pressure at RT (Pa)	1e – 36 [93]	NR	2300
Density (gcm <sup>-3</sup> )	6.91	6.36	1
Viscosity (1 × 10 <sup>-3</sup> kgm <sup>-1</sup> s)	1.969	1.99	1
Surface tension (mNm <sup>-1</sup> )	750	632	72.8
Thermal conductivity (Wm <sup>-1</sup> K)	30.5	26.4	0.6
Resistivity (μΩ cm)	27.2	29.4	20 × 10 <sup>8</sup>

Table 1.3 – Properties of liquid metals used in this work, and comparison with water. Adapted from [91] unless stated otherwise. NR: Not Reported.

Finally, since both approaches rely on intrinsically stretchable conductors, they guarantee a maintained electrical conduction even if stretched in arbitrary modes or direction. Unlike pre-stretched circuits, they can sustain solicitations that were not anticipated when fabricating the circuit. In particular, they are insensitive to local stress concentration that may occur if a section of the circuit is unintentionally clamped.

### 1.2.4 Conclusion

I briefly reviewed the stretchable conductors strategies reported in the literature and highlighted that:

- stretchability is enabled by the reversible motion of the conductive material at the molecular, nano, micro or mesoscopic scale.
- micro-cracked thin metal films are promising to build imperceptible strain sensors, a particular class of skin like transducers.
- liquid metal offer an unmatched combination of high conductivity and very large (>700%) rupture strain.

In the next section, I show that stretchable conductors meet criteria for long-term, imperceptible hand-worn movement and tactile monitoring for innovative therapeutic applications.

---

## 1.3 Skin-like motion and tactile transducers for the hand

### 1.3.1 Motivation

Neurological disorders such as stroke, multiple sclerosis or Parkinson's disease impact mobility and natural control of the upper limbs [94, 95]. Traumatic events such as amputation also force patients to adapt their control strategies to a prosthesis that doesn't feel natural. Indeed, amputees often cite the lack of tactile sensory feedback as a reason for poor embodiment and eventually abandonment of motorized prosthetic hands [96]. Innovative therapies designed to help patients improving and ultimately regaining motor control of impaired or artificial limbs often implement a combination of robotic, stimulation, and sensing technologies.

In this section, I show that existing solutions are too cumbersome for routine motion or tactile monitoring of the hand in the clinic or at home. Electronic skin equipped with strain and tactile sensors would be a favorable alternative but bulkiness and reliability issues currently limit their translation to therapeutic applications, calling for more imperceptible and robust solutions to achieve an improvement in patients' quality of life.

### 1.3.2 The human hand

The human hand is highly articulated (14 joints, see Figure 1.2), and its ability to perform fast and highly dexterous movements has been an inspiration to build robotic grippers [11, 97]. Tactile and proprioceptive sensory feedback are key to successfully perform precision manipulation tasks such as writing [98].

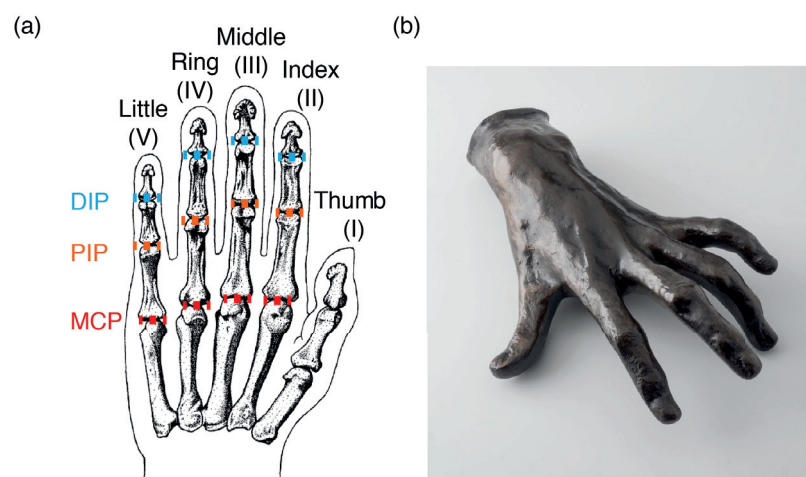


Figure 1.2 – Anatomy of the human hand. a) Identification of the fingers joints: metacarpophalangeal (MCP), proximal interphalangeal (PIP) and distal interphalangeal (DIP). Adapted from [99]. b) Hand of a pianist by Auguste Rodin. Copyright Rodin Museum, Paris.

### 1.3.3 Hand motion encoding

#### Applications for neuro-rehabilitation and current solutions

Vision or robotic based systems are now common in research or clinical therapy to provide high accuracy in movement monitoring and restoration. Their use may promote more effective and faster rehabilitation [100]. However, they require complex, large and/or expensive equipment and software for data treatment that are difficult to adapt to a system for daily usage in the clinic and at home.

Inertial sensors are easier to integrate into a portable system but are prone to integration drift, which limits their accuracy over long periods of time [101]. Hand posture and motion can also be monitored with data gloves during rehabilitation therapies or assistive devices usage [102, 103]. Commercially available systems such as the Data Glove (5DT Inc. Irvine, CA) or the Cyberglove (Cyberglove Systems LLC. San Jose, CA) are still cumbersome and often restrict the natural motion of the fingers (see Figure 1.3).

In the neurorehabilitation context, gloves may also impede access to the skin for recording and stimulation of muscle activity. Moreover, they cover the hand palm, altering tactile sensation and grip ability. Tracking gloves become difficult if not impossible to put on if the patient's hand is locked in a closed fist position after a stroke. Finally, variability in hand segments length across individuals necessitates the possibility of adjustment and personalized fitting for hand-worn devices [104].



Figure 1.3 – Example of a commercially available wearable motion sensing for the hand: the Data Glove Ultra from 5DT. Picture copyright 5DT.

#### Benefits and challenges for skin-like strain sensors

Lightweight, body conformable strain sensors are regarded as a promising alternative to the existing solutions reported above [105]. Resistive strain gauges made of soft material

---

are unobtrusive for body movement, straightforward to produce since they are essentially composed of a single metallization layer, are insensitive to electromagnetic perturbations, and do not require complex read-out circuitry.

Important metrics for evaluating the performance of a strain sensor are: maximum strain allowed, gauge factor (GF, defined as  $GF = \frac{\Delta R}{R_0 \epsilon}$ , where R is the sensor's resistance and  $\epsilon$  the applied strain), linearity, hysteresis, response time, overshoot behavior and durability [106]. Conductive rubber composites have been widely studied as a sensing material for stretchable movement tracking devices [107]. However, they suffer from strain rate dependent response, hysteresis and overshoot due to their viscoelastic behavior and the interactions between conductive filler and polymer material [106, 108]. By contrast, liquid metal sensors offer higher linearity, lower hysteresis and fast response with no overshoot or relaxation phenomena [109, 110].

Localized strain detection is often achieved using rigid, strain insensitive wires to probe the soft and stretchable sensors [111] (see Figure I.3d page 4). It results in bulky and fragile systems since the interface between the soft sensors and the hard wires favours mechanical failure [28]. Strategies can be developed to integrate soft strain sensors and soft interconnects in a single device. Examples include varying the geometry of conductive composite patterns between low strain sensitive meanders and highly strain sensitive straight tracks [112], or coupling highly resistive ionic liquid and highly conductive liquid metal [68, 113]. Finally, maintaining a thin and light form factor is crucial for coupling with actuators for closed-loop control of rehabilitation or assistance devices such as hand exoskeletons [26, 114].

Improving the usability of stretchable sensors for routine hand motion tracking should focus on increasing the systems' robustness while maintaining a very thin form factor for minimizing the impediment to motion or therapeutic manipulations. It also necessitates a systematic evaluation of the accuracy, time response and sensitivity to parasitic stimuli or noise. Finally, the sensors should be compatible with integration in a compact, low power and portable data acquisition system for long-term monitoring.

### **1.3.4 Tactile sensing for the hand**

#### **Applications for neuro-rehabilitation and current solutions**

The development of tactile sensing systems for artificial and robotic limbs is an active research field [19]. An evident application of such sensors in a neuro-rehabilitation context is the elicitation of tactile sensation for upper-limb amputees. However, commercially available sensor systems are still relatively bulky and difficult to mount on highly articulated prosthesis featuring a limited surface area (see Figure 1.4a). For instance, only two discrete sensor with a

### 1.3. Skin-like motion and tactile transducers for the hand

---

limited sensing range of 0 N to 4.5 N were taped on a prosthesis to elicit tactile sensation in [115].

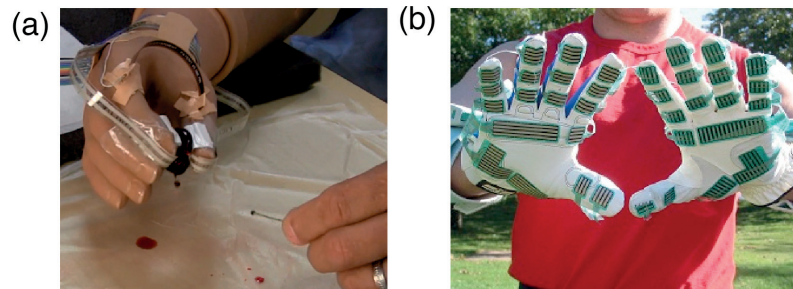


Figure 1.4 – Example of commercially available tactile sensing systems for the hand: t. a) Prosthetic hand equipped with Flexiforce sensors from Tekscan to elicit tactile sensation for an amputee patient. From [115]. b) The Grip system from Tekscan. Picture copyright Tekscan Inc.

Distributed tactile sensors could interface with stimulations systems designed to trigger fine tactile sensations for amputees and provide better embodiment [116]. A combination of sensors and stimulators could also improve amputees quality of life by alleviating the residual phantom pain [117]. Such solutions are not limited to upper limb amputees but could also equip the sockets of lower limb prosthesis for enhanced rehabilitation and control [118]. In general, covering robotic limbs with a sensitive skin could enhance the interactions between patients, robots, and doctors [19].

#### Benefits and challenges for skin-like tactile sensors

Distributed tactile sensors enable richer interaction and exploration of the environment for prosthesis users or robots [119, 120]. Integrating tactile sensors in a glove-like system that can stretch enables to cover most of the hand, including the dorsal sides of the finger, without impeding the movements [84, 121]. However, pressure or force skin-like sensors were never applied in advanced clinical studies involving patients such as amputees to my knowledge. This is likely due to the sensors' cross-sensitivity to strain generated by the limb's motion or electromagnetic noise resulting from interactions with the environment [53, 122].

Advancing the integration, durability, cross-sensitivity and performance of soft tactile sensors is still required to go further than a technological demonstration and test the systems on the long term in realistic use cases [28, 123]. It is a mandatory step before artificial skins can bring a substantial improvement in patients' quality of life.

---

### 1.3.5 Conclusion

In this section, I demonstrated that:

- the human hand is a complex, multi-articulated limb whose motor performance can be affected by neurological diseases or traumatic injuries.
- innovative wearable therapeutic treatment could benefit from skin-like sensors to continuously monitor movements and tactile interactions.
- the ability to deliver high performance, localized sensing in a thin and light form factor is crucial for successful sensor deployment.

## 1.4 Summary and outlook

I examined the mechanical, electrical and processing requirements for stretchable transducers and showed that PDMS gathers the right mechanical and processing properties to serve as a substrate for skin-like electronics. Existing strategies to create stretchable electronic conductors, all based on motion of conductive materials for reversible strain accommodation, were reviewed. I indicated that thin metal films and liquid metal possess particularly interesting properties to fabricate high performance stretchable conductive patterns. Finally, I reviewed existing solutions for hand-worn motion and tactile encoding and suggested that skin-like sensors could lead to significant improvements in wearable set-ups for neuro-rehabilitation applications.

In the rest of the thesis, I present novel technological solutions based on the selected approaches - thin film processing and liquid metals - to assemble skin-like transducers, and in particular strain and tactile sensors for the hand. I also provide extensive characterization of the assembled transducers in realistic use cases.



## 2 Stretchable conductors from thin metal films and liquid metals

As detailed in chapter 1, thin metal films and liquid metal are good candidates to build stretchable electronic transducers, provided that the materials can be processed and patterned to form circuits and interconnects. In this chapter, I report on the experimental investigation of three stretchable metallization technologies. The gauge factor, sheet resistance and strain direction sensitivity of micro-cracked gold thin films are reported in section 2.1. Section 2.2 presents linear resistance and electro-mechanical characteristics of micro-plotted liquid metal interconnects, and their integration with micro-cracked gold tracks. Finally, section 2.3 describes growth, micro-patterning and electro-mechanical characterization of biphasic (solid-liquid) stretchable thin films. The three technologies are compared in the closing section 2.4.

This chapter is adapted from the following publications:

- A) H. O. Michaud, J. Teixidor, and S. P. Lacour. Soft metal constructs for large strain sensor membrane. *Smart Materials and Structures*, 24(3):35020, 2015.
- B) A. Hirsch, H. O. Michaud, A. P. Gerratt, S. de Mulatier, and S. P. Lacour. Intrinsically Stretchable Biphasic(Solid-Liquid) Thin Metal Films. *Advanced Materials*, 28(22):4507–4512, 2016.
- C) H. O. Michaud and S. P. Lacour. Liquid electromigration under dc current in biphasic thin metal films. *In preparation*, 2017.

---

## 2.1 Electro-mechanical characterization of stretchable micro-cracked gold films on PDMS

### 2.1.1 Motivation

Microcracks spontaneously develop in thin gold films thermally evaporated on PDMS under specific deposition conditions [70, 127], as displayed in Figure 2.1. The y-shaped cracks allow for the microscopic gold bands to bend and twist locally out of the plane, thereby reversibly accommodating macroscopic deformations of the substrate [58]. Because the thin films are rough and nearly discontinuous, their resistivity is typically 3-4 times higher than continuous gold films and their resistance increases by about 200% at 50% of applied mechanical strain [128].

Micro-cracked gold film thus possesses interesting properties as strain sensing material for large deformation: a high resistance in the relaxed state, a large strain sensitivity and the possibility to be patterned over large areas using methods like stencil masking.

In this section, I further explore the influence of the deposition parameters on the strain response of the films to demonstrate that:

- the gold thickness can be optimized to achieve controlled initial sheet resistance and strain sensitivity.
- high aspect ratio traces are sensitive to one preferential strain direction.

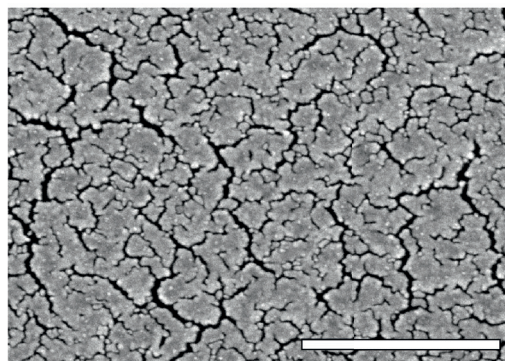


Figure 2.1 – Scanning electron microscope (SEM) picture of the surface of micro-cracked gold thin films deposited on PDMS. Scale bar is 1  $\mu\text{m}$ .

## 2.1. Electro-mechanical characterization of stretchable micro-cracked gold films on PDMS

### 2.1.2 Evaluation of the gauge factor

#### Materials and methods

**Sample preparation:** The process flow for sample preparation is summarized Figure 2.2 and a detailed description of the fabrication process flow is available in Appendix section A.1.1 page 117. It was designed to obtain dog-bone samples following the DIN 53504-S3 standard without applying any stress to release the samples before testing.

To summarize, a first layer of PDMS was spin-coated on a silicon wafer and cured to form a 700  $\mu\text{m}$  membrane. The surface was then spin-coated with a layer of poly(styrene-4-sulfonate) (PSS) release layer. Finally, a second layer of PDMS was spin-coated and cured to form a 120  $\mu\text{m}$  layer. The dog-bone samples were cut in the upper PDMS layer using a plotter cutter (RoboPro CE5000-40-CRP, Graphtec). The next step consisted in aligning stencil masks to define conductive tracks on the dog-bones. Bi-layers of Cr/Au were then thermally evaporated. The thickness of Cr was fixed to 5 nm while the thickness of Au was varied between 13 nm and 60 nm. After thermal evaporation, the shadow masks were peeled-off from the PDMS surface. The wafers were entirely dipped into deionized water for 30 min to dissolve the PSS layer and release the dog-bone samples as shown Figure 2.2i. The gold track featured four contacting pads for four-wire resistance sensing and the distance between the inner contacts was 20 mm.

**Gauge factor measurement:** The samples were tested with a custom symmetric-displacement tensile machine shown in Figure 2.3 and controlled with a Labview (National Instruments). Displacement was induced by a rotary motor (BMS60-UFA, Aerotech) and encoded by two inductive position sensors (Li200P0-Q25LM0, Turck). The control program simultaneously

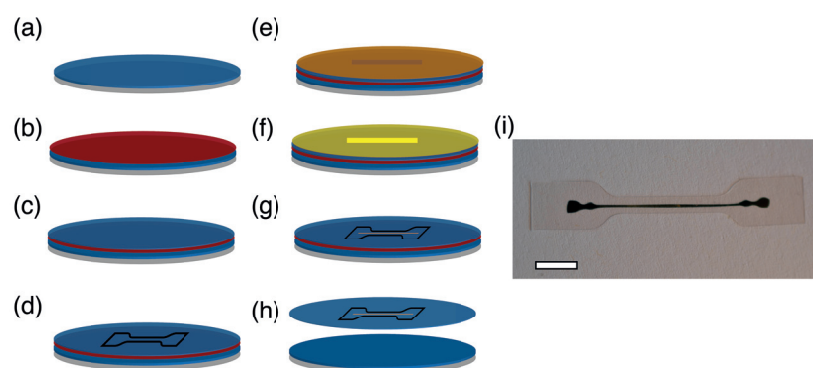


Figure 2.2 – Sample fabrication to evaluate the gauge factor of stretchable micro-cracked film. a) Thick PDMS layer spin-coating. b) PSS release layer spin-coating. c) Thin PDMS layer spin-coating. d) Dog-bone cutting. e) Kapton mask. f) Cr/Au thermal evaporation. g) Kapton mask peel-off. h) Release by PSS layer dissolution. i) Dog-bone shaped tests specimen with evaporated gold track. Scale bar is 5 mm.

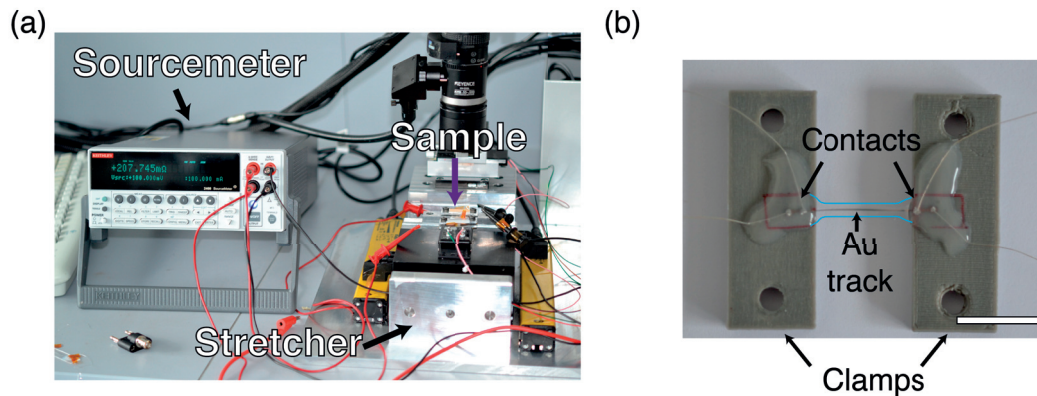


Figure 2.3 – Set-up for gauge factor measurements. a) Picture of the set-up. b) Sample mounted on the stretcher clamps. Blue lines represent the edges of the PDMS substrate. Scale bar is 10 mm.

recorded the applied displacement and the sample resistance at 6 Hz through a data acquisition board and a source-meter (2400, Keithley). The samples were strained at a strain rate of  $1\% \text{ s}^{-1}$  up to 30% strain for 100 cycles. The applied current for four-wire sensing resistance measurement was set to 0.1 mA. The gauge factor was determined from the average slope of the relative resistance versus strain curve at the 101<sup>st</sup> cycle.

## Results and discussion

Figure 2.4 shows scanning electron microscope (SEM, Merlin, Zeiss) images of the surface of the micro-cracked Cr/Au thin films for four Au thickness. Samples with the smallest Au thicknesses displayed a higher micro-cracks density. It corresponded to a sharp increase of the average value and dispersion of the sheet resistance and gauge factor for Au thickness inferior to 15 nm (Figure 2.5a).

The gauge factor was minimum for samples with a initial sheet resistance between  $10 \Omega/\text{sq}$  and  $20 \Omega/\text{sq}$ . It is in agreement with previous studies reporting on very thin metal films subject to microstrain deformation [129, 130]. For thicker films with lower sheet resistance, irreversible fracture appear while for thinner films with higher sheet resistance, nearly discontinuous thin gold ligaments rupture at larger strains .

## 2.1. Electro-mechanical characterization of stretchable micro-cracked gold films on PDMS

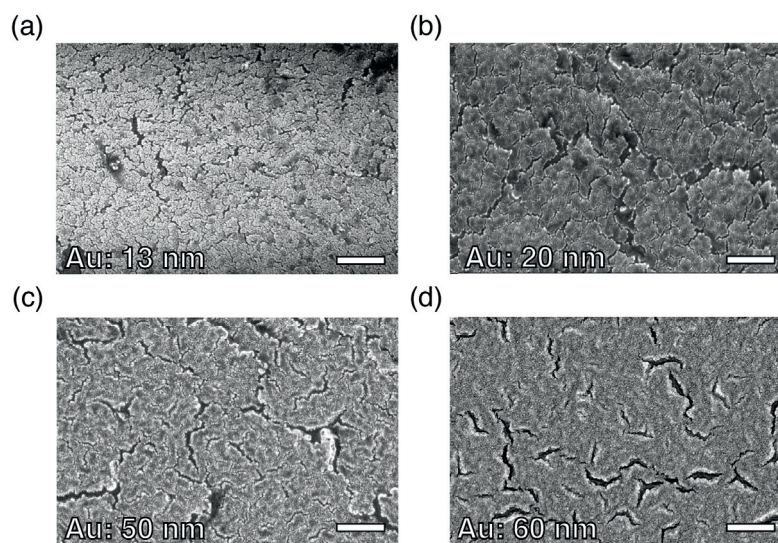


Figure 2.4 – SEM images of micro-cracked Cr/Au surface for a deposited Cr thickness of 5 nm and Au thickness of 13 nm, 20 nm, 50 nm and 60 nm. Samples were imaged as deposited. Scale bars are 1 μm.

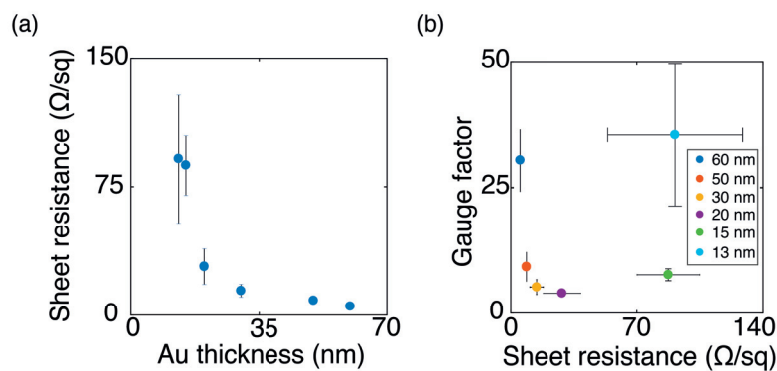


Figure 2.5 – Sheet resistance and gauge factor of micro-cracked gold thin films a) Sheet resistance as a function of deposited gold thickness. Data points represent an average over more than three samples for each Au thickness. Error bars represent standard deviation. b) Gauge factor of micro-cracked gold thin films as a function of sheet resistance. Data points represent an average over more than three samples for each Au thickness. Error bars represent standard deviation.

---

### 2.1.3 Evaluation of sensitivity to strain direction

#### Materials and methods

The samples were prepared according to the process flow detailed in Appendix section A.1.1 page 117. In brief, PDMS was spin-coated and cured on a silicon wafer to form a 120  $\mu\text{m}$  thin layer. A bi-layer of 5/25 nm Cr/Au was then thermally evaporated through a stencil mask laminated on the PDMS substrate. The mask was then peeled-off to form stripes of  $0.5 \times 5 \text{ mm}^2$ .

$15 \times 15 \text{ mm}^2$  membranes of PDMS with two perpendicular Cr/Au tracks were cut manually and clamped in the custom tensile machine. Resistance of the Cr/Au strips was measured using the two point-probe method and EGeIn contacts. The samples were stretched to 10%, 20%, 30%, 40% and 50% strain for one cycle before the resistance measurements were performed up to 50% strain.

#### Results and discussion

As displayed in Figure 2.6, a large increase in resistance was observed when the Au line was aligned with the elongation direction ( $\Delta R/R_0 = 2$  at 50% strain), while a significantly lower increase was observed when the film is stretched perpendicularly ( $\Delta R/R_0 = 0.1$  at 50% strain). Thus a strain gauge made from stretchable Cr/Au has highly directional strain sensitivity, and determination of an unknown strain direction and magnitude would be possible using, for instance, three gauges arranged in a rosette [131].

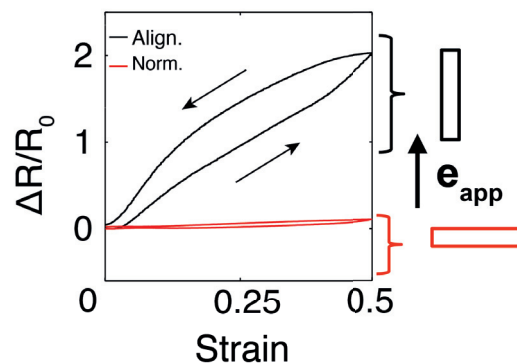


Figure 2.6 – Relative increase in resistance of a 5/25 nm Cr/Au track as a function of strain when the track is aligned with the strain direction or when it is normal to the strain direction.

However, there was a large hysteresis loop in the gauge resistance as the sample was strained and relaxed, with a maximum width corresponding to about 14% strain. This ultimately limited the accuracy of Cr/Au thin films as strain sensors for macroscopic deformations. The hysteresis was also observed in earlier studies on micro-cracked gold films and might come

## 2.1. Electro-mechanical characterization of stretchable micro-cracked gold films on PDMS

---

from rupture of some metal ligaments when the samples are stretched [128, 132]. Long-term cycling could also permanently modify the micro-structure of the films and lead to degraded strain encoding capabilities [72].

### 2.1.4 Conclusion

I defined a range of deposition parameters to form directional strain sensors from micro-cracked gold thin films. The gold thickness was optimized to obtain micro-cracked Cr/Au films with well determined initial resistance and gauge factor. I showed that:

- for a gold thickness ranging from 20 nm to 50 nm, the micro-cracked films gauge factor and sheet resistance had small standard deviations from sample to sample.
- in this range, the gauge factor varied between 4 and 10 and the sheet resistance varied between  $9 \Omega/\text{sq}$  and  $30 \Omega/\text{sq}$ .
- for rectangular gold tracks, with a length/width ratio of 10, the traces sensitivity to strain was 20 times larger along the length direction than along the width direction. This made micro-cracked gold traces suitable for directional strain sensing.

However, the need to use rigid, strain insensitive wires as interconnects in order to probe the tracks could limit this approach for wearable strain sensing. Indeed, the interface between soft sensors and hard wires can lead to stress concentration and failure of the devices [28, 113]. In the next session, I present a set-up to deposit highly conductive stretchable wires and connect to the thin films in order to form all-soft integrated transducers with localized strain sensitivity.

---

## 2.2 Liquid metal micro-plotting

### 2.2.1 Motivation

Liquid metals are especially interesting to form highly conductive stretchable interconnects. Their liquid state allows them to sustain hundreds of percent of strain and makes them immune to mechanical fatigue [92]. They are also compatible with additive manufacturing methods such as printing and plotting [133, 134]. Printing enables a fast and easy redistribution of the conductive traces for custom layouts.

In this section, I report on a 2D plotting setup for gallium indium eutectic (EGaIn). Electro-mechanical characterization of the obtained conductive traces is then presented. Finally, I show that the micro-wires can be connected to micro-cracked gold thin films to form a novel combination of high and low strain sensitivity stretchable conductors.

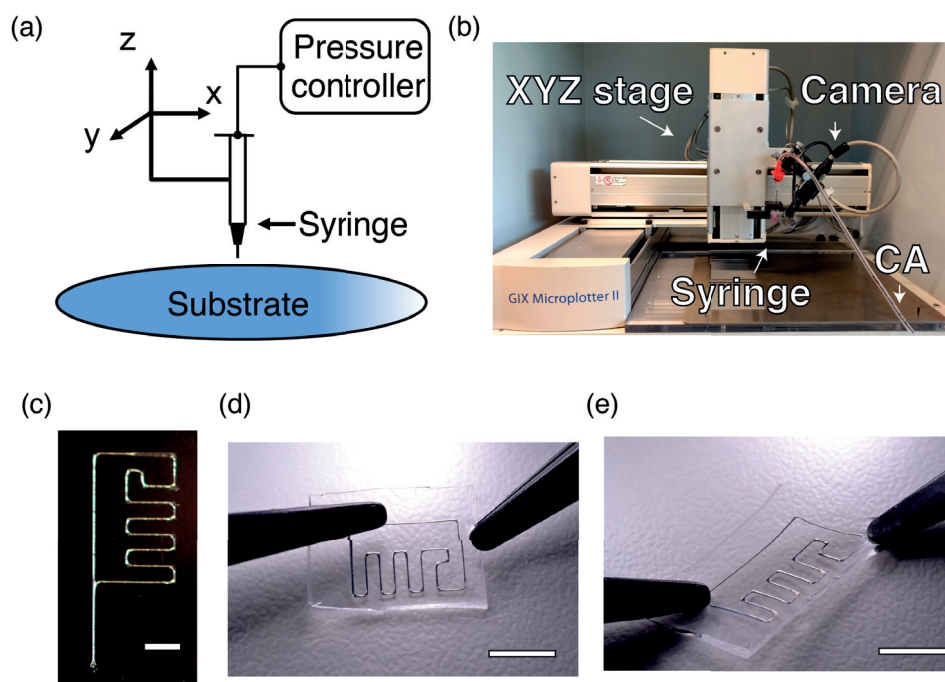


Figure 2.7 – EGAIn microwires plotting set-up. a) Schematic of the EGAIn microwires plotting set-up. b) Picture of the microplotting setup. CA: Compressed air. c) Picture of a printed EGAIn pattern. Scale bar is 2 mm. d-e) Pictures of the same pattern stretched using tweezers. Scale bars are 5 mm.



## 2.2.2 Deposition and characterization of micro-plotted wires

### Materials and methods

**Deposition set-up** I developed a micro-plotting technique similar to that reported by Boley et al. [134]; its schematic is highlighted Figure 2.7 and the fabrication process is detailed in Appendix section A.1.2 page 117. In brief, the metal wires were plotted directly on a PDMS membrane spun and cured on a silicon carrier wafer. Controlling the height, displacement speed and pressure in the dispensing syringe allowed the liquid metal to flow on the substrate and form wires. Solid silver wires were then put into contact with the terminals of the liquid metal wires and secured with silicone sealant. The wires were finally encapsulated by spin-coating and curing PDMS. The total thickness of the samples was below 500  $\mu\text{m}$ . Figure 2.8a displays a cross-sectional view of an encapsulated soft conductor.

**Electromechanical characterization** Four-wire sensing resistance measurements were performed on soft microwires on PDMS substrate without encapsulation. A Keithley 2400 sourcemeter was used in preconfigured four-wire sensing mode, with automatic current selection, in the 20  $\Omega$  range with 100  $\mu\Omega$  resolution. In this range, the accuracy of the measurement was given by  $\Delta R = 0.010\% \times R_{measured} + 3 \text{ m}\Omega$  according to the instrument's manual [135]. Four hook probes mounted on XYZ positioners were used to precisely contact the EGaIn line. Each probe held a 76  $\mu\text{m}$  diameter Au wire (Science Products) which was put in contact with the liquid metal wire. The two outer probes were positioned at the two opposite ends of the wire. The distance  $L_w$  between the two inner probes (see Appendix A.2 page 120), which defined the four-wire sensing resistance, was measured with a digital microscope (Keyence VHX-600, VH-Z50L lens). As the hard probing wires may have damaged the liquid metal wire in the vicinity of the contact point, the spacing between the two inner probes was first set to a maximum of 5 mm and then sequentially reduced to collect the data points.

### Results and discussion

The measured resistances for various wire lengths were compared with the output of an analytical model and shown in Figure 2.8. The EGaIn microwire was modeled as a metallic semi-cylinder with a constant resistivity  $\rho = 29.4 \times 10^{-6} \Omega\cdot\text{cm}$  [136] and a truncated circular cross-section with a radius  $r_w$ . The corresponding resistance  $R_w$  is computed from the measured geometry of the wire using

$$R_w = \rho \frac{L_w}{\beta \pi r_w^2} \quad (2.1)$$

$r_w$  was determined from the length of each wire ( $155 \pm 1 \mu\text{m}$ , mean  $\pm$  S.D. with 18 measure-

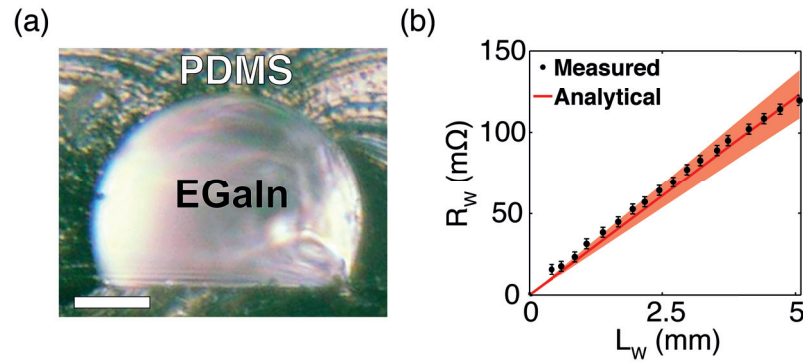


Figure 2.8 – Characterization of micro-plotted EGaIn wires. a) Cross section of a liquid metal wire encapsulated in PDMS. Scale bar is 50  $\mu\text{m}$ . b) Comparison between four-wire sensing resistance measurement and resistance computed from equation (3). Error bars represent measurement accuracy. Shaded area represent 95% confidence interval for the output values of the analytical model.

ments, for the wire in Figure 2.8b) and  $\beta$  ( $0.63 \pm 0.3$ , mean  $\pm$  S.D. with 11 measurements) was experimentally determined after encapsulation by measuring the cross-section of the imprint left by the wires in the PDMS (Figure 2.8a).

The good agreement between the output of the model and the four-wire sensing resistance demonstrated that the deposition process did not increase the resistivity of the liquid metal structures. It also suggested that the encapsulation process did not impact the structure of the microwires. The average cross-section geometry corresponded to a contact angle of about  $102^\circ$  at the interface between EGaIn microwires and PDMS substrate. It was consistent with previously reported values for microwires with similar dimensions [134].

## Electro-mechanical characterization

### Methods

The EGaIn microwires were stretched using the custom motorized uniaxial stretcher described section 2.1.2 page 21. Each end of the samples, including the contact area with silver wires, was clamped on a moving platform. The four-wire sensing electrical resistance and the applied mechanical strain were recorded simultaneously at a frequency of 8 Hz.

### Results and discussion

Figure 2.9 presents the electro-mechanical characterization of an EGaIn microwire. Assuming the EGaIn is incompressible, the volume of the wires remains constant under elastic deforma-

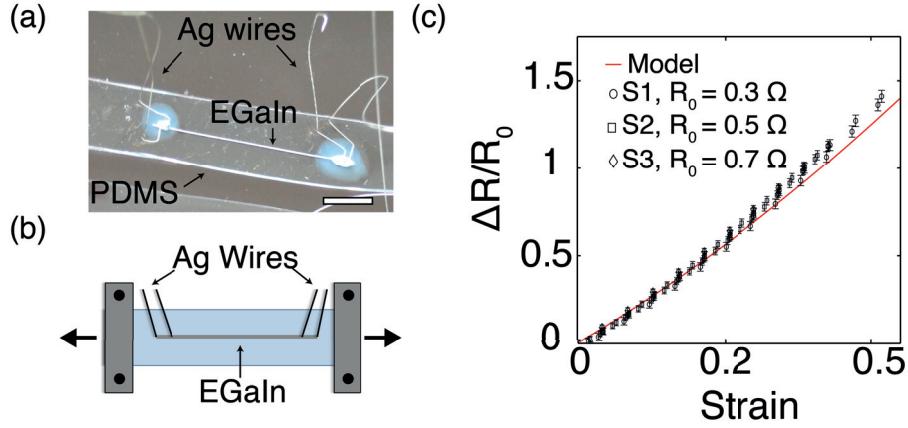


Figure 2.9 – Electro-mechanical characterization of long EGaln wires encapsulated in PDMS under uniaxial strain. a) Picture of a sample. Scale bar is 2 mm. b) Schematic representation of the uniaxial stretching test. c) Resistance of three samples as a function of applied strain and comparison with the constant volume model (Equation 2.2). Resistance was measured using the four-wire sensing method. The initial length of the wires was 25 mm (S1 and S3) and 30 mm (S2). Sample S1 was strained up to 50%, samples S2 and S3 up to 42%. Error bars represent measurement accuracy.

tion and their relative increase in resistance as a function of applied mechanical strain  $e_{app}$  can be expressed as

$$\frac{\Delta R}{R_0} = \left(\frac{L}{L_0}\right)^2 - 1 = e_{app}(2 + e_{app}) \quad (2.2)$$

The good correspondence between the model and experimental measurements indicated that no physical leakage occurred when the wires were stretched. Although soft EGaln microstructures can be used as strain sensitive elements [137], the direct patterning of the EGaln microwires and their minimal increase in resistance under mechanical deformation offer ideal characteristics for elastic interconnects.

### 2.2.3 Connection of micro-plotted EGaln wires to micro-cracked Au tracks

#### Materials and methods

PDMS substrates with patterns of micro-cracked gold were processed in the liquid metal dispensing set-up. EGaln microwires could be drawn continuously from the bare PDMS areas to the gold-coated areas and vice versa. Figure 2.10a presents the microfabrication process developed to integrate compact strain gauges with high and localized sensitivity. First a gold layer was thermally evaporated through a shadow mask on the PDMS substrate. Then, EGaln

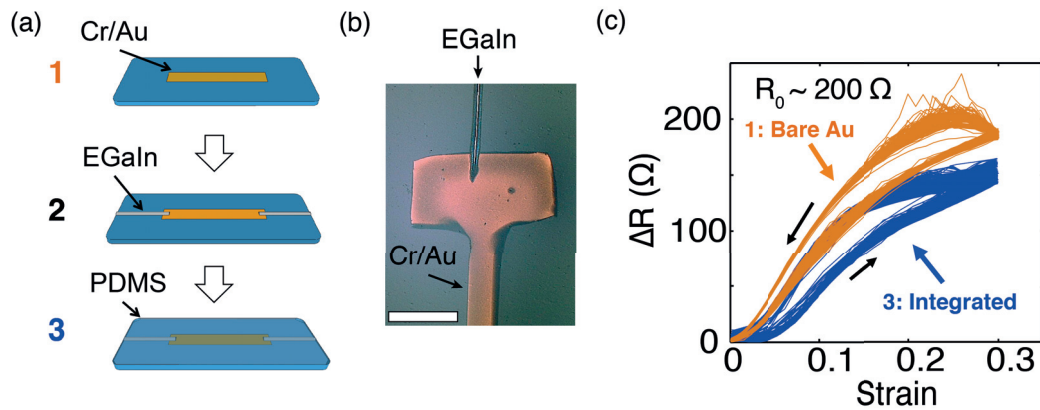


Figure 2.10 – Connection between microplotted EGaIn wires and micro-cracked gold traces. a) Process flow for the fabrication of an integrated strain gauge made of micro-cracked gold and connected with EGaIn microwires. b) Picture of the interconnection area between an EGaIn microwire and a Cr/Au trace. Scale bar is 1 mm c) Comparison of the response of a non-encapsulated gold track probed with solid wiring, connected with silver-filled epoxy adhesive (Epotek H27-D), and an integrated strain gauge with EGaIn interconnects. 125 cycles are represented on this graph for each gauge. Length  $L$  and width  $W$  are 6 mm and 500  $\mu\text{m}$  respectively.

interconnects were plotted using the direct writing system. The interconnected sensors were then encapsulated with a layer of PDMS.

Integrated single strain gauges were characterized in the customized stretcher. The strain rate was fixed between 1.25 and 1 %/s when the number of strain cycles was below 100 and fixed to 5 %/s for larger number of cycles. Prior to single gauge or rosette characterization measurements, about 50 cycles up to 50% strain were applied to the structures in order to reach a stable regime for the electro-mechanical response of Au tracks[72].

## Results and discussion

The encapsulated liquid metal interconnects exhibited a low absolute resistance at zero strain ( $R_{w,EGaIn} \ll R_{\text{gauge,Au}}$ ) and a low relative and absolute increase in resistance compared to stretchable gold thin films ( $\Delta R_{w,EGaIn} \ll \Delta R_{\text{gauge,Au}}$ ). No significant difference was observed between the response of the integrated strain gauges and the bare gold tracks when a large number of strain cycles was applied (Figure 2.10). The strain sensitivity of the interconnects did not alter the thin Au film gauges' response to strain. The lower increase in resistance of the integrated strain gauge may have been explained by the presence of the encapsulation layer and by the dispersion of the gold tracks electrical characteristics due to the random nature of the microcracks. Furthermore, the absolute change in resistance of the soft gauges was more than two orders of magnitude higher than that of the liquid metal interconnects.

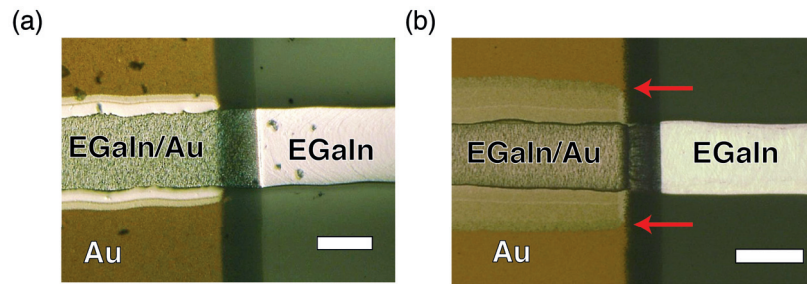


Figure 2.11 – Diffusion of EGaln into micro-cracked gold tracks. (a) Bottom of the contact zone between EGaln microwire and Au thin film on PDMS one week after integration. (b) Bottom of the contact zone between EGaln microwire and Au thin film on PDMS six months after integration. The arrows indicate the limit of the alloyed area. Scale bars are 200  $\mu\text{m}$ .

EGaln alloys with gold, forming a compound 100 times more resistive than bulk gold [138]. If this alloy sits underneath EGaln, it is electrically shorted by the liquid metal. However, as shown Figure 2.11 the alloy appeared to have diffused a few hundreds of microns around the contact point after six months storage in ambient conditions, resulting in a mean increase in base resistance of 42% (from  $92 \pm 4 \Omega$  to  $131 \pm 7 \Omega$  for  $5 \times 0.5 \text{ mm}^2$  tracks (mean $\pm$ s.d., n=3).

#### 2.2.4 Conclusion

I presented a plotting setup to serially draw micro wires of gallium indium eutectic. The liquid metal conductors were characterized by:

- a low sheet resistance (5 m $\Omega$ /sq for 40  $\mu\text{m}$  diameter wires).
- a predictable sensitivity to strain (gauge factor  $\approx 2$ ).

The wires could be drawn to arbitrary 2D designs and connected to highly resistive micro-cracked gold traces in order to form all-stretchable integrated strain gauges with high and localized strain sensitivity.

In the next section I present a novel parallel deposition process enabling batch patterning of liquid metal-based conductors down to 10  $\mu\text{m}$  critical dimensions.

---

## 2.3 Gallium-based biphasic (liquid-solid) and intrinsically stretchable thin films

### 2.3.1 Motivation

The high surface tension and the passivating oxide skin that spontaneously forms on the surface of liquid metals hinder their patterning using conventional techniques and especially the formation of thin films [50]. Alternative methods such as micro-plotting, which was reported in the previous section, do not offer high-resolution batch processing over large (wafer-scale) surface areas.

Physical vapor deposition (PVD) describes a range of methods, including thermal evaporation and sputtering, to deposit thin metal layers on large surface areas. PVD is deployed across many industries from microelectronics to food packaging. For instance, gallium is sputtered to form GaN, a common direct bandgap semiconductor. Interestingly, gallium was also thermally evaporated in its pure metal form on top of glass substrates pre-coated with a thin layer of gold [139]. The obtained morphology was drastically different from that of gallium evaporated on bare glass. However, PVD was never explored to form gallium-based stretchable conductors, in spite of the promise of unmatched electromechanical properties and patterning ability.

In this section, I report on the formation and characterization of stretchable gallium-based thin films formed by combining noble metals sputtering and gallium thermal evaporation.

### 2.3.2 Growth of the films

#### Materials and methods

**Deposition process** The deposition process is detailed in Appendix section A.1.3 page 118 and illustrated in Figure 2.12. In short, stencil masks were laminated on PDMS wafers, before sputtering 60 nm of gold and thermally evaporating 0.1 g to 1 g of gallium. After evaporation, the mask was removed from the substrate to reveal the desired pattern. The parameter  $\beta$  was defined as the atomic ratio ( $n_{Ga}/n_{Au}$ ) in the film. Before gallium evaporation,  $\beta = 0$ .

Since a standard thickness monitor could not be used, the deposited mass of gallium deposited per wafer was calibrated as a function of the gallium mass introduced in the thermal evaporator crucible (see Appendix section A.3 page 121).

**Surface and cross-section metrology** To assess the growth of the gold-gallium films, I analyzed their surface with scanning electron and atomic force microscopies. SEM images were acquired in a Merlin microscope (Zeiss) using the Everhart-Thornley (ET) detector at a beam

### 2.3. Gallium-based biphasic (liquid-solid) and intrinsically stretchable thin films

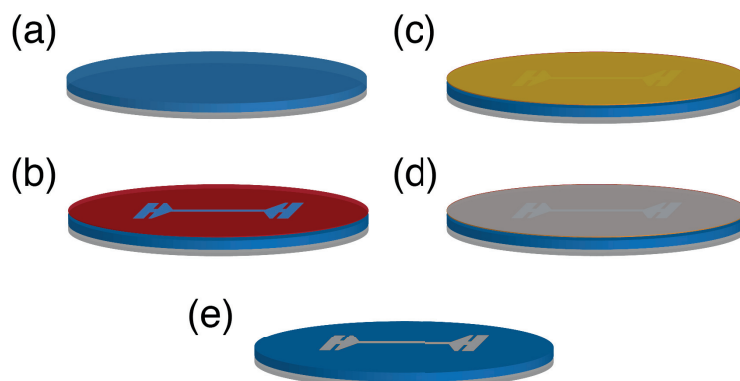


Figure 2.12 – Process flow for the deposition of gallium-based biphasic thin films. a) PDMS spin-coating. b) Shadow mask deposition or photoresist mask deposition and patterning. c) Au sputtering. d) Ga thermal evaporation. e) Mask removal.

energy of 22 keV to 3 keV for topography contrast, and the backscattered electron (BSE) detector at beam energy of 2 keV to 3 keV and grid voltage of 400 V for elemental contrast. Atomic force microscope (AFM) images were acquired in a Dimension Fastscan AFM (Bruker) with ScanAsyst-Air-HR probes from same supplier.

For larger area profilometry, I used a confocal laser microscope (LEXT OLS4100, Olympus, pixel size  $625 \times 625 \text{ nm}^2$ ), which has a maximum vertical accuracy of 200 nm and can image reflective samples with slopes up to  $85^\circ$ . I also utilized a white light interferometer (ContourGT-K, Bruker, pixel size  $1 \times 1 \mu\text{m}^2$ ) in vertical scanning interferometry (VSI) mode, which has a vertical resolution limit of 3 nm but cannot measure steep slopes on reflective materials.

For SEM cross-section observation, I peeled off a sample from the wafer and put a solid gallium crystal in contact with the film to initiate the crystallization of gallium. Then the sample was immersed in liquid nitrogen to cool it below the glass transition temperature of PDMS ( $-125^\circ\text{C}$ ). I initiated a crack on the side of the sample using scissors and eventually broke it in two parts using tweezers.

**Elemental mapping and X-ray diffraction analysis** Energy dispersive spectroscopy (EDS) data were acquired in the Merlin SEM at beam energy of 20 keV, using a  $50 \text{ mm}^2$  X-Max silicon drift detector (Oxford Instruments) and analyzed using Aztec software from the same supplier.

X-ray diffraction (XRD) analysis was conducted in a diffractometer (D8 Discover, Bruker) with

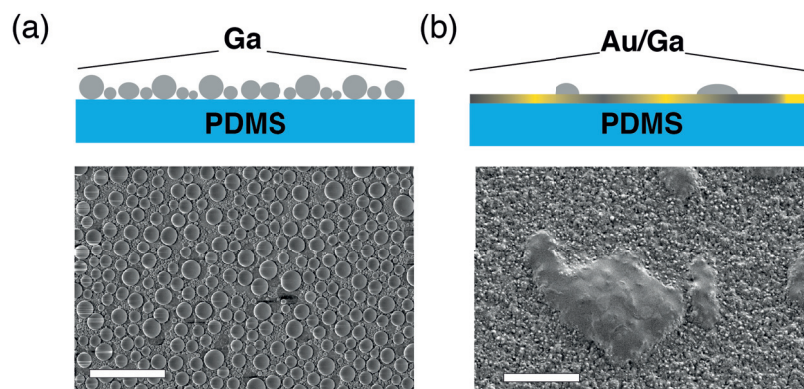


Figure 2.13 – Thermal evaporation of gallium on bare and gold-coated PDMS substrates. a) Schematic cross-section (top) and scanning electron microscope image (bottom) of gallium deposited by thermal evaporation on a bare PDMS substrate. The evaporated gallium condensed on the substrate to form a non-percolating layer of micro-droplets. b) Schematic cross-section (top) and scanning electron microscope image (bottom) of gallium deposited by thermal evaporation on PDMS substrate previously coated with sputtered gold (60 nm in thickness). The thin gold coating allows the gallium to spread by diffusing and alloying. Scale bars are 5  $\mu\text{m}$ .

a Cu  $K\alpha$  radiation ( $\lambda = 1.54 \text{ \AA}$ ,  $0.05^\circ$  steps, 2 s per step). All the samples were prepared and scanned on a float glass support wafer.

## Results and discussion

**Role of the Au underlayer** Gallium did not wet bare PDMS, which prevented the formation of an evaporated continuous liquid metal film on bare silicone substrates. Instead, the surface of the elastomer was covered with a non-conducting arrangement of liquid gallium microdroplets (Figure 2.13). In contrast, evaporating gallium on an alloying metal film, first deposited on the silicone surface, overcame the cohesive forces by allowing the liquid metal to diffuse, which further promoted the development of a continuous thin film.

The films' morphology and composition was drastically modified as more and more gallium was evaporated. The parameter  $\beta$ , defined as the atomic ratio ( $n_{Ga}/n_{Au}$ ) in the film, was used to quantify the amount of gallium deposited since it was not possible to use the thickness sensor of the evaporator.

**Growth stages** Figure 2.14 summarizes the growth stages of the biphasic film. The PDMS substrate was first coated with a 60 nm thick film of sputtered gold. The gold-coated PDMS surface revealed characteristic wrinkles resulting from compressive stress induced by thermal



### 2.3. Gallium-based biphasic (liquid-solid) and intrinsically stretchable thin films

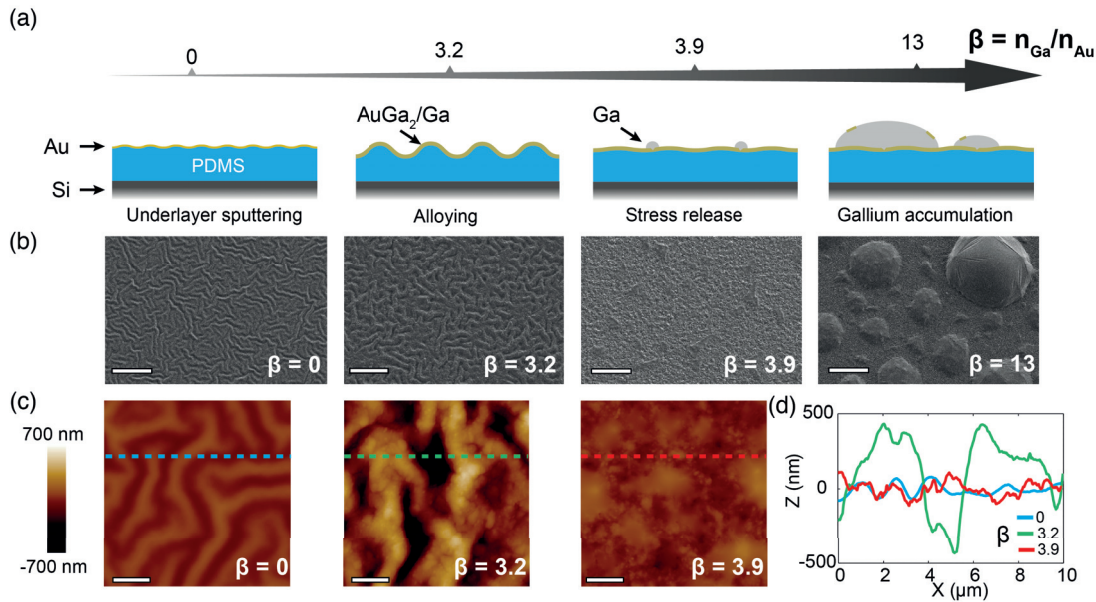


Figure 2.14 – Growth of biphasic gold-gallium thin films on a PDMS membrane. a) Schematic representations of the various structural regimes of the biphasic film on a PDMS substrate as a function of the gallium/gold atomic ratio,  $\beta$ . b,c) SEM and atomic force microscopy (AFM) images of the surface of the biphasic films deposited on PDMS substrates as a function of increasing  $\beta$  ratio. SEM scale bars are 10  $\mu\text{m}$ . AFM scale bars are 2  $\mu\text{m}$ . d) Cross-section profiles along the dotted lines indicated on the AFM scans displayed in (c).

expansion of the elastomeric substrate during deposition of the metal film [140]. Gallium was then deposited by thermal evaporation. For  $\beta = 3.2$ , the gold film completely alloyed with the evaporated gallium to form the intermetallic compound AuGa<sub>2</sub> (Figure 2.15) and pronounced buckling with micrometer amplitude and wavelength was observed. Gold-gallium alloying results in large volume expansion (340%) of the film as the lattice constant of the metal increases from 4.08  $\text{\AA}$  in pure gold to 6.08  $\text{\AA}$  in AuGa<sub>2</sub> [141]. This likely induced larger compressive stress in the thin film on the PDMS substrate, amplifying its wavy topography. The XRD scans did not reveal presence of Ga in a solid phase. It indicated that although the samples were cooled down to room temperature, below Ga fusion point (29.8  $^{\circ}\text{C}$ ), gallium remained in a liquid phase. This phenomenon is known as supercooling and gallium as been shown to supercool down to 70  $^{\circ}\text{C}$  below its fusion point when constrained into microscopic droplets [142].

For a ratio of 3.9, the metallic film on PDMS was surprisingly flat, with a surface roughness close to that of the bare sputtered gold layer. This was also concomitant to the accumulation of the liquid gallium in microscopic bulges (of  $<1 \mu\text{m}$  size) on top of the alloyed film. I propose that this flattening results from the release of the compressive stress by cracking and/or delamination of the intermetallic alloy [143]. Adding more gallium ( $\beta = 13$ ) increased the volume of the liquid bulges further while the rest of the AuGa<sub>2</sub>/Ga film remained flat (see also

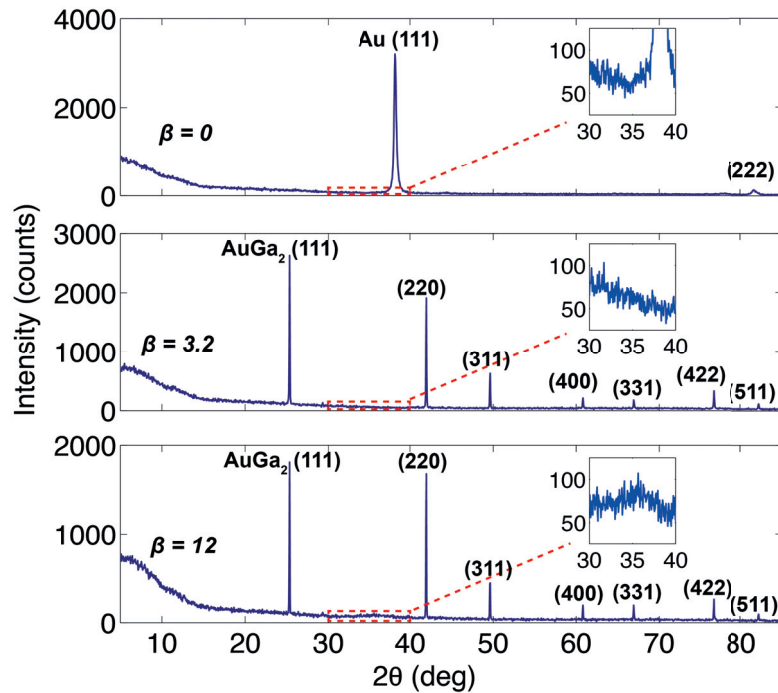


Figure 2.15 – X-Ray diffraction analysis of biphasic gold-gallium thin film. The peaks corresponding to Au (for  $\beta = 0$ , ICDD PDF Card 00-004-0784) and  $\text{AuGa}_2$  (for  $\beta = 3.2$  and  $\beta = 12$ , ICDD PDF Card 01-072-5268) are identified. Insets show the increase in baseline signal around  $2\theta = 35^\circ$  attributed to liquid gallium [144].

Figure 2.16).

**Film topography** A cross section of the film is visible in Figure 2.17, while representative film topography measured by optical profilometry is illustrated Figure 2.18. At  $\beta = 13$ , bulges could reach up to  $100\ \mu\text{m}$  in circumference and up to  $20\ \mu\text{m}$  in height. More than 80% of the film surface area remained under  $1\ \mu\text{m}$ , and more than 97% remained under  $5\ \mu\text{m}$ . From topographic measurements, I could use a feature recognition algorithm detailed in Appendix A.4 page 123 to identify the bulges at the surface of the film (Figure 2.18c). The mean measured thickness of the flat portions of the film at the center of a wafer over about  $0.5\ \text{mm}^2$  was  $370\ \text{nm}$  with a mean RMS roughness of  $80\ \text{nm}$  (see Appendix A.4 page 123). The mean measured thickness corresponded to the thickness of the alloy shown in Figure 2.17, while the RMS roughness value was in agreement with the AFM measurements in Figure 2.14d.

### 2.3. Gallium-based biphasic (liquid-solid) and intrinsically stretchable thin films

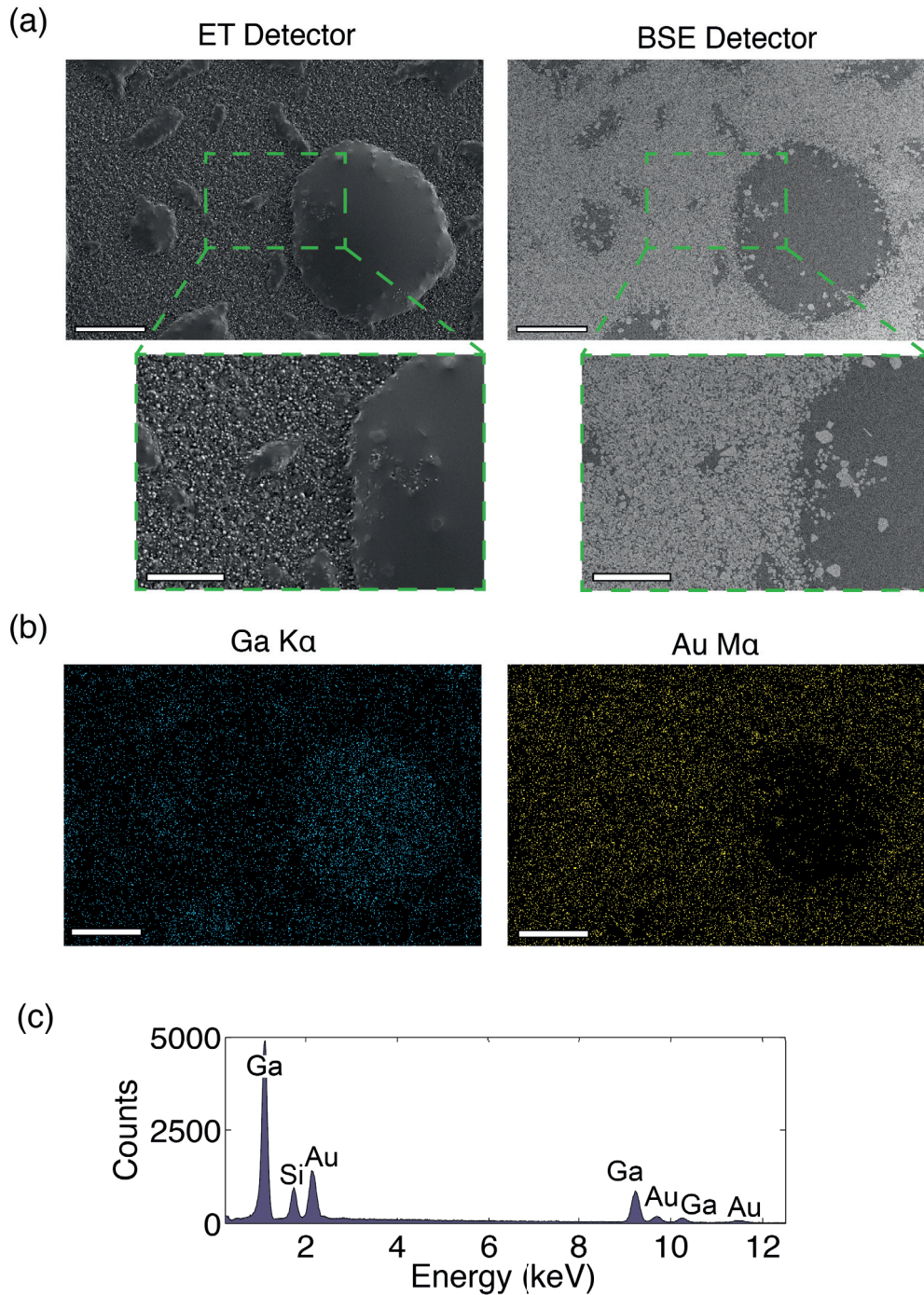


Figure 2.16 – EDS-SEM analysis of the gold-gallium films. a) SEM images of the surface of a biphasic gold-gallium thin film deposited on a PDMS substrate with Ga/Au atomic ratio  $\beta = 13$ . Left-hand images were acquired with an Everhart-Thornley (ET) detector. Right-hand images were acquired using a backscattered electron (BSE) detector. Scale bars are 10  $\mu\text{m}$  (5  $\mu\text{m}$  in the magnified views). b) Energy-dispersive X-Ray spectroscopy (EDS) mapping of the area observed in (a) for gold and gallium. Scale bars are 10  $\mu\text{m}$ . c) EDS spectrum corresponding to the entire mapping area shown in (b).

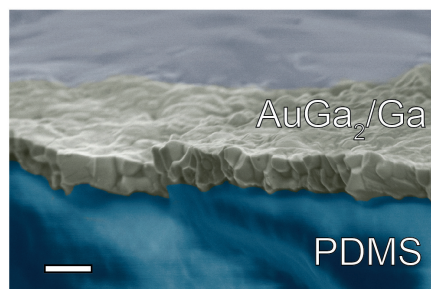


Figure 2.17 – False color scanning electron microscopy (SEM) image of a slightly tilted cross-section of the biphasic gold–gallium film on a PDMS substrate. The blue, yellow and gray colors correspond to the PDMS substrate, the biphasic AuGa<sub>2</sub>/Ga film, and a gallium bulge in the background, respectively. Scale bar is 500 nm.

### 2.3. Gallium-based biphasic (liquid-solid) and intrinsically stretchable thin films

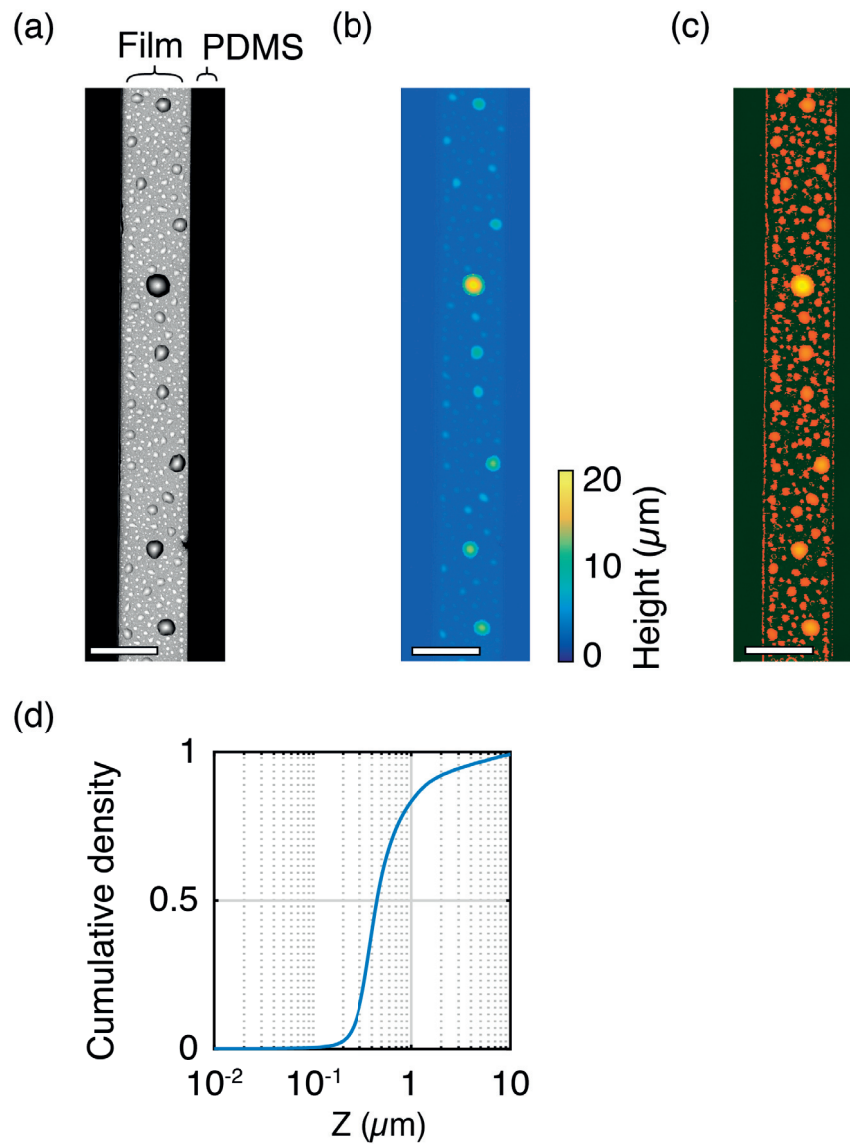


Figure 2.18 – Topography of a biphasic film track. a) Confocal laser microscope image of a track. Scale bar is 300 μm. b) Corresponding profile map. Scale bar is 300 μm. c) Corresponding identification of bulges using feature recognition algorithm. Bulges are identified in red. Scale bar is 300 μm. d) Empirical cumulative density for the thickness in the film area.

---

### 2.3.3 Electromechanical characterization

#### Materials and methods

Biphasic gold-gallium thin film conductors were stencil-patterned on 120  $\mu\text{m}$  thick PDMS to produce 15 mm long and 0.3 mm wide electrical conductors with four contacts pads (Figure 2.19). Samples were subsequently cut in  $10 \times 30 \text{ mm}^2$  rectangles and peeled from the wafer. Samples were mounted on the custom-built uniaxial tensile stretcher described section 2.1.2 page 21. Each clamp featured two contact pads that provided constant electrical and mechanical contact to the sample under test. The position of the clamps and the electrical resistance of the conductor, measured using the four-wire sensing method.

The conductors were first cycled twenty times to up to 0.1 applied strain. Next, every 20 stretch cycles, the maximal applied strain was increased by 0.1 to reach a maximal strain of 0.8. For fatigue experiments, the stretcher was programmed to perform one million stretch-relaxation cycles (0 to 0.5 strain at a frequency of 1.4 Hz). Ten times per decade, counting cycles on a logarithmic scale, the stretcher slowed to 0.14 Hz for 5 cycles in order to record the position of the clamps and resistance of the sample.

For SEM observation under strain, the samples were cut, peeled from their carrier wafer and mounted on a manual aluminum uni-axial stretcher. Controlled strain was applied to stretch the soft samples to a strain  $\epsilon$ . For SEM observation under strain, the samples were stretched using a manual stretcher which was subsequently loaded into the SEM chamber and imaged using identical parameters to those selected for (unstrained) samples imaged on carrier wafers.

### 2.3. Gallium-based biphasic (liquid-solid) and intrinsically stretchable thin films

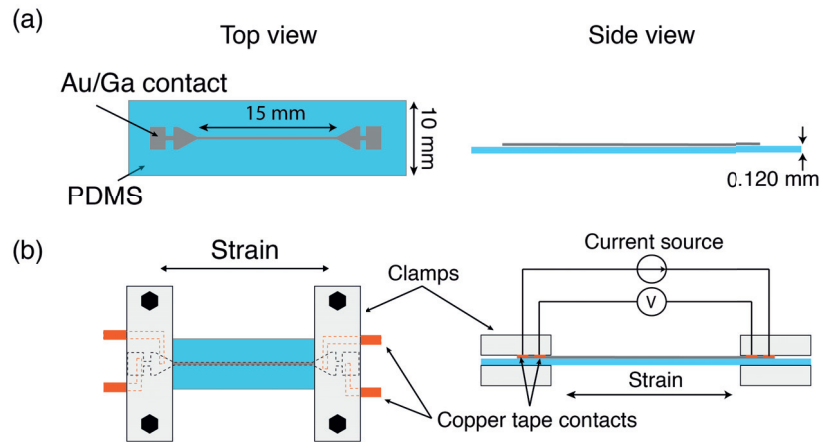


Figure 2.19 – Samples and setup for electromechanical characterization of biphasic thin films. a) Top (left) and side (right) schematics of the biphasic gold-gallium thin film on a PDMS substrate used for electromechanical characterization. The biphasic thin film was patterned using a stencil mask to produce 15 mm long and 0.3 mm wide conductive tracks featuring large contacts at the extremities. b) Top (left) and side (right) schematics of clamped samples for electromechanical characterization. Each clamp featured two contact pads that enabled constant electrical and mechanical contact with the tested sample. The resistance of the track, measured using the four-wire sensing method, and the position of the clamps were measured synchronously.

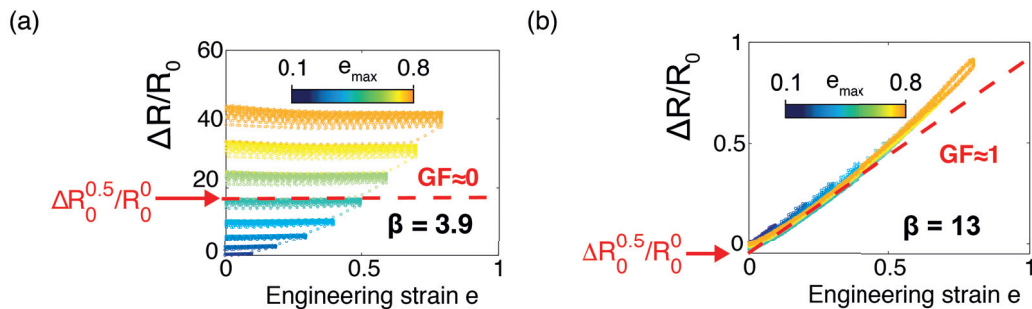


Figure 2.20 – Relative change in electrical resistance as a function of applied engineering strain  $e$  of biphasic conductive tracks prepared with atomic ratio  $\beta$  of 3.9 (a) and 13 (b). The conductors were first cycled twenty times to 0.1 applied strain. Next, every 20 stretch cycles, the maximal applied strain was increased by 0.1 to reach a maximal strain of 0.8. The gauge factor (GF) is calculated from the slopes of the red dashed lines. The relative increase in resistance at rest after cycling to 0.5 applied strain,  $\Delta R_0^{0.5}/R_0^0$ , is also indicated.

---

## Results and discussion

The biphasic conductors were characterized during uni-axial stretching cycles with four-wire sensing resistance measurements and scanning electron microscopy (Figures 2.20, 2.21 and 2.22). Films prepared with  $\beta < 3.2$  were conductive after fabrication but failed with catastrophic cracking during release from the carrier substrate and subsequent handling. For  $\beta = 3.9$ , the films maintained electrical conduction when strained up to 0.8. For large deformations (strain  $> 0.1$ ), the amount of liquid gallium available was not sufficient to prevent the formation of cracks thereby leading to irreversible damage in the film and permanent degradation of its macroscopic electrical conductivity (Figures 2.20 and 2.21).

In films prepared with  $\beta > 6$ , liquid gallium percolated throughout the AuGa<sub>2</sub> clusters and maintained electrical continuity in the tested strain range (0 to 0.8 strain) (Figure 2.21). Scanning electron microscopy images suggested the biphasic film maintained its continuity as gallium filled the cracks in the solid AuGa<sub>2</sub> matrix.

Next, assessment of the initial sheet resistance, the gauge factor and relative change of resistance at relaxed state (0 strain) after twenty stretching cycles (0 to 0.5 strain) was performed (Figure 2.22).

The relative change of resistance after cycling at 0.5 strain was defined as:

$$\Delta R_0^{0.5} = \frac{R_0^{0.5} - R_0}{R_0} \quad (2.3)$$

where  $R_0^{0.5}$  is the measured resistance at 0 strain after the sample has been stretched 20 times to 0.5 strain, and  $R_0$  is the initial resistance of the conductor.

The gauge factor (GF) was computed as the slope of the relative change of resistance as a function of the applied strain, and computed using a linear fit on the last cycle at 0.5 maximal applied strain.

It was found that for sufficiently high atomic ratios ( $\beta > 6$ ), the biphasic films combined low sheet resistance ( $< 1 \Omega/\text{sq}$ ), low gauge factor ( $\approx 1$ ) and no dependence on strain history. In brief, the elemental composition of the biphasic films defines their electromechanical response:

- for  $3.2 < \beta < 6$ , the electrical conduction of the film displays strain-history dependence.
- for  $\beta > 6$ , the film displays high conductivity regardless of the strain history.

To demonstrate the electromechanical robustness and assess fatigue resistance of the biphasic



### 2.3. Gallium-based biphasic (liquid-solid) and intrinsically stretchable thin films

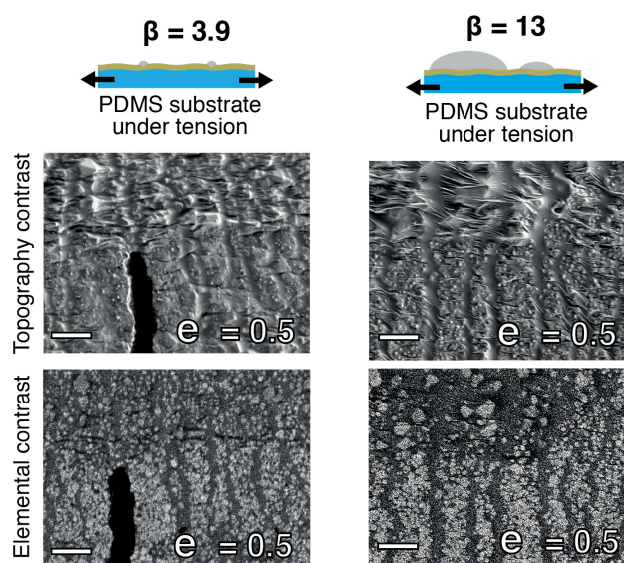


Figure 2.21 – SEM images of the surface of biphasic gold-gallium thin films prepared with atomic ratio  $\beta$  of 3.9 and 13 on PDMS substrates. Top and bottom SEM images were obtained with the Everhart-Thornley (ET) detector for topographical contrast, and the backscattered electron (BSE) detector for elemental contrast, respectively. Scale bars are  $2\ \mu\text{m}$ .

films, a conductor ( $\beta = 13$ ) was stretched to 0.5 strain one million times over a period of one week (Figure 2.23a). The film withstood the cyclic deformation, displaying minimal variation in resistance over time. When processed on a polyurethane substrate, the biphasic metallization ( $\beta = 5.2$ ) sustained reliably uniaxial stretching to five times its initial length (Figure 2.24b-c). A PDMS membrane hosting biphasic conductors ( $\beta = 13$ ) was radially stretched to three times its initial surface area. The PDMS membrane fractured before the biphasic conductors electrically failed (Figure 2.25).

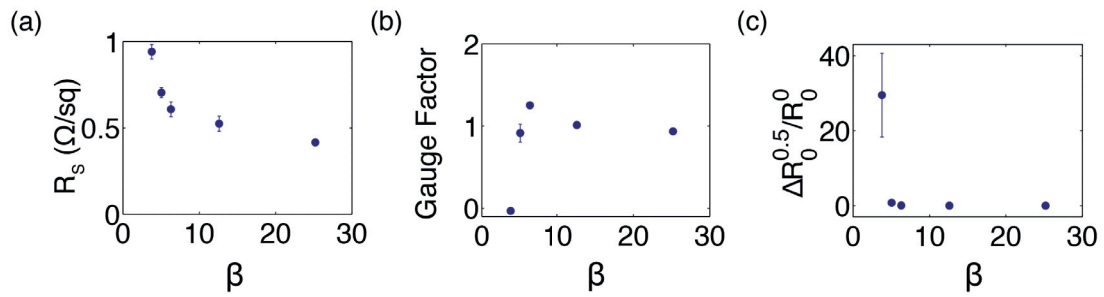


Figure 2.22 – a) Initial sheet resistance ( $e = 0$ ), (b) gauge factor (calculated over 0.5 strain cycle), and (c) relative change in electrical resistance ( $e = 0$ ) after cycling to 0.5 maximum applied strain for increasing  $\beta$  ratios ( $n = 3$  samples, error bars: s.d.).

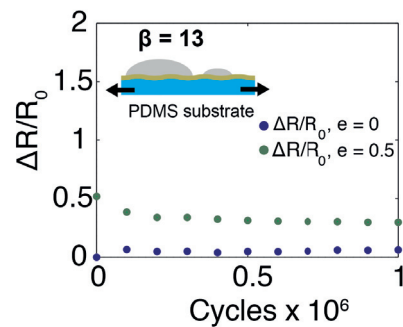


Figure 2.23 – Fatigue test for the biphasic gold-gallium thin films. Relative change in electrical resistance over one million cycle to 0.5 strain of a biphasic gold-gallium conductor prepared with the atomic ratio  $\beta = 13$ .

### 2.3. Gallium-based biphasic (liquid-solid) and intrinsically stretchable thin films

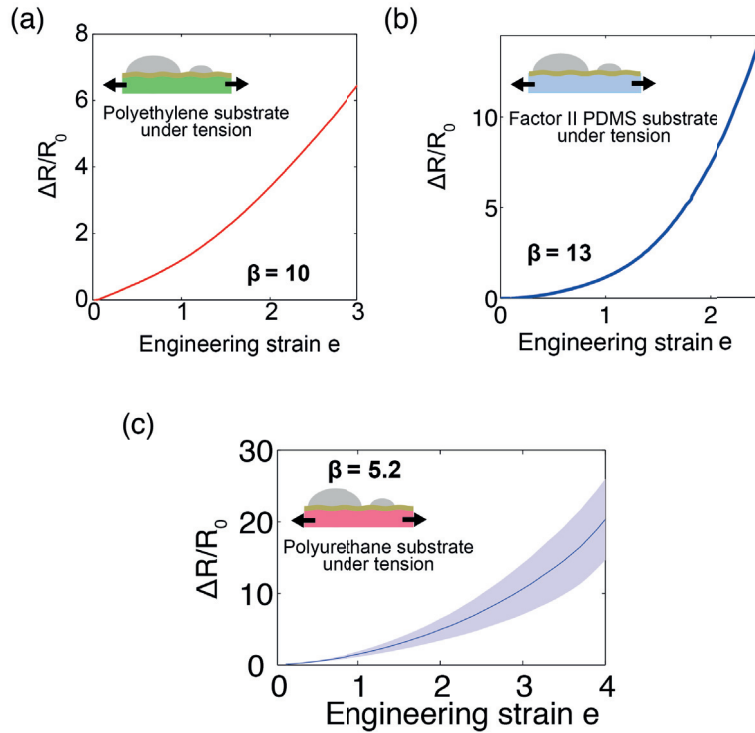


Figure 2.24 – Test to very large (>2) strains for the biphasic gold-gallium thin films. a) Relative change in electrical resistance of a biphasic gold-gallium conductor prepared with the atomic ratio  $\beta = 5.2$  deposited on a  $250\mu\text{m}$  thick polyurethane substrate (Inspire 7250, Coveris). (average over  $n = 10$  samples, shaded area represent s.d.). b) Relative resistance change as a function of engineering strain  $e$  for a gold-gallium biphasic film deposited on a  $10\mu\text{m}$  thin polyethylene substrate (Ideal, Weita) with the atomic ratio  $\beta = 10$ . Initial sheet resistance of the sample was  $0.6\Omega/\text{sq}$ . c) Relative resistance change as a function of engineering strain  $e$  for an gold-gallium biphasic film deposited on a  $120\mu\text{m}$  thin PDMS substrate (A-221-05, Factor II) with the atomic ratio  $\beta = 13$ . Initial sheet resistance of the sample was  $0.6\Omega/\text{sq}$

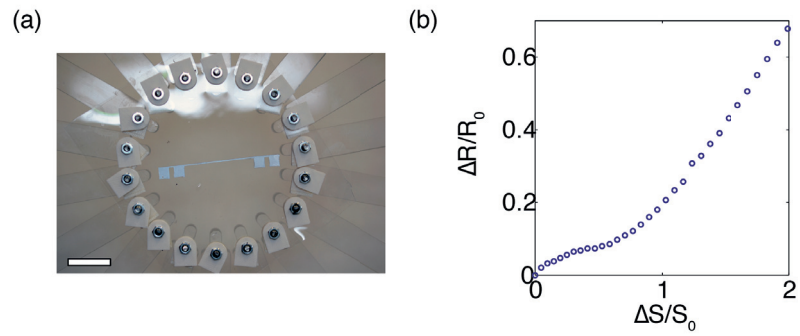


Figure 2.25 – Radial stretching of the biphasic gold-gallium thin film conductors on a PDMS substrate. a) Picture of a  $35 \times 0.5 \text{ mm}^2$  track in the radial stretcher. Scale bar is 20 mm. b) Relative increase in resistance of the track, measured using the four-wire sensing resistance measurement method, as a function of the relative increase in surface area of the support membrane.

## 2.3. Gallium-based biphasic (liquid-solid) and intrinsically stretchable thin films

---

### 2.3.4 Micro-patterning

#### Materials and methods

A fabrication process flow was designed to enable photoresist spin-coating, curing and removal directly on a PDMS substrate. The very high thermal expansion coefficient of PDMS ( $300 \text{ ppm K}^{-1}$  [43]) and potential swelling by solvents [41] imposed some process constraints:

- the uncured photoresist should not swell the PDMS.
- the maximum process temperature and temperature gradients had to be kept to a minimum to avoid catastrophic cracking of the photo-resist.
- the solvent used for resist removal should not swell PDMS nor attack the metallization.

The lift-off process is detailed in Appendix section A.1.3 page 118. To summarize it quickly, 40 nm of gold were sputtered and 0.2 g of gallium were evaporated after photoresist deposition and patterning. The resist was then stripped to reveal the patterns before drying the samples.

The root mean square (RMS) edge roughness of the lines patterned by lift-off was derived from a series of optical microscope images using the Analyze-Stripes macro for ImageJ [145].

#### Results and discussion

I achieved a critical dimension of  $10 \mu\text{m}$  (Figure 2.26). Arbitrary 2D shapes were produced across an extended area (more than  $50 \times 80 \text{ mm}^2$ ) while maintaining sharp features (RMS edge roughness of  $2.7 \mu\text{m}$  for a  $10 \mu\text{m} \times 15 \text{ mm}$  line, see also Figure 2.27), and I confirmed the exceptional electromechanical performance of the micropatterned conductive tracks (Figure 2.28).

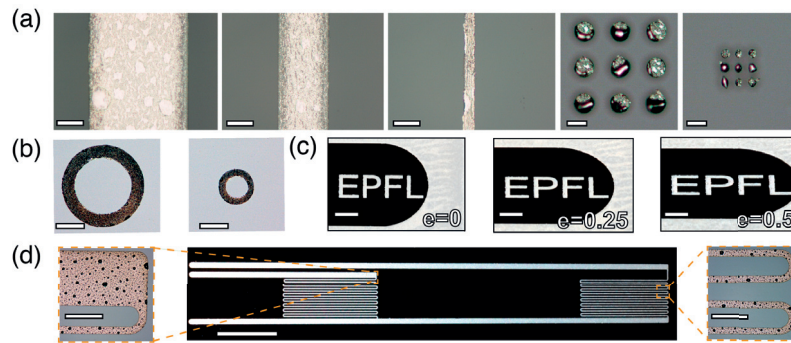


Figure 2.26 – Micropatterning of biphasic gold-gallium conductors on PDMS substrates with lift-off processing. a) Optical microscope images of (left to right) 100  $\mu\text{m}$ , 50  $\mu\text{m}$ , and 10  $\mu\text{m}$  wide tracks and 3 $\times$ 3 matrices of 25  $\mu\text{m}$  and 10  $\mu\text{m}$  diameter dots of biphasic thin films patterned with a photolithographic lift-off process. Scale bar: 25  $\mu\text{m}$ . b-c) Arbitrary patterns of biphasic gold- gallium thin films on PDMS substrates. Scale bars are 250  $\mu\text{m}$  (b) and 1 mm (c). d) Pictures of patterns developed over large-area surfaces. Scale bars are 10 mm (main picture) and 500  $\mu\text{m}$  (insets).

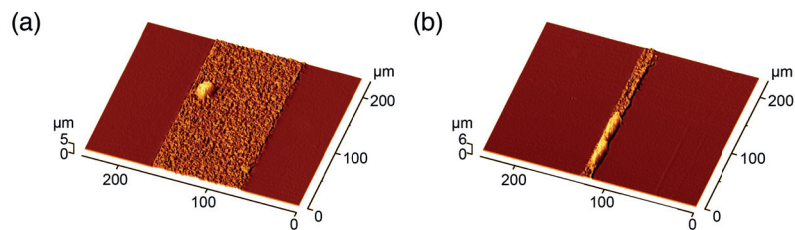


Figure 2.27 – 3D reconstruction of micro-patterned biphasic gold-gallium tracks from optical profilometer measurement. a) Portion of a 100  $\mu\text{m}$  wide track. b) Portion of a 10  $\mu\text{m}$  wide track.

### 2.3. Gallium-based biphasic (liquid-solid) and intrinsically stretchable thin films

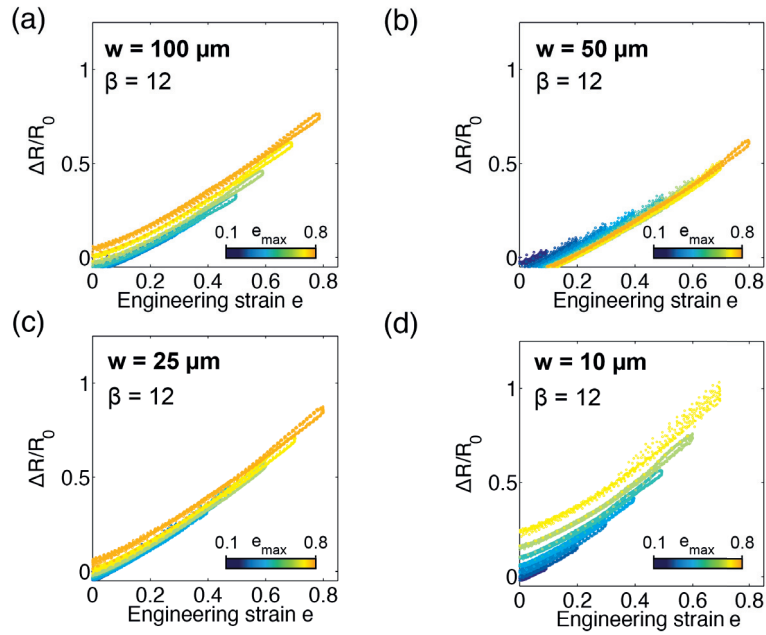


Figure 2.28 – Electromechanical characterization of micro-patterned biphasic gold-gallium tracks. Relative resistance change during incremental stretching of (a)  $100 \mu\text{m} \times 15 \text{ mm}$ , (b)  $50 \mu\text{m} \times 15 \text{ mm}$ , (c)  $25 \mu\text{m} \times 15 \text{ mm}$ , and (d)  $10 \mu\text{m} \times 15 \text{ mm}$  biphasic gold-gallium tracks measured using the four-wire sensing method. Initial sheet resistances were  $0.8 \Omega/\text{sq}$ ,  $0.7 \Omega/\text{sq}$ ,  $0.6 \Omega/\text{sq}$  and  $0.4 \Omega/\text{sq}$ , respectively.

‡

---

### 2.3.5 Investigation of other solid metallic under-layers

#### Materials and methods

The samples were prepared and tested as described in section 2.3.3 page 40. Three alternative to Au underlayers were sputtered (DP 650, Alliance Concept) before gallium thermal evaporation: Pd (60 nm), Pt (60 nm) and Ir (60 nm). Only noble metals were investigated since surface oxidation of non noble metal seemed to prevent the formation of the biphasic thin films. Al and Cu were also considered but gallium did not wet the surface of sputtered Cu, and films with Al underlayer failed at strains below 0.8.

#### Results and discussion

Films prepared with a Pd underlayer could maintained their continuity up to 0.8 strain (see Figure 2.29) and displayed electromechanical performance similar to films prepared with Au underlayer for every tested metric as illustrated in Figure 2.30. On the contrary, cracks appeared in samples prepared with Pt and Ir, leading to degraded electromechanical performance (large increase in baseline resistance after cycling to 0.5 strain). It highlighted the importance of the interaction between the substrate, the solid metal underlayer and the liquid gallium to obtain high performance biphasic thin metallic films.



### 2.3. Gallium-based biphasic (liquid-solid) and intrinsically stretchable thin films

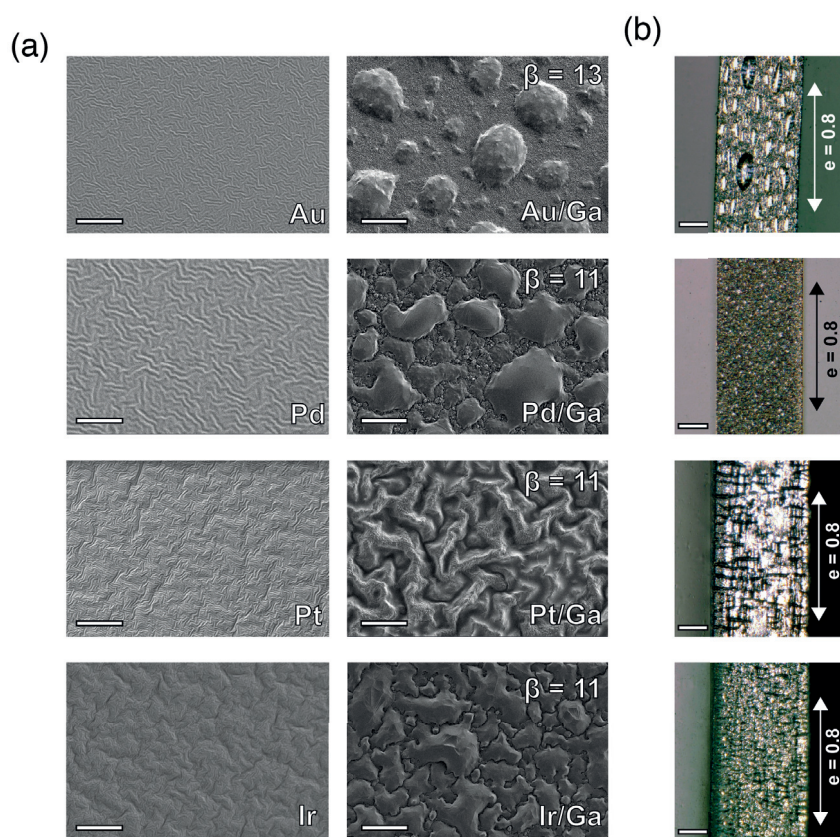


Figure 2.29 – Biphasic gallium-based thin films on PDMS substrates with Au, Pd, Pt and Ir underlayers. a) SEM images of the surface of films after sputter deposition of the 60 nm metal layer on a PDMS substrate (left) and after the subsequent gallium thermal evaporation (right). Scale bars are 20  $\mu\text{m}$ . b) Optical microscope images of 300  $\mu\text{m}$  wide tracks of the biphasic films under 0.8 applied mechanical strain. Scale bars are 100  $\mu\text{m}$ .

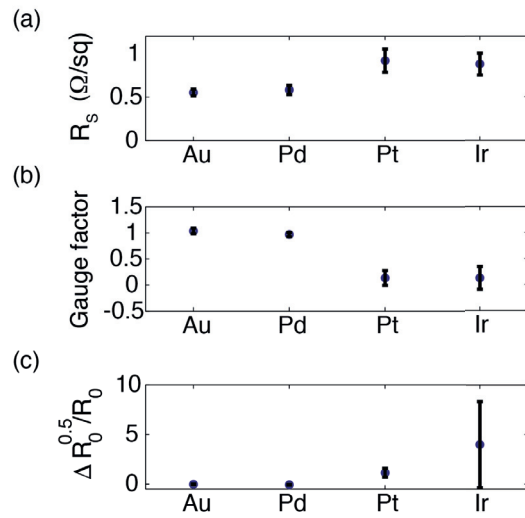


Figure 2.30 – Electromechanical characterization of biphasic films with Au, Pd, Pt and Ir underlayers. a) Sheet resistance, (b) gauge factor and (c) relative change in baseline resistance at zero strain after the tracks were stretched to 0.5 strain. Corresponding atomic ratios ( $n_{metal}/n_{Ga}$ )  $\beta$  are 13 for Au, 11 for Pt, 11 for Pt and 11 for Ir. ( $n = 4$  for each data point, error bars: s.d.).

### 2.3.6 Liquid electromigration under DC current in biphasic thin films

#### Electromigration in solid and liquid conductors

Electromigration in solid metals refers to the displacement of the conductor's atoms under the action of an electrical current and has an important influence on the reliability of integrated circuits [146]. It results from collisions between the free electrons and the atoms of the conductor. Following the "electron wind" direction, the metal atom diffuses towards the anode, preferably through grain boundary vacancies in polycrystalline thin films.

Dutta and coworkers reported extensively on macroscopic electromigration of liquid metals, and gallium in particular [147–149]. The electromigration force exerted on the metal ions of the lattice is the resultant of two forces with opposite direction, the electrostatic force and the force exerted by the electron wind. The total force is:

$$\vec{F} = (Z + Z_w)e\vec{E} = Z^*e\vec{E} \quad (2.4)$$

with  $Z$  the ion valence,  $Z_w$  the valence resulting from ion-electron wind coupling, and  $Z^*$  the effective valence accounting for both wind and electrostatic forces,  $\vec{E}$  the electric field, and  $e$  the elementary charge [146]. In solid conductors, the wind force dominates:  $Z^* < 0$  and electromigration occurs in the direction opposite to the electrical field (from cathode to anode). In liquid conductors, the electrostatic force dominates:  $Z^* > 0$  and electromigration occurs in the direction of the electrical field (from anode to cathode) [147, 148].

In thin films metallic interconnects, the mean time to failure  $t_{\text{fail},50}$  is empirically described by the generalized Black's equation [150, 151]:

$$t_{\text{fail},50} = \frac{A}{j^n} e^{\frac{E_a}{kT}} \quad (2.5)$$

where  $A$  is a constant,  $E_a$  is the activation energy for failure,  $k$  is the Boltzmann constant, and  $T$  is the temperature.

#### Materials and methods

**Samples preparation** Samples were prepared as described in Appendix section A.1.3 page 118. In short, glass wafer were coated with a 120  $\mu\text{m}$  layer of PDMS cured at 80  $^\circ\text{C}$ . 60 nm of gold was sputtered and gallium was thermally evaporated to reach an atomic ratio  $\beta = 13$ .  $1 \times 15 \text{ mm}^2$  conductive tracks terminated by connection pads were patterned using stencil masks.

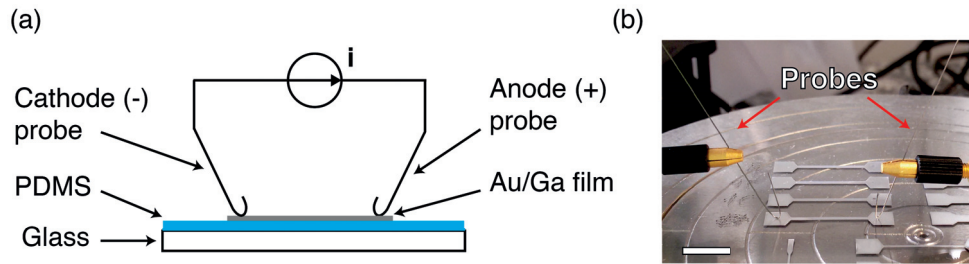


Figure 2.31 – Test set-up for liquid electro-migration measurement. a) Schematic representation of the test set-up. b) Picture of a sample under test. Scale bar is 10 mm.

**Samples testing** Figure 2.31 shows a schematic of the testing set-up. Wafers were placed in a probe station (MPS 150, Cascade Microtech). I probed the tracks using curved tungsten wires (99.9% purity, 0.25 mm diameter, Electron Microscopy Sciences) mounted on micrometric positioning probes (DPP210, Cascade Microtech). Tungsten was chosen as contacting material since it is resistant to corrosion by gallium [152]. The mean interprobe distance was  $18.0 \pm 0.3$  mm (mean $\pm$ S.D.,  $n=15$ ). Direct current was passed through the tracks and the resistance was recorded using a source-meter (2400, Keithley).

**Sample observation** Samples were observed using an optical microscope (Eclipse, Nikon) and a scanning electron microscope (SEM) (Merlin, Zeiss). Energy dispersive spectroscopy (EDS) data were acquired in the SEM at beam energy of 20 keV, using a 50 mm<sup>2</sup> X-Max silicon drift detector from Oxford Instruments and analyzed using Aztec software from same supplier.

## Results and discussion

**Resistance variation** As shown Figure 2.32 the resistance of the tracks increased dramatically over time when a DC current passed through. The initial mean resistance  $R_0$  of the samples was  $11.6 \pm 0.9 \Omega$  (mean $\pm$ s.d., 15 samples). In microelectronics reliability studies, the failure time of an interconnect is typically defined as a fixed percentage increase from its initial resistance [153–155]. In this study, I defined the failure time  $t_{fail}$  as the time when the resistance of the sample reached  $10R_0$  (represented by solid lines Figure 2.32a). The failure time followed an inverse power law relationship as a function of the applied current  $i$ :  $t_{fail} \propto i^{-n}$  with  $n = 3.2$ . As reported in Appendix A.5 page 125, the time to ultimate failure followed the same trend for the fourteen samples tested until an open circuit condition was reached.

From measurements of the contact area at the probes ( $A_{contact} = 49 \pm 3 \times 10^3 \mu\text{m}^2$ , mean $\pm$ s.d.,  $n=3$ ), I estimated the current density  $j$  at the probe/film contact area between  $100 \text{ A cm}^{-2}$  (for  $i=50 \text{ mA}$ ) and  $5 \text{ A cm}^{-2}$  (for  $i=2.5 \text{ mA}$ ).

### 2.3. Gallium-based biphasic (liquid-solid) and intrinsically stretchable thin films

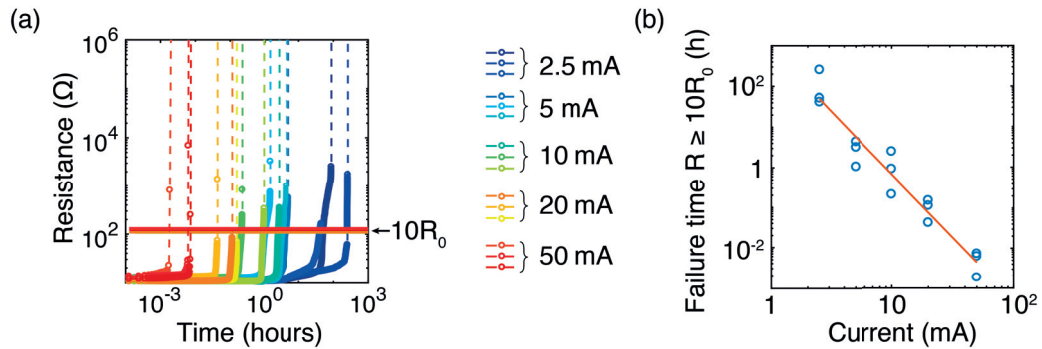


Figure 2.32 – a) Resistance of samples as a function of time for DC currents of 2.5 mA to 50 mA. b) Failure time as a function of DC current amplitude for the 15 tested samples.  $R^2 = 0.93$  for linear fit.

**Change in film aspect and composition** I observed a drastic change in film aspect in the area around the tungsten probes (Figure 2.33). Before failure and after probing, both anode and cathode contact areas had a metallic aspect. After failure, the anode area took a dark aspect, with scattered metallic clusters. On the contrary, the cathode area conserved its original metallic aspect. Liquid gallium bulges remained in the cathode area whereas they disappeared in the anode area.

EDS-SEM analysis after electrical failure revealed that in the anode area, gallium and gold were almost exclusively concentrated into the microscopic metallic clusters, while they were evenly distributed in the cathode area (Figure 2.34). The metallic micro-clusters were composed of disjointed crystallites as shown Figure 2.35 which I identified as  $\text{AuGa}_2$  intermetallic alloy [125].

**Evidence for liquid electromigration** In brief, I observed two phenomena:

- gallium is depleted in the anode area and accumulates in the cathode area.
- the failure time follows an inverse power law function of the applied DC current in the tracks.

There is thus a transport of gallium from anode to cathode, leading to a failure of the interconnects following the empirical Black's equation.

Taken together with literature described above, the experimental results show that liquid electromigration occurs in biphasic gallium-based thin films. If a significant current must pass through the biphasic thin film interconnects, mitigation strategies such as alternative current

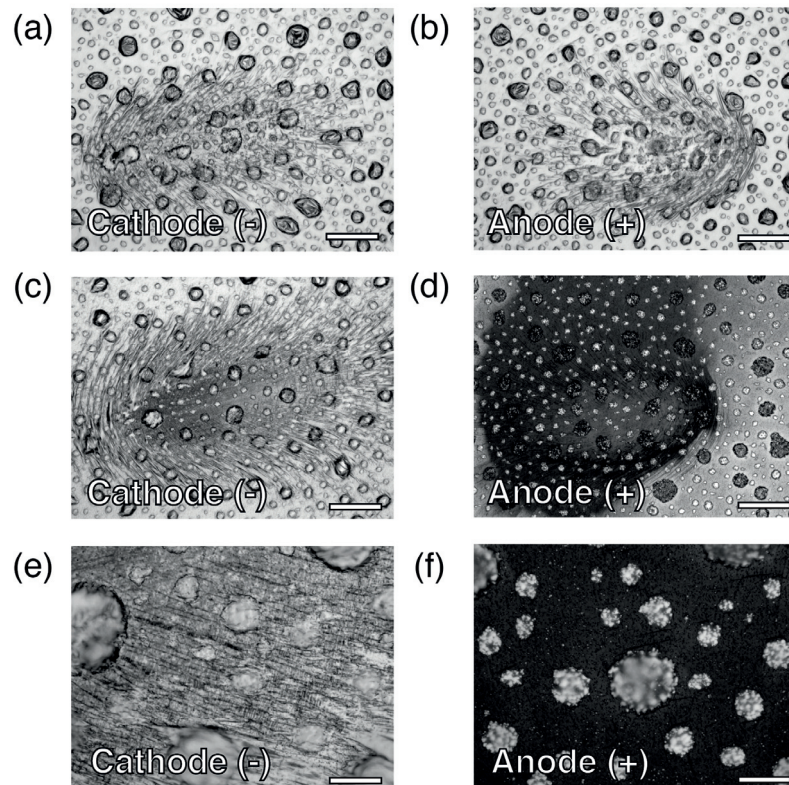


Figure 2.33 – Biphasic film aspect before and after electrical failure, observed using an optical microscope. a-b) Typical aspect of cathode and anode areas after probing and before failure. Scale bars are 100  $\mu\text{m}$  c-d) Typical aspect of cathode and anode area after failure. Scale bars are 100  $\mu\text{m}$  e-f) Cathode and anode area after failure at higher magnification. Scale bar is 20  $\mu\text{m}$ .

(AC) or pulsed DC powering can be considered to extend devices lifetime [156]. Increasing the films uniformity to decrease the current density for a fixed deposited gallium quantity should also mitigate the effect of electromigration.

### 2.3. Gallium-based biphasic (liquid-solid) and intrinsically stretchable thin films

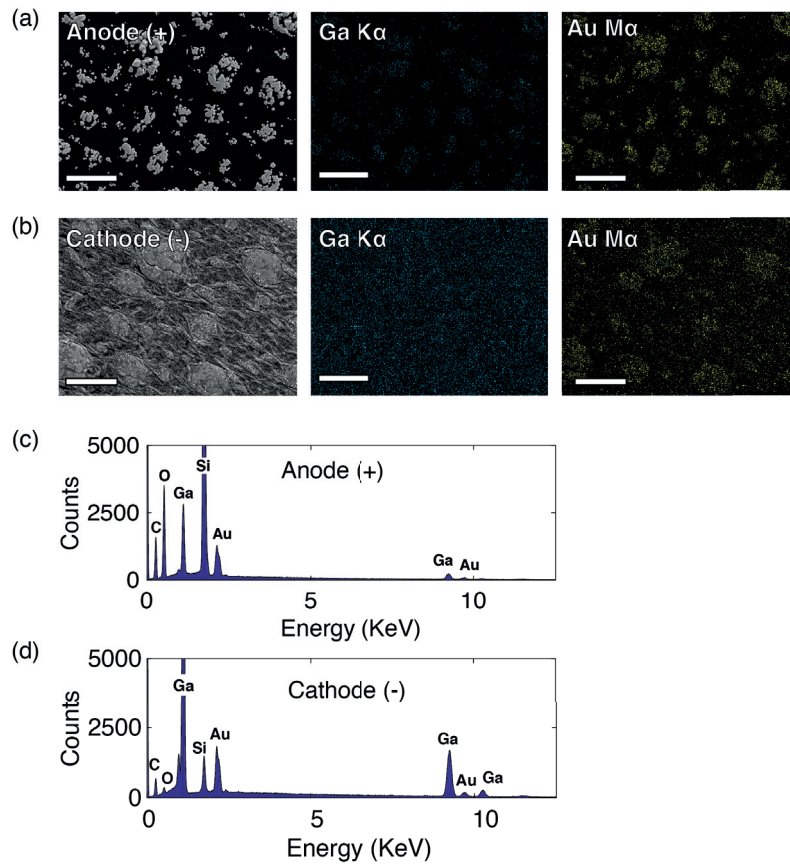


Figure 2.34 – EDS-SEM analysis of the cathode and anode areas after electrical failure. a) SEM image and EDS elemental mapping for Ga and Au in the anode area after electrical failure. Scale bars are 25  $\mu\text{m}$ . b) SEM image and EDS elemental mapping for Ga and Au in the anode area after electrical. Scale bars are 25  $\mu\text{m}$ . c-d) EDS spectra corresponding to the entire elemental maps in (a) and (b).

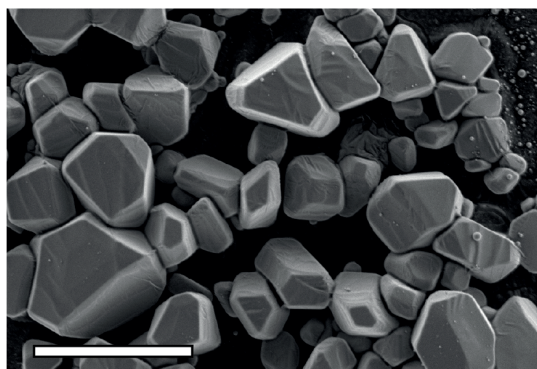


Figure 2.35 – SEM image of the metallic clusters in the anode area. Scale bar is 5  $\mu\text{m}$ .

---

### 2.3.7 Conclusion

I reported on the composition, morphology and electromechanical properties of biphasic (solid-liquid) films deposited by physical vapor deposition process on elastomer substrates.

I highlighted several mechanisms enabling high conductivity, low gauge factor and stretchability of the films to hundreds of percent and to a million cycles:

- pre-coating the substrate with a sputtered gold layer enabled the evaporated gallium to wet and diffuse in the gold layer to form a continuous coating.
- a fraction of the gallium alloyed with the gold while the excess remained liquid and accumulated into randomly distributed microscopic bulges. For a Ga/Au atomic ratio of 13, 97% of the film area remained under 5  $\mu\text{m}$  in thickness while the bulges could reach up to 20  $\mu\text{m}$  in height and 100  $\mu\text{m}$  in diameter.
- for a Ga/Au atomic ratio larger than 6 the solid alloy layer cracked while liquid gallium could flow between the cracks to maintain the continuity of the film. For a Ga/Au atomic ratio smaller than 6, the films fractured irreversibly, leading to degraded electrical properties.
- electro-mechanical properties were similar for a palladium pre-coating. By contrast, cracks appeared in the films prepared with platinum and iridium pre-coatings, leading to degraded electrical properties including a drift in the baseline resistance.

For a Ga/Au atomic ratio of 13, the films were characterized by a sheet resistance of 0.5  $\Omega/\text{sq}$ , a gauge factor of 1 up to 80% strain, a failure strain larger than 300% for uniaxial strain, and could sustain radial stretching resulting in a substrate surface area increase of 200%.

I also demonstrated that conductive tracks with critical dimensions down to 10  $\mu\text{m}$  could be patterned by lift-off process over large area, and maintain conductivity under repeated large (>50%) strains.

Finally, I showed that liquid electromigration occurred in the films exposed to prolonged DC currents, stressing the need to increase films uniformity in order to decrease the maximum current density and achieve reliable operation in a large range of applications.



## 2.4 Summary and outlook

Three technologies for stretchable metallization were presented in this chapter:

- micro-cracked Cr/Au thin films
- micro-plotted EGaIn wires
- biphasic gallium-based thin films

For each technique, Table 2.1 summarizes the properties reported in this chapter and in the literature when applicable.

	$\mu$ -cracked Cr/Au	$\mu$ -plotted EGaIn	Biphasic thin films
Thickness	<50 nm	$\approx 40 \mu\text{m}$ [134]	<1 $\mu\text{m}$
Sheet resistance ( $\Omega/\text{sq}$ )	20	$5 \times 10^{-3}$	0.5
Mean gauge factor	$\approx 4$	$\approx 2$	$\approx 1$
Maximum strain	0.5	>1 [134]	4
Hysteresis loop width (strain)	0.14	$< 1 \times 10^{-2}$	$< 1 \times 10^{-2}$
Fatigue (cycles)	$1 \times 10^6$ (@ 0.2 strain) [72, 80]	NC	$1 \times 10^6$ (@ 0.5 strain)
Critical dimension ( $\mu\text{m}$ )	50 [38]	40	10
Deposition and patterning	Parallel	Serial	Parallel
Electromigration	NC	NC	Yes

Table 2.1 – Comparison between the three stretchable metallization techniques on stretchable PDMS substrates reported in this chapter. NC: Not Characterized.

Micro-cracked Cr/Au films patterns on PDMS gather the required properties to be used as thin strain gauges up to maximum 50% of strain: they are sub-micrometer thin, have a large gauge factor (4) and high sheet resistance (20  $\Omega/\text{sq}$ ), resulting in large signal-to-noise ratio for strain sensing. A limitation is the large hysteresis loop width.

Micro-plotted EGaIn wires make stable, strain insensitive stretchable interconnects thanks to their very low sheet resistance (<5 m $\Omega/\text{sq}$ ) and finite gauge factor (GF=2). However, they are relatively thick (>40  $\mu\text{m}$ ) and can only be produced in a serial manner.

---

Finally, biphasic (solid-liquid) gallium-based thin films are versatile since they offer a low sheet resistance ( $0.5 \Omega/\text{sq}$ ), a thickness lower than  $1 \mu\text{m}$  on average, and a batch deposition and patterning method down to  $10 \mu\text{m}$  critical dimensions. Figure 2.36 illustrates their exceptional electromechanical performance compared to the state of the art for micro-patternable stretchable conductors: the ability to reach micro-metric critical dimension and less than double in resistance at 50% strain is unmatched to my knowledge. In addition, they are produced using standard industrial machines, a major asset for translation to large area and high throughput production. Yet, the conductive biphasic tracks may fail due to electromigration generated by prolonged direct current.

Many electro-mechanical characteristics must be taken into account to benchmark a stretchable conductor. For a given set of specifications - including electromechanical performance, critical dimensions, and cost - the stretchable electronic system designer should evaluate the different technologies at hand and choose the conductive material that offers the most appropriate trade-off for the target application.

The next chapter presents application of the three stretchable metallization technologies to fabricate hand-worn strain sensors. I demonstrate that the combination of micro-cracked gold thin films enables highly sensitive and localized strain sensing. I then utilize the superior electro-mechanical and patterning properties of biphasic gallium-based films to assemble even thinner, more robust sensing devices that can sustain the whole finger range of motion.

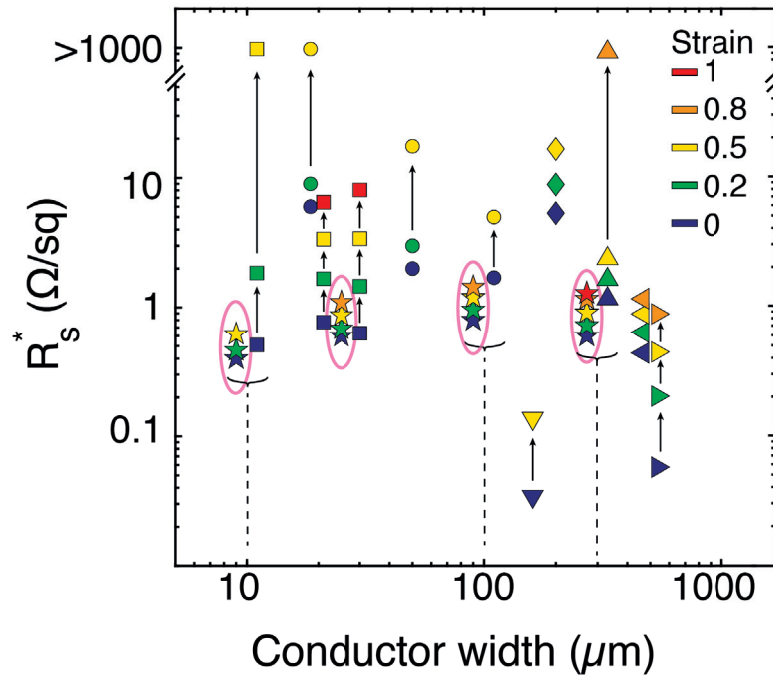


Figure 2.36 – Overview of published results on thin, intrinsically stretchable conductors patterned over large area ( $>50 \text{ cm}^2$ ) with line widths  $\leq 500 \mu\text{m}$  ( $\star$  Ga-based biphasic thin films [125],  $\blacksquare$  AgNW composite [75],  $\bullet$  AgNW composite [157],  $\blacktriangledown$  AgNW composite [56],  $\blacklozenge$  Au micro-cracked thin films [158],  $\blacktriangle$  Au nano-sheets [159],  $\blacktriangleleft$  Ag micro-flakes [74],  $\blacktriangleright$  AgNW composite [160]). The "as-designed" sheet resistance is calculated as  $R_s^* = R \frac{w_0}{L_0}$  where R is the resistance of the conductor at the strain considered and  $w_0$  and  $L_0$  are the width and length of the conductor at zero strain. Pink circles highlight biphasic thin films reported in section 2.3. Adapted from [75].

---

## 2.5 Contributions

For the work presented in section 2.1, I designed the experiments and Laurent Dejace (LD) and myself performed them as part of his master thesis under my supervision. LD also acquired the SEM images. I analyzed the data and wrote the paper together with Prof Lacour.

For the work presented in section 2.2, I designed the experiments and developed the micro-plotting process. Joan Teixidor fabricated the samples and performed the experiments for electrical and mechanical characterization as part of his semester project under my supervision. I analyzed the data and wrote the paper together with Prof Lacour.

For the work presented in section 2.3 apart from section 2.3.6 on electromigration, Arthur Hirsch (AH) and I initially conceived the study. AH performed the electro-mechanical characterization for gold underlayer, including long-term cycling. I acquired the electro-mechanical data for all the other underlayers and for the PET substrate. I acquired the SEM images and the EDS mapping data. I acquired and analyzed the XRD data with Séverine de Mulatier (SdM) as part of her master thesis under my supervision. SdM also acquired the AFM data. I performed the optical profilometry experiments and data analysis. I developed the lift-off patterning process and performed corresponding electro-mechanical characterization experiments. Dr Aaron P. Gerratt (APG) build the set-up and performed the radial stretching experiment. AH, APG, Prof Lacour and I further analyzed the results and wrote the paper.

For the work on electromigration presented in section 2.3.6, I designed the study and performed the experiments. I analyzed the data and wrote the paper manuscript together with Prof Lacour.

## 3 Skin-like strain sensors from stretchable conductors

In this chapter, the three stretchable conductor technologies presented in chapter 2 - micro-cracked gold thin films, micro-plotted EGaIn wires and biphasic thin metal films - are applied to construct soft, skin-like strain sensors. Section 3.1 describes a smart glove equipped with a strain sensing strip to encode the joints rotation of a humanoid robotic hand. Then I adapt the precedent design for a human hand and demonstrate its use in combination with soft tactile pressure sensors for grasp encoding in section 3.2. In section 3.3, I describe epidermal strain sensors based on biphasic thin films. Compared to the first two solutions, they enable a larger range of motion thanks to an increased robustness and a thickness reduced by one order of magnitude. The previous three sensing systems are limited to uniaxial sensing. In the last section 3.4, strain gauge rosettes made from micro-cracked Cr/Au to determine direction and magnitude of multi-axial strains are demonstrated.

This chapter is adapted from the following publications:

- A) H. O. Michaud, J. Teixidor, and S. P. Lacour. Soft flexion sensors integrating stretchable metal conductors on a silicone substrate for smart glove applications. In *2015 28th IEEE International Conference on Micro Electro Mechanical Systems (MEMS)*, pages 760–763, 2015.
- B) A. P. Gerratt, H. O. Michaud, and S. P. Lacour. Elastomeric Electronic Skin for Prosthetic Tactile Sensation. *Advanced Functional Materials*, 25(15):2287–2295, 2015.
- C) H. O. Michaud, L. Dejace, S. de Mulatier, and S. P. Lacour. Design and Functional Evaluation of an Epidermal Strain Sensing System for Hand Tracking. In *2016 IEEE/RSJ International Conference on Intelligent Robots and Systems (IROS)*, pages 3186–3191, 2016.
- D) H. O. Michaud, J. Teixidor, and S. P. Lacour. Soft metal constructs for large strain sensor membrane. *Smart Materials and Structures*, 24(3):35020, 2015.

---

## 3.1 Liquid metal wires and microcracked gold thin films for robotic hand motion encoding

### 3.1.1 Motivation

Robotic systems can be divided into two groups:

- *fully actuated* systems where there is at least one actuator per degree of freedom. The state or position of a fully actuated system can always be set or controlled to arbitrary position in the configuration space.
- *under actuated* systems where the state of the system cannot always be set or controlled to arbitrary position. For example, this is the case if there are less actuators than degrees of freedom. The state of such systems typically results from interactions with the environment.

A number of under actuated biomimetic robotic hands have been proposed recently [164–166]. Compared to fully actuated hands, the design is greatly simplified, resulting in lower cost, decreased weight, increased robustness and simpler control strategy. However, the lack of sensors makes it difficult to determine the system configuration and classify, for example, if a grasp attempt was successful or not. Implementing skin-like sensor to cover the hands and encode the position of each joint could enable precise position monitoring while maintaining the simplified design and actuation principles.

I proposed a skin-like sensing device to encode the physical position of biomimetic robotic fingers.

### 3.1.2 Design and fabrication of the sensors

#### Design

As illustrated in Figure 3.1, I assembled three flexion sensors made from microcracked gold films interconnected with micro-plotted liquid metal wires into a thin (<0.5 mm) and soft silicone membrane. The system was designed to fit on a humanoid robotic hand and monitor its three joints angular positions. The iCub robot was chosen as the test platform since its hand mimics the kinematic of the human fingers and is embedded with its own commercial rotation sensors [167]. In this implementation, the sensors were integrated in an elastomer membrane placed on a textile glove in tight contact with the dorsal side of the finger.

Let's consider an articulated finger with three cylindrical joints (metacarpophalangeal MCP, proximal interphalangeal PIP, and distal interphalangeal DIP) of radius  $r$  and rigid phalanxes.

### 3.1. Liquid metal wires and microcracked gold thin films for robotic hand motion encoding

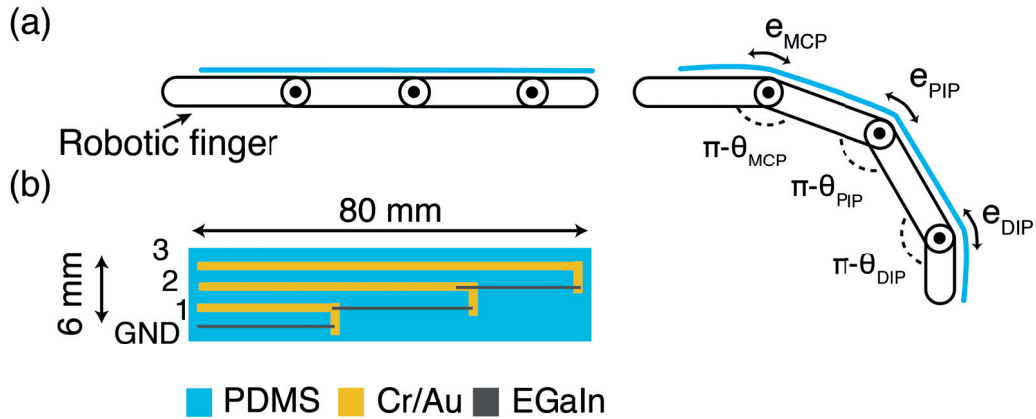


Figure 3.1 – Sensing principle and design of the stretchable flexion sensing strip with soft interconnects for humanoid fingers. a) The sensing strip was mounted on the surface of the finger to transduce the strain  $e$  that occurred when the finger was bent. b) Design of the sensing strip.

When a joint of the finger rotates by an angle  $\theta$ , the length of the dorsal part the finger increases by  $\theta r$ . It results in a tensile strain  $e$  across the surface of the soft membrane located on top of the joint (Figure 3.1a). In order to convert this mechanical stimulus, I chose to form strain gauges from patterns of the stretchable gold thin films. Three gold-film strain gauges with graded lengths aligned with the middle of the phalanxes of the robotic finger were interconnected. The staggered EGaIn interconnect design was laid down because of a limitation from the printing set-up, which restricted the maximum length of a printed wire to 35 mm.

The liquid metal interconnects provided a fully elastic wire-sensor interface thereby avoiding interfacing mechanically soft sensors with hard wiring. In particular, it prevented mechanical stress concentration at the soft-hard junctions and failure of the sensory skin.

#### Readout circuit

Figure 3.2 presents the equivalent readout electrical circuit of the soft sensing system. The resistance of each sensor was recorded through a voltage divider connected to the analog inputs of an Arduino Micro board (Arduino/Adafruit, 15 Hz sampling frequency). The voltage reference was set at 1.24 V (LM 385, Texas Instruments). As shown in section 2.2 page 26, soft liquid metal micro-wires embedded in silicone have a small resistance at rest (less than 1  $\Omega$  for centimeter-long wires) and their resistance increases by less than 150% for strains up to 50%. Hence, for each gauge  $j$ , its resistance  $R_j$  was much larger than the sum of the resistances  $R_{int,j}$  of the interconnects:  $R_j \gg \sum R_{int,k}$  at rest. When the finger was flexed,  $\Delta R_j \gg \sum \Delta R_{int,k}$  so the sensors could be addressed independently through the interconnection network.

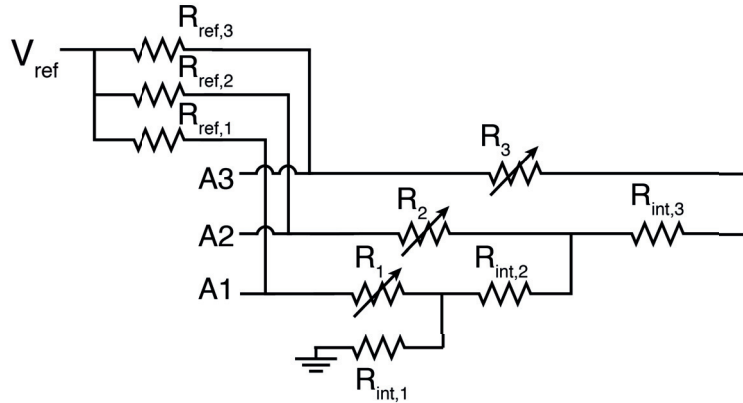


Figure 3.2 – Equivalent electrical circuit of the soft integrated flexion sensing strip for humanoid fingers. The resistance of each sensing gauges  $R_j$  is probed through a voltage divider bridge with reference voltage  $V_{ref}$  and connected to ground via the interconnects  $R_{int,j}$ .  $R_j \gg \sum R_{int,k}$  at rest and  $\Delta R_j \gg \sum \Delta R_{int,k}$  when a strain is applied by bending the finger.

## Fabrication

The fabrication process is detailed in the Appendix sections A.1.1 and A.1.2 page 117. To quickly summarize it, 5/25 nm Cr/Au thin film were evaporated on a PDMS through a stencil mask. Then EGaIn wires were micro-plotted to interconnect the Cr/Au structures, solid wires were connected and secured using silicone sealant, and PDMS encapsulation was spin-coated. The final thickness of the strips was below 500  $\mu\text{m}$ .

### 3.1.3 Results and discussion

#### Single sensor characterization

After microfabrication, the strip was attached to a textile glove using EcoFlex (Smooth-On) as a curable adhesive. When the robot was wearing the sensorized glove, it could rotate normally all finger's joints and open and close completely its hand (Figure 3.3). The Arduino board was addressed from a PC through the serial communication bus. I assessed the repeatability and linearity of the sensors by recording the relative increase in resistance of sensor 1 when the MCP joint was incrementally closed multiple times (Figure 3.4). Small standard deviations and a high  $R^2$  value indicated good linearity of the sensor.

#### Computation of the joints angle

I made the following assumptions in order to compute the three joints' angle from the output of the sensors:

- The rotation of each joint resulted in a linear increase of the electrical resistance of each



### 3.1. Liquid metal wires and microcracked gold thin films for robotic hand motion encoding

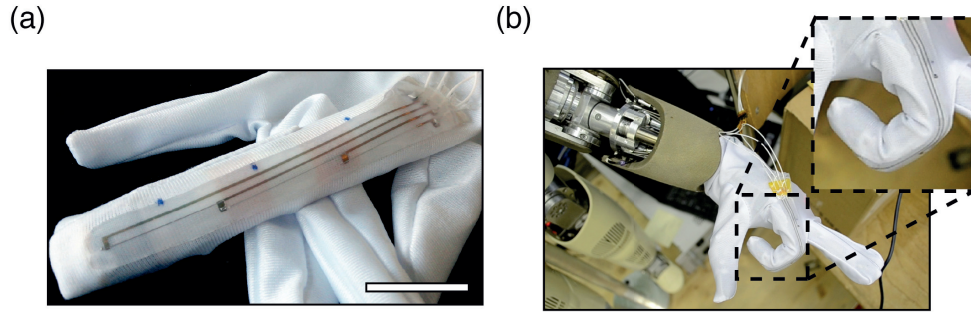


Figure 3.3 – a) Soft flexion sensing trip after mounting on a textile glove. Scale bar is 20 mm. b) Glove worn by the iCub robot with its finger fully flexed.

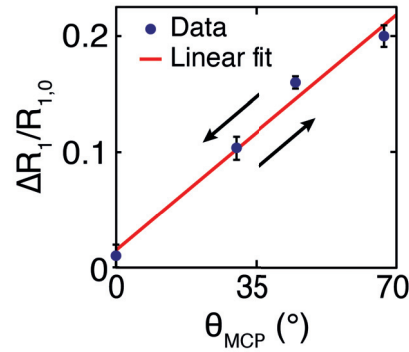


Figure 3.4 – Response of sensor 1 to flexion of the MCP joint. 12 flexion cycles from 0° to 67° are represented. Error bars represent 99% confidence interval. Solid line represents linear interpolation ( $R^2=0.98$ ).

strain gauge.

- This increase in resistance was independent from the position or rotation of the other joints.

Hence, the relative increase in resistance of each sensor was a linear combination of the three joints' angles, with fixed coefficients. I defined the vectors  $\boldsymbol{\theta} = [\theta_{MCP}; \theta_{PIP}; \theta_{DIP}]$  and  $\mathbf{R} = [\frac{\Delta R_1}{R_{1,0}}; \frac{\Delta R_2}{R_{2,0}}; \frac{\Delta R_3}{R_{3,0}}]$  and could therefore define:

$$\mathbf{R} = \mathbf{J}\boldsymbol{\theta} \quad (3.1)$$

where  $\mathbf{J} = \mathbf{K}^{-1}$  is a  $3 \times 3$  matrix.

The calibration matrix  $\mathbf{K}$  ( $\boldsymbol{\theta} = \mathbf{K}\mathbf{R}$ ) was determined using the following calibration scheme. The outputs of the sensors were recorded for six different known positions of the finger and arranged in an  $18 \times 9$  matrix  $\mathbf{R}_{cal}$ . The angles of the three joints for the six known positions were arranged in an eighteen elements vector  $\boldsymbol{\theta}_{cal}$ . The nine elements vector containing the

---

coefficients of matrix  $K$ ,  $C_K$ , was computed using the least square method:

$$C_k = (R_{cal}^T R_{cal})^{-1} R_{cal}^T \theta_{cal} \quad (3.2)$$

This routine was implemented in Matlab (MathWorks).

### **Acquisition of the position of the robotic hand**

After determination of the calibration matrix  $K$ , a Matlab script converted the sensors' outputs into joint angles and displayed the finger position. Figure 3.5 presents the sensors outputs, the computed angles and the reconstructed finger position for repeated complete closings of the robot's hand. The MCP joint was first rotated then PIP and DIP joints were completely closed at the same time. The joints were actuated in the inverse order for opening.

Data showed that the sensors were stable, quickly adapted to finger motion with good repeatability, and did not overshoot (Figure 3.5). I also observed a systematic large overestimation of  $\theta_{PIP}$  ( $\approx 130^\circ$  vs  $90^\circ$  reading from embedded reference sensor) and large underestimation of  $\theta_{DIP}$  ( $\approx 75^\circ$  vs  $90^\circ$  reading from embedded reference sensor) when the finger was completely closed. This might come from non-linearity or global strain (not only in the vicinity of the joints) occurring in the skin during finger bending. These phenomena were not taken into account in the calibration scheme.

With longer interconnects, the accuracy of the sensors could have been improved by patterning a single strain sensing area per joint, thus mechanically reducing crosstalk between sensors. For example, as sensor 1 was covering the MCP joint only, it was mainly sensitive to the closing of the MCP joint and not to the rotation of the other two joints (Figure 3.5a). However, the calibration scheme is general and could be used for compensating the cross-talk in an alternative sensor's layout.

### 3.1. Liquid metal wires and microcracked gold thin films for robotic hand motion encoding

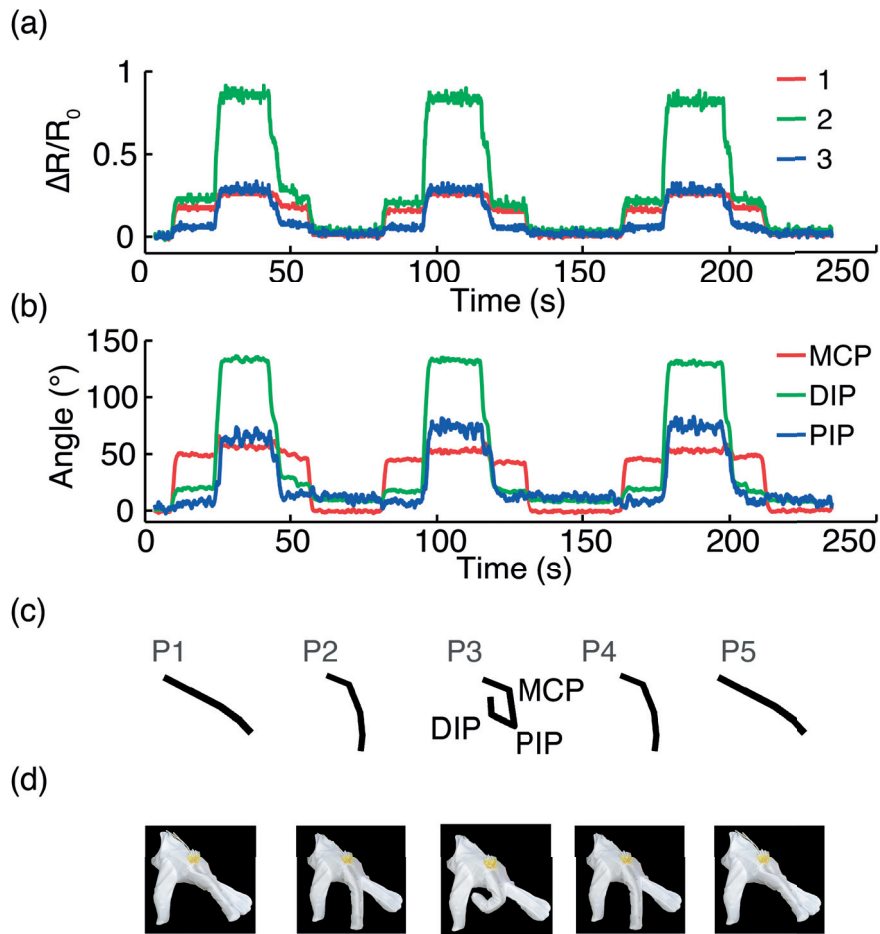


Figure 3.5 – Acquisition of robotic hand position with the soft sensor strip. a) Sensor output as a function of time for three complete index closing and opening. b) Computed joints angles. c) Reconstructed index profile for positions P1 to P5. d) Actual hand profile for positions P1 to P5.

---

### **3.1.4 Conclusion**

I reported on the fabrication and characterization of stretchable, skin-like flexion sensors designed to encode the position of a biomimetic robotic finger's joints. The skin system was mounted on the iCub humanoid hand to assess the sensors' linearity, repeatability and dynamic behavior. I also proposed a calibration algorithm that overcame design limitations and enabled reconstruction of the finger posture in real time. Modification of the sensor's design could enhance the accuracy of the sensors.

In the next section, the proposed design is adapted to encode the movements of human fingers.

## **3.2 Liquid metal wires and microcracked gold thin films for motion encoding on a glove**

### **3.2.1 Motivation**

I adapted the design presented in section 3.1 to allow for tracking of a human hand and coupling with soft tactile pressure sensors. This was important not only to extract richer grasping information by adding two sensing modalities, but also to increase the accuracy of the tactile sensors in real-life scenarios. Indeed, stretchable tactile pressure sensors often display a large cross-sensitivity to strain and noise received from the human body [122, 123]. The solution proposed here combined the response of soft strain and pressure sensors to extract accurate finger bending and tactile information with a hand-wearable device.

### **3.2.2 Design and fabrication of the sensors**

#### **Design**

The sensors displayed Figure 3.6 were designed to encode the flexion and extension of two joints of the user's index finger: the metacarpophalangeal (MCP) joint and proximal-interphalangeal (PIP) joint. Two strain gauges were prepared with highly strain sensitive stretchable gold thin film interconnected with printed elastic liquid metal wires.

#### **Fabrication**

The fabrication process is detailed in the Appendix sections A.1.1 and A.1.2 page 117. To summarize it briefly, Cr/Au (5/40 nm) bilayers were thermally evaporated onto 125  $\mu\text{m}$  thick PDMS. Liquid metal wires were then plotted on the PDMS membrane. The elastic wires were next connected to Teflon coated silver wires for interfacing with the readout electronics. Then the sensors on PDMS were encapsulated with a thin layer of PDMS. The total thickness of the encapsulated sensors was below 500  $\mu\text{m}$ . Soft sensing strips were mounted onto a textile glove with a thin layer of silicone (Ecoflex 00-10, Smooth-On), which was cured at 50  $^{\circ}\text{C}$  in an oven.

### **3.2.3 Characterization**

#### **Sensor response to finger flexion**

Once mounted on a finger, the glove user was asked to flex and extend his MCP joint and his PIP joint sequentially in order to evaluate the response of each sensors. The flexion-sensing skin reliably discriminated between the PIP and MCP joint movement (Figure 3.7). The joints angular positions were measured during an arbitrary finger movement. Both sensors' resistance increased linearly as a function of joint angle ( $R^2 > 0.94$  for both sensors). The average cross sensitivity of the PIP to the MCP joint flexion was less than 6% in the considered angular

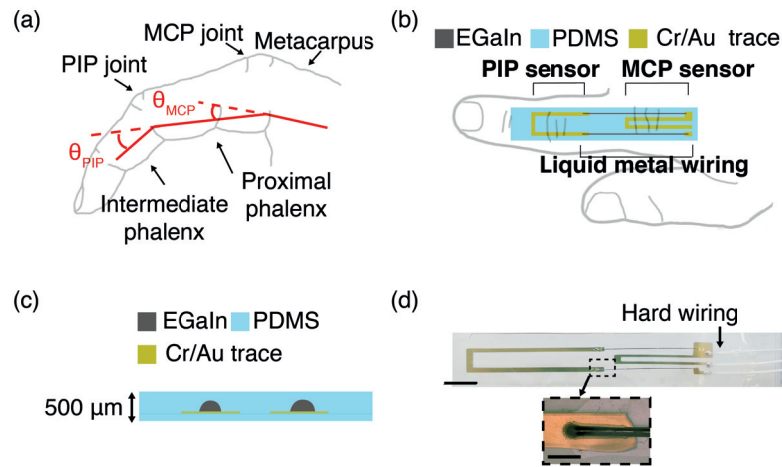


Figure 3.6 – Soft resistive sensor for transducing the relative motion of the first two phalanges of a human finger. a) Schematic representation of the finger featuring the relative angles of the metacarpophalangeal (MCP) and proximal interphalangeal (PIP) joints. b) Design of soft integrated goniometric sensors. c) Schematic of the cross-section. d) Image showing the fabricated strain and bending sensor. Scale bar on full device is 5 mm. Scale bar on close-up of Au and EGaIn intersection is 1 mm.

motion range, and less than 10% vice versa. The range of motion of the user was intentionally limited when using the sensorized glove since the strain sensors could not sustain the strain induced by complete flexing of the joints.

### 3.2. Liquid metal wires and microcracked gold thin films for motion encoding on a glove

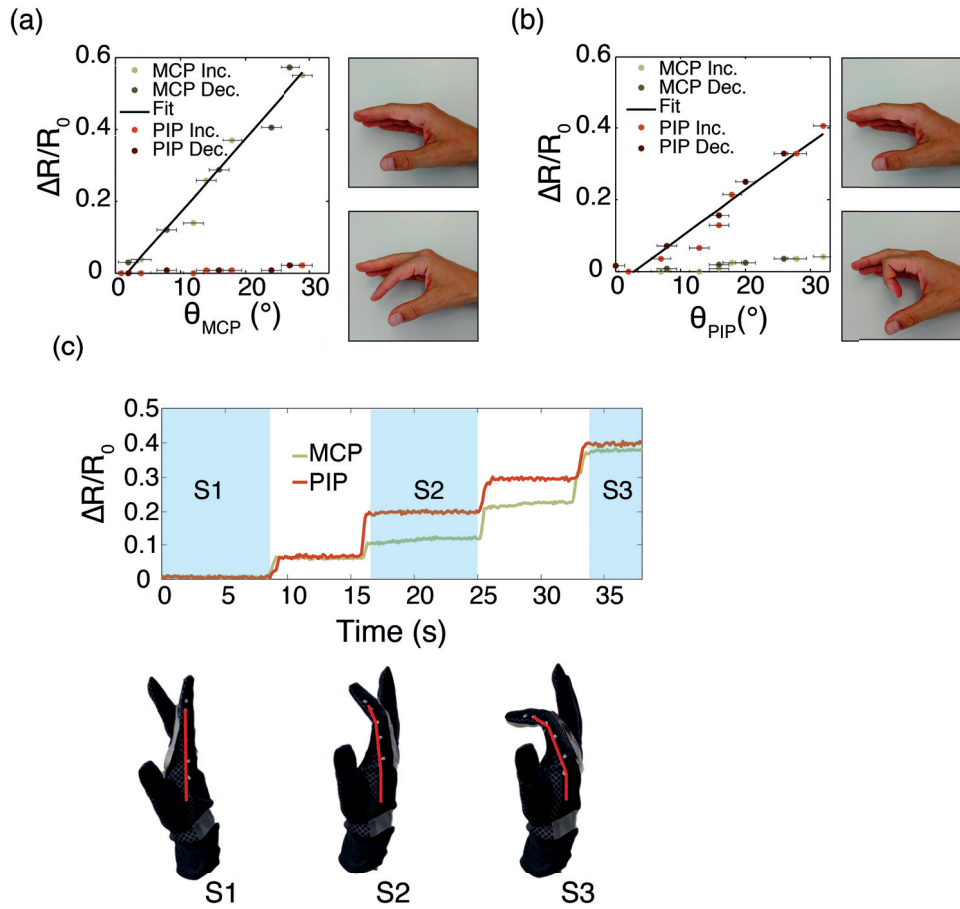


Figure 3.7 – a) Response of the MCP and PIP resistive sensors to a flexion of the MCP joint only. Visual markers on the two joints, on the middle of each phalanx and on the metacarpus were used to quantify the finger’s position. Light and dark shades represent increasing (inc.) and decreasing (dec.) angles, respectively. The solid line represents a linear fit of the MCP sensor’s response ( $R^2 = 0.97$ ). b) Response of the MCP and PIP resistive sensors to a flexion of the PIP joint only. Light and shades represent increasing and decreasing angles, respectively. The solid line represents a linear fit of the PIP sensor’s response ( $R^2 = 0.94$ ). c) Time response of both bending sensors for arbitrary finger motion when the hand is closed step by step. The reconstructed finger profile (in red) is compared with pictures taken during steps S1, S2 and S3.

---

### Sensor response to temperature

The sensors were placed in an oven (B180, Nabertherm) while the temperature was monitored with a bandgap temperature sensor (MCP9808, Microchip).

The change in resistance of a gold conductor subject to temperature change can be calculated as  $\frac{\Delta R}{R_0} = \alpha(T - T_0)$  where  $R_0$  is the resistance at a reference temperature,  $T_0$  is the reference temperature,  $\alpha$  is the thermal coefficient of resistance (TCR) and  $T$  is the final temperature. TCR of bulk gold is  $3.72 \times 10^{-3} \text{ K}^{-1}$  and TCR of gold thin film has been measured to be lower  $1.5 \times 10^{-3} \text{ K}^{-1}$  for 17 nm films and  $1.7 \times 10^{-3} \text{ K}^{-1}$  for 110 nm films [168, 169]. A temperature increase of  $30 \text{ }^\circ\text{C}$  would result in a relative increase in resistance of 0.05 to 0.1, significantly less than the measured increase of 0.7 in relative resistance of the strain sensors for an increase from  $22 \text{ }^\circ\text{C}$  to  $52 \text{ }^\circ\text{C}$ . The additional increase in resistance of the sensors may be explained by the thermal expansion of the silicone substrate.

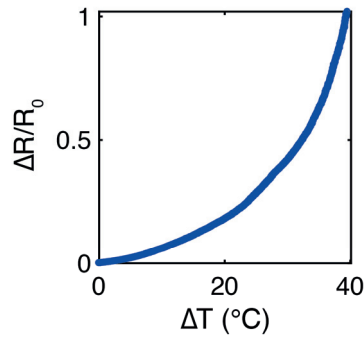


Figure 3.8 – Relative change in resistance of a strain sensor as a function of temperature increase from room temperature.

### 3.2.4 Coupling with soft-pressure sensor for grasp encoding

As displayed in Figure 3.9a, a glove featuring stretchable flexion/extension resistive sensors on the dorsal side and soft capacitive tactile sensors on the palm side of the index finger was assembled. More details on the capacitive tactile sensors fabrication and performance are available in [162]. Flexion of the finger was also detected with the capacitive sensors: when the finger was closed, the recorded capacitance change was similar to a 50 kPa tactile compression, a significant error if left uncompensated.

After a calibration step, live bending compensation was allowed on each tactile node. During movement of the finger, the response of the capacitive sensors was corrected as:

$$\Delta C_{comp} = \Delta C - \Delta C(\Delta R_{MCP}, \Delta R_{PIP}) \quad (3.3)$$



### 3.2. Liquid metal wires and microcracked gold thin films for motion encoding on a glove

where  $\Delta C$  is the raw data, and  $\Delta C(\Delta R_{MCP}, \Delta R_{PIP})$  is the compensating capacitive value defined at the selected finger MCP and PIP joint position.  $\Delta C(\Delta R_{MCP}, \Delta R_{PIP})$  is determined for each tactile sensor node by asking the user to flex the MCP joint only, the PIP joint only, and finally both joints, and performing a third degree polynomial fit. Figure 3.9b shows that the compensation scheme efficiently diminished tactile sensors sensitivity to bending, with a peak response divided by more than three (0.2 pF to 0.06 pF).

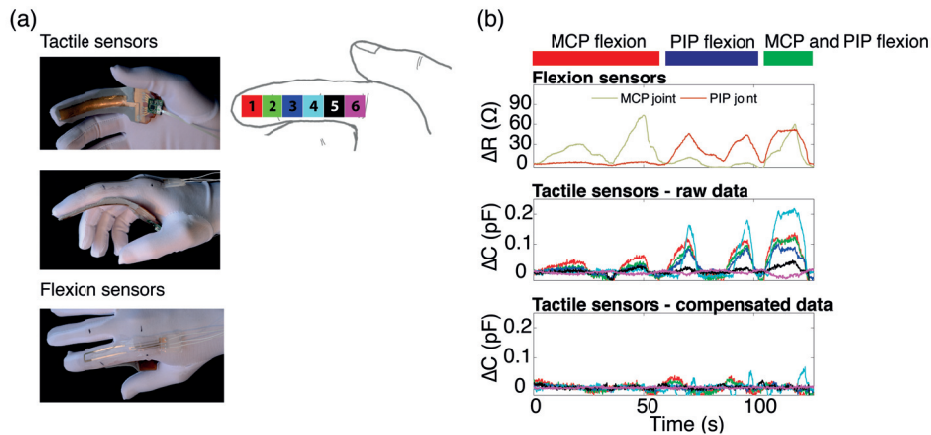


Figure 3.9 – Coupling soft strain sensors with soft tactile force sensors on a glove. a) Images of the pressure sensors on the palmar side of the hand and flexion sensors on the dorsal side of the hand with schematic representations of the sensor locations on the finger. b) During finger articulation, the strain–pressure cross-sensitivity of the tactile sensors was compensated with the strain sensor response. The three plots show the flexion sensor data, the raw data from the tactile sensors, and the compensated response of the tactile sensors. Data from all six of the capacitive sensors are shown, with the plotted colors representing the corresponding location in the schematic of the finger.

---

The possibility of distinguishing soft from hard objects with the smart tactile glove was then investigated. During this experiment, objects with distinct compliance were held between the index and thumb, and squeezed three times. The soft and hard objects were both 6.5 cm diameter cylinders prepared with compressible polyurethane foam and rigid plastic, respectively. The combined readouts of the flexion and capacitive sensors differentiated objects stiffness. When squeezing the soft cylinder, pressure and flexion sensor responses increased simultaneously as the soft object was compressed. Conversely, the flexion sensor readout remained constant once the hard object was grasped, and only the capacitive sensors detected the three additional squeezes. Holding the hard object at the base of the fingers, as opposed to the fingertip (Figure 3.10a), lead to distinct absolute sensor readouts, and highlighted the necessity for full-finger coverage in order to gain a complete comprehension of the grasp dynamics.

Finally, the smart tactile glove was evaluated in a more complex grasping task using human-in-the-loop visual feedback (Figure 3.10b). The glove wearer was asked to grasp an object while watching a color on a display. The color represented the tactile information from no touch (dark blue) to high compressing touch (red) with graded intermediate levels. The user was instructed to pick up the object and then adjust his grasp to a pre-set, arbitrarily selected pressure (matching the cyan color on the scale). Visual feedback, in the form of a color, of the instantaneous response of the tactile sensors was used to adjust and reach the target contact pressure. Two successive grasps and releases are illustrated Figure 3.10b. When the object was grabbed, the applied pressure overshoot then decreased and was held at the desired level based on the visual, color feedback. This type of closed-loop task is critical in robotic and prosthetic applications where robotic control, sensing, actuation, and neural stimulation should be precisely coordinated [120].

### 3.2. Liquid metal wires and microcracked gold thin films for motion encoding on a glove

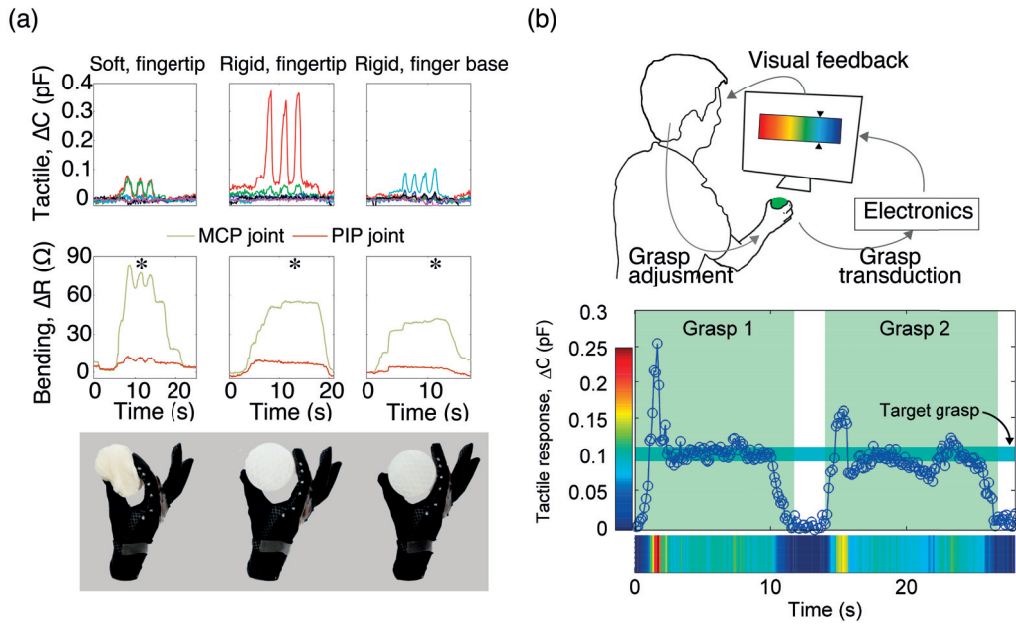


Figure 3.10 – Grasp transduction using a glove equipped with soft strain sensors and soft tactile sensors. a) Grasps of a soft, compressible object and a rigid, incompressible object of the same diameter. The \* symbols denote the time when the images of the grasps were taken. b) Tactile response during a grasp and manipulation task demonstrating the wearer was able to adjust the grasp strength to the target pressure during two trials.

---

### 3.2.5 Conclusion

I have demonstrated a multifunctional, wearable electronic skin, optimized for hand tactile information encoding. Elastic metallization and silicone elastomers were processed with standard fabrication techniques to form a highly compliant and large-area sensory skin conveying live pressure and proprioceptive-like information.

The integration of bending and pressure sensors on the dorsal and palmar side of the hand enabled:

- combined detection of tactile and bending inputs.
- decoupling of multi-modal stimulation of the soft tactile sensors, with a peak response to bending divided by three.
- discrimination between soft and hard object.
- fine grasp force control by the user.

In the next chapter, I use biphasic thin metal films to enable assemble thinner wearable strain sensors compatible with a larger range of motion.

## 3.3 Epidermal strain sensors from biphasic thin films

### 3.3.1 Motivation

I applied the stretchable gallium-based thin film deposition and micropatterning process presented in section 2.3 page 32 to construct skin-worn strain sensors. Compared to the glove-based solutions presented in the two previous sections, the objective was to:

- assemble thinner and more robust sensors to achieve larger range of motion (ROM) and minimal limitation of motion.
- evaluate the response of the sensors subjected to parasitic stimuli including transverse strain, normal pressure and thermal loading.
- quantify the tracking performance of the sensors with a reference system in the considered ROM and for a large range of grasping tasks.

### 3.3.2 Design and fabrication of the sensors

#### Design

Two sets of sensors were designed and fabricated. The first one served to characterize the response of a single strain gauge to uniaxial longitudinal strain, uniaxial transverse strain and normal pressure. The second was designed to cover the articulations of the human finger and measure the finger's motion over its full range of flexion and extension.

**Sensors for characterization under uniaxial strain** The size of the sensors was selected in order to fit in the customized linear stretcher described section 2.1.2 page 21. The sensors featured large terminal tracks (800  $\mu\text{m}$  width) and thin meander patterns (sixteen 100  $\mu\text{m}$  wide parallel tracks, as shown Figure 3.11a).

**On-finger flexion and extension sensors** Long sensing strips (80  $\times$  9.8  $\text{mm}^2$ ) hosted two flexion and extension sensors (Figure 3.11b). Each sensor consisted of two meander patterns (sixteen 100  $\mu\text{m}$  wide parallel tracks or twenty 50  $\mu\text{m}$  wide parallel tracks) interconnected to 800  $\mu\text{m}$  wide terminal tracks. The spacing (50  $\mu\text{m}$  center to center) and length (15 mm) of the gauges were chosen to cover most of the human finger sizes [104]. Assuming a constant sheet resistance, the meander patterns were at least 35 times more resistive than the terminal tracks for all sensor pairs designs. Hence, most of the sensed signal came from the meanders and the cross talk from the tracks was minimized. Two sensors covering the metacarpophalangeal (MCP) and proximal interphalangeal (PIP) joints were sufficient to reconstruct the whole finger movement since the movement of the distal interphalangeal joint (DIP) is strongly coupled to the PIP joint [170].

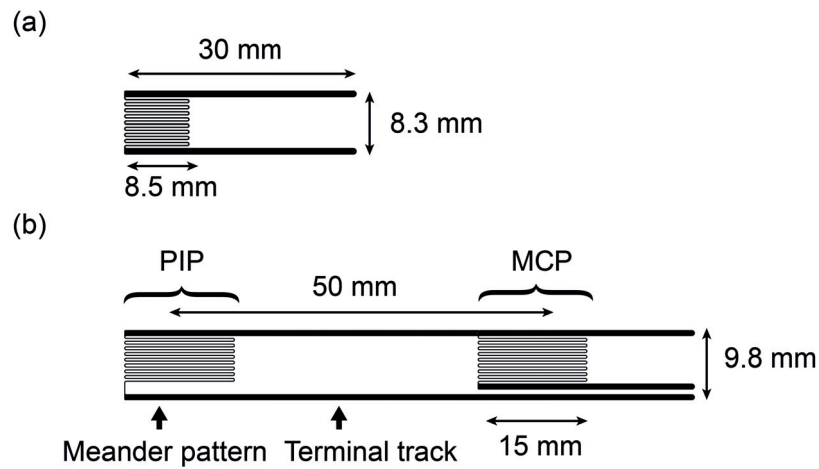


Figure 3.11 – a) Design of a single sensor for characterization and b) sensor pair for on-finger flexion and extension sensing. Meander patterns were composed of sixteen  $100\ \mu\text{m}$  wide parallel tracks for the single sensor and sixteen  $100\ \mu\text{m}$  or twenty  $50\ \mu\text{m}$  wide parallel tracks for the sensor pair for on-finger flexion sensing. Terminal tracks were  $800\ \mu\text{m}$  wide for both designs.

### Fabrication

The sensors were fabricated according to the process-flow details in Appendix section A.1.3 page 118. To summarize it briefly, a  $25\ \mu\text{m}$ -thick PDMS film was spin-coated and cured on a support silicon wafer. After this, photoresist was spin-coated, exposed and developed. Subsequently, a  $40\ \text{nm}$ -thick Au adhesion layer was sputtered and  $0.2\ \text{g}$  of Ga were thermally evaporated to form a solid-liquid biphasic film. The photoresist was removed in a stripping solution. Next, the metallized tracks were connected to stranded wires with eutectic gallium-indium and encapsulated with a silicone sealant (734, Dow Corning). The sensors were encapsulated by spin-coating a second  $25\ \mu\text{m}$ -thick PDMS layer. They were finally cut and manually peeled off the support wafer before usage. Figure 3.12 shows three sensor strips in use after fabrication and a schematic cross-section of the sensors.

### 3.3.3 Response to uni-axial strain, normal force, and temperature variation

#### Experimental set-up and instrumentation

For uniaxial strain characterization, I used the custom stretcher described in section 2.1.2 page 21. The sensors were held by  $40\ \text{mm}$  wide clamps.

For pressure response testing, a controlled normal force was applied on the sensors over an area of  $23 \times 14\ \text{mm}^2$  using an electromechanical Universal Test System (Criterion C.42, MTS) with a  $100\ \text{N}$  load cell.

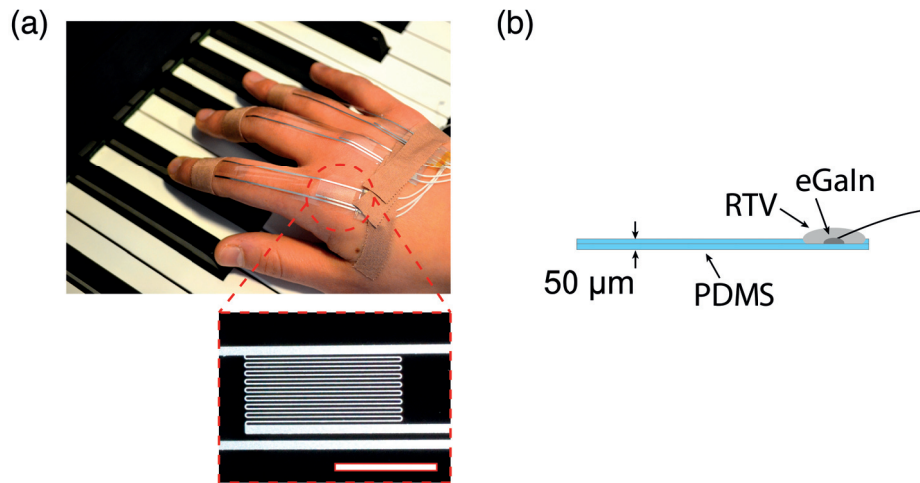


Figure 3.12 – a) Three pairs of sensing strain gauges placed on a hand performing a fine motor task. Scale bar of inset is 10 mm. b) Schematic cross-section of a sensor connected with external wiring.

For thermal response testing, the sensors were placed in a temperature controlled oven (UFE 500, Memmert), and the resistance of the sensor was monitored while the temperature was raised from room temperature to 100 °C.

#### Results and discussion

The gauge factor in the x-direction was 1.2 versus only 0.05 in the y-direction (Fig. 3.13a-b), therefore the strain gauges were 24 times more sensitive to strains in the designed sensing direction than in the transverse direction. This selective sensitivity is a key feature for strain gauges [131].

Sensitivity to normal pressure was less than  $0.2 \text{ MPa}^{-1}$  in the 0 kPa to 100 kPa pressure range (Figure 3.13c). The sensor's resistance increased linearly as a function of the temperature in the considered range ( $R^2 > 0.99$ ), with a sensitivity of  $1.7 \times 10^{-3} \text{ K}^{-1}$ .

The strain gauges behaved similarly to traditional strain gauges even at very large strains, and their performance was minimally influenced by transverse strains or normal pressure. Thermal drift should be compensated for if the application involves large temperature variations, by means of a Wheatstone bridge for instance.

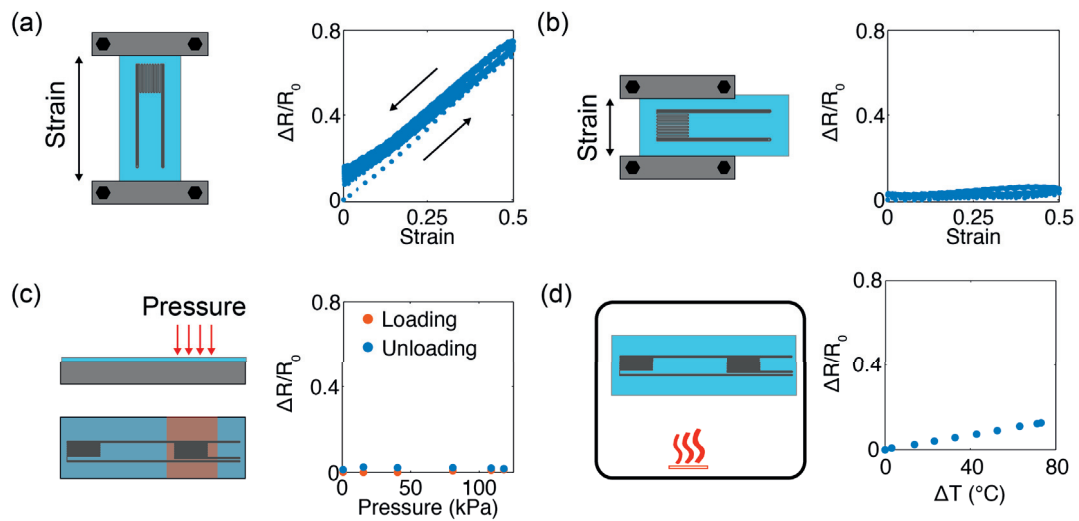


Figure 3.13 – Relative change in resistance of a characterization sensor as a function of (a) uniaxial longitudinal strain for 200 cycles to 50% strain, (b) uniaxial transverse strain for 20 cycles to 50% strain, (c) normal pressure, and (d) temperature increase from room temperature.

### 3.3.4 Benchmarking as finger tracking sensors

#### Experimental set-up

In this study, the MCP and PIP angles computed by the sensors were compared to the angles measured by a motion tracking system (Nexus, Vicon Motion Systems), consisting of eight Bonita cameras and one data acquisition device (Vicon Datastation ADC Patch Panel, Oxford Metrics). The system tracked markers with a precision of 0.5 mm in translation and  $0.5^{\circ}$  in rotation according to the manufacturer's specifications. Nine markers were positioned on the carpo-metacarpal (CMC), metacarpo-phalangeal (MCP), proximal-interphalangeal (PIP) and distal interphalangeal (DIP) joints and fingertip (FT) of the subject (Figure 3.14). The 3D spatial position of the markers was recorded at 100 Hz. Acquisition of signals from the flexion sensors and the tracking system were synchronized.

The sensors' resistances were recorded at 1 kHz with a 16 bit resolution via a voltage divider. A constant input voltage of 5 V (2400 SourceMeter, Keithley) was applied across each track on which two 1.5 k $\Omega$  reference resistors were mounted.

The sensing strip and the markers for the camera motion tracking were placed as depicted Figure 3.14. Placement of the markers enabled the projection of the finger angles in the sagittal plane of the hand [171]. The sagittal plane was defined as perpendicular to the plane containing the CMC2, MCP2 and MCP3 markers. The computation of the joint's angles from markers' positions is detailed in Appendix A.6 page 126.



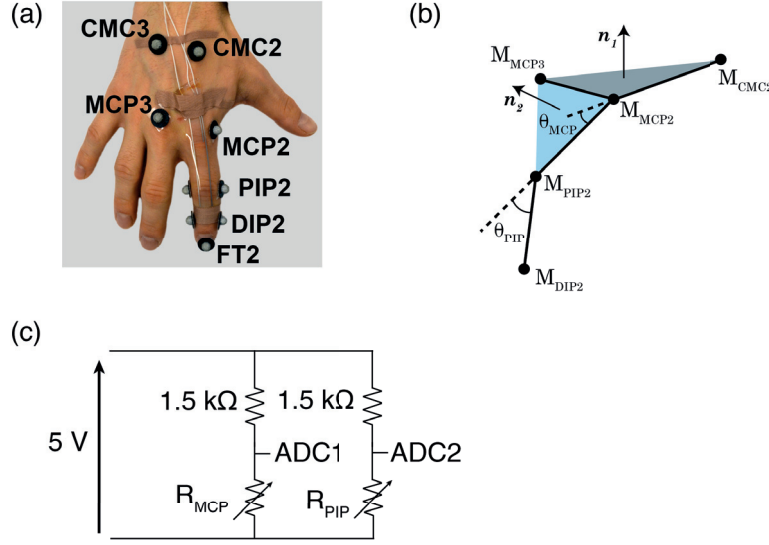


Figure 3.14 – Experimental set-up for joints angle recording and sensor readout. a) Position of the markers for video-tracking. b) Definition of the MCP and PIP angles, and the plane used to compute them. c) Readout circuit schematic.

### Calibration procedure

At the beginning of each data acquisition session, the subject was asked to sequentially flex and extend his/her MCP joint three times, then his/her PIP joints three times, then both joints three times. The considered range of motion (ROM) covered most of the average functional ROM for both joints (respectively 0° to 61° for MCP joint and 0° to 60° for the PIP joint) [172].

From the data of the calibration runs illustrated in Figure 3.7, the least squares method was applied to determine the coefficients of a second order polynomial regression model:

$$\theta = a_0 + a_1 \frac{\Delta R_{MCP}}{R_{0,MCP}} + a_2 \frac{\Delta R_{PIP}}{R_{0,PIP}} + a_{12} \frac{\Delta R_{MCP}}{R_{0,MCP}} \frac{\Delta R_{PIP}}{R_{0,PIP}} + a_{11} \left( \frac{\Delta R_{MCP}}{R_{0,MCP}} \right)^2 + a_{22} \left( \frac{\Delta R_{MCP}}{R_{0,MCP}} \right)^2 \quad (3.4)$$

The  $a_i$  coefficients were determined for each angle (MCP and PIP) and used to reconstruct the angles  $\theta_{MCP}$  and  $\theta_{PIP}$  from the resistances of the pair of sensors in every other run of the session.

Abduction and adduction of the index were minimally influencing the output signal (1.6% of

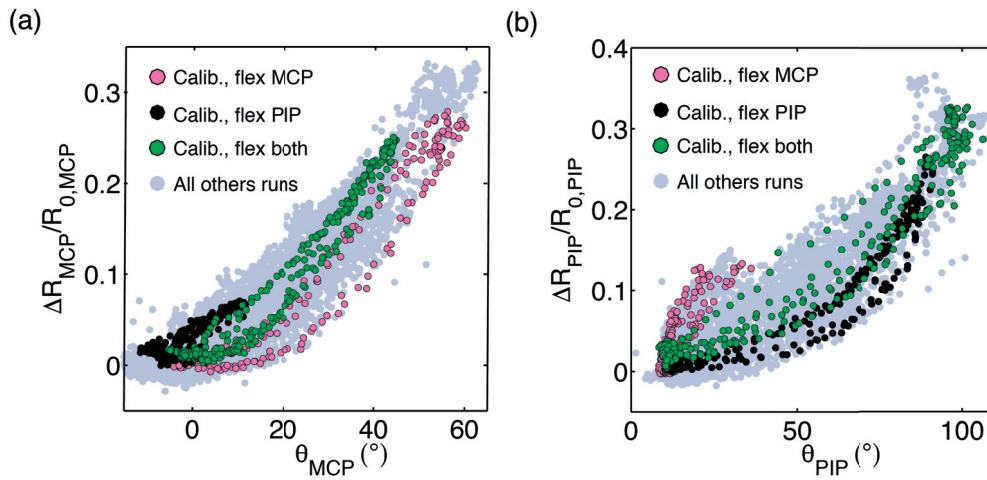


Figure 3.15 – Calibration of a pair of epidermal strain sensors. a) Relative change in resistance of the MCP sensor as a function of  $\theta_{MCP}$  for the nine calibration flexions and extensions of the third session. The blue points represent the data acquired during all the other runs of the session. b) Relative change in resistance of the PIP sensor as a function of  $\theta_{PIP}$  for the nine calibration flexions and extensions of the third session. The grey points represent the data acquired during all the other runs of the session. For clarity, only one in ten points were plotted.

relative resistance variation over a full ad-abduction cycle) of the MCP sensor, validating the choice of studying the flexion of the finger in the sagittal plane of the hand only.

### 3.3.5 Comparison with the video-tracking system during grasping tasks

#### Description of data acquisition sessions

In total, three data acquisition sessions were performed, using different sensor designs or attachment strategies. The first featured 100  $\mu\text{m}$  wide tracks in the meander patterns, and were glued directly to the finger using skin adhesive silicone (7-9700, Dow Corning). The second and third sessions were performed by attaching the strip to the finger with medical tape, as demonstrated in Figure 3.14. The width of the meander patterns was decreased to 50  $\mu\text{m}$  in the third session. The use of tape enabled quicker and easier adjustment and repositioning of the strips at the beginning of the session. The sensors could also be put slightly under tension in the resting position to prevent the apparition of a "dead-zone" in-which no signal variation occurred for low MCP or PIP angles.

The whole set of grasps performed during the different sessions consisted in moving the MCP joint only, moving the PIP joint only, moving both joints, performing a power grip grasp on cylindrical objects with diameters of 65 mm, 53 mm, 39 mm and 28 mm, performing a tip

### 3.3. Epidermal strain sensors from biphasic thin films

Table 3.1 – Type and number of tasks for all data acquisition sessions.

	100 μm, glue	100 μm, tape	50 μm, tape
Flex. MCP	3	6	6
Flex. PIP	3	6	6
Flex. both	3	6	6
Power 65 mm	6	6	9
Power 53 mm	6	9	6
Power 39 mm	6	6	9
Power 28 mm	0	9	6
Tip pinch	6	9	6
Writing tripod	3	9	9
Pliers	0	6	9
Catch bottle	0	0	6
Total	36	72	78

pinch grasp, performing a writing tripod grasp, manipulating pliers, and catching a falling bottle of water. Table 3.1 details the number and types of tasks for each session.

During the first session, the glued sensors sometimes detached from the user's finger, making it impossible to exploit the data for a number of tasks. Differences in repetitions between second and third sessions came from unusable data from the video tracking system due to missing markers trajectories, except for the bottle catching task that was added during the third session.

#### Sensor response to finger flexion and extension

The sensitivities were calculated from the calibration runs as plotted in Figure 3.15:

- $>8 \times 10^{-4} \text{ } ^\circ^{-1}$  in the  $0^\circ$  to  $25^\circ$  range and  $>6 \times 10^{-3} \text{ } ^\circ^{-1}$  in the  $25^\circ$  to  $60^\circ$  range for the MCP joint sensor
- $>1 \times 10^{-3} \text{ } ^\circ^{-1}$  in the  $12^\circ$  to  $65^\circ$  range and  $>7 \times 10^{-3} \text{ } ^\circ^{-1}$  in the  $65^\circ$  to  $90^\circ$  range for the PIP joint sensor.

For the third data acquisition session, these sensitivities were equivalent to more than  $5 \text{ } \Omega^{-1}$ , since both sensors had an initial resistance larger than  $6.9 \text{ k}\Omega$ . The sensor response to joint's flexion and extension formed a hysteresis loop. The maximum width of the loop corresponded to about  $10^\circ$  for both sensors.

Table 3.2 – Mean absolute errors and baseline resistances through all trials, with 100  $\mu\text{m}$  and 50  $\mu\text{m}$  wide gauge tracks.

	100 $\mu\text{m}$ , glue	100 $\mu\text{m}$ , tape	50 $\mu\text{m}$ , tape
$\langle D_{MCP} \rangle \pm \sigma$ ( $^\circ$ )	$8.8 \pm 15$	$7.4 \pm 5.2$	$6.1 \pm 4.5$
$\langle D_{PIP} \rangle \pm \sigma$ ( $^\circ$ )	$11.6 \pm 8.7$	$8.4 \pm 7.0$	$8.3 \pm 7.0$
$\langle R_{0,MCP} \rangle \pm \sigma$ ( $\Omega$ )	$2591 \pm 29$	$2321 \pm 107$	$8137 \pm 179$
$\langle R_{0,PIP} \rangle \pm \sigma$ ( $\Omega$ )	$3020 \pm 19$	$1970 \pm 37$	$6912 \pm 122$

### Quantitative comparison with the camera tracking system

After calibration, the response of the sensor was compared to the reference motion tracking system. Figure 3.16 shows the typical time response of the sensor for nine grasps and finger movements, representative of an entire session.

The absolute deviation  $D$  between the sensors and the reference was computed as:

$$D = |\theta_{sens} - \theta_{ref}| \quad (3.5)$$

where  $\theta_{sens}$  is the angle computed from the response of the sensors' pair and  $\theta_{ref}$  is the output of the reference motion camera tracking system.

Table 3.2 summarizes the results of all runs. The accuracy, defined as the average of  $D$  over all runs of a session after calibration, was minimized to  $6.1^\circ$  for the MCP angle and  $8.3^\circ$  for the PIP angle, respectively, across all tasks. Eliminating the dead-zone by slightly pre-stretching the sensors when using the tape resulted in higher accuracy. The baseline of the sensors was also stable over the whole test session. No overshoot was observed, and the sensors could capture movement lasting as quick as 250 ms when the hand was closed to catch the bottle.

Finally, no significant improvement in accuracy was observed when decreasing the meander track width from 100  $\mu\text{m}$  to 50  $\mu\text{m}$  to increase the strain gauges resistance. The accuracy of the sensors was ultimately limited by the width of the hysteresis loop. Mechanical cross-talk might also explain the lower accuracy in the PIP angle measurement.

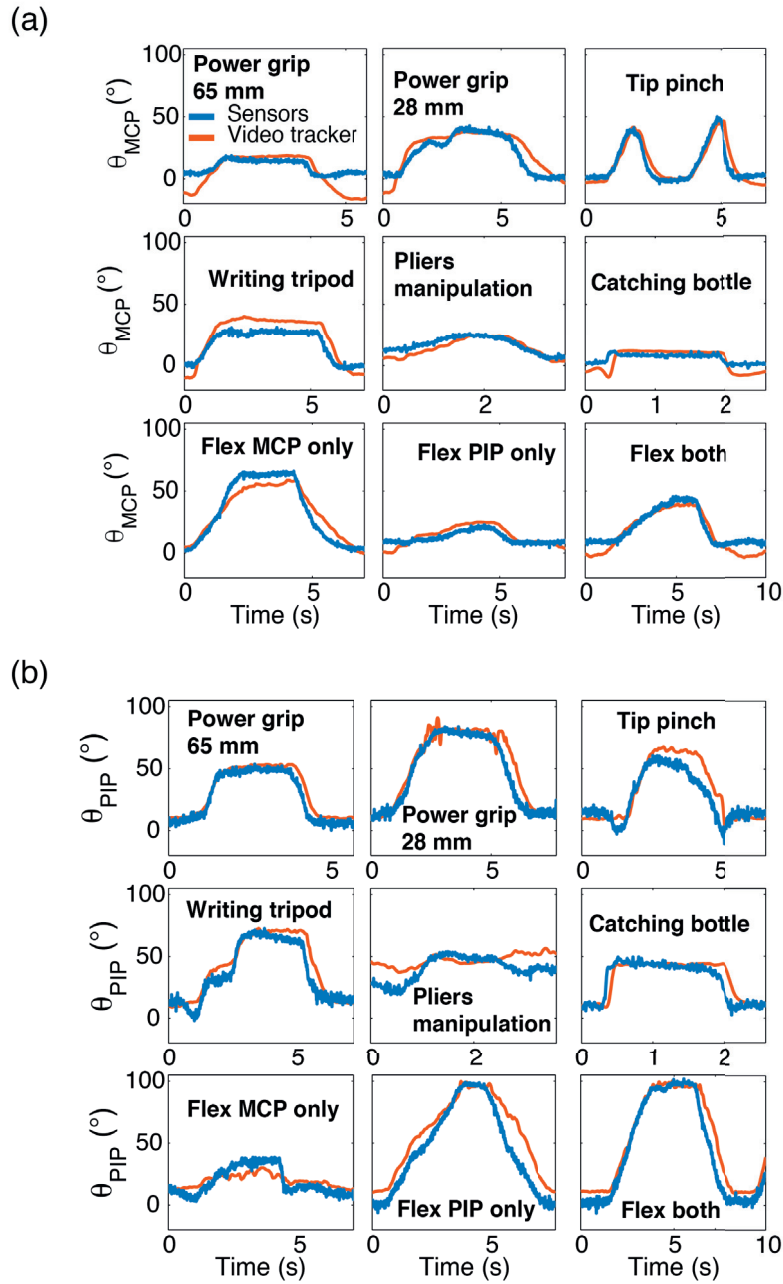


Figure 3.16 – Evaluation of the accuracy of the epidermal strain sensors for joint motion encoding. Comparison between the index (a) MCP and (b) PIP angles sensed by the camera tracking system (orange) and by the soft skin-like sensor pair (blue) after calibration for nine different tasks. A ten points moving average filter was applied to the sensor's output.

---

### 3.3.6 Conclusion

I presented resistive strain gauges based on intrinsically stretchable biphasic thin metal films deposited and micro-structured on PDMS substrate. These rubber-like gauges are soft (Young's modulus  $<2$  MPa), with a thickness approaching that of the outermost layer of the human skin ( $<50$   $\mu\text{m}$ ). One single gauge is 24 times more sensitive to large (50 %) axial strain than transverse strain, and quasi-insensitive to normal pressure up to 100 kPa.

I proposed a design integrating a pair of sensors to encode the flexion and extension of human fingers. I demonstrated that the sensors have a fast and stable response, with more than  $10^\circ$  accuracy when compared to a commercial vision based tracking system. The performance was maintained through a wide range of repeated dexterous manipulation tasks. The accuracy of the sensors was ultimately limited the width of their hysteresis loop.

### 3.4 Combining micro-cracked gold and micro-plotted liquid metal wires for skin-like multidirectional strain sensors

#### 3.4.1 Motivation

The three stretchable sensing systems presented in sections 3.1 to 3.3 are limited to the detection of a uniaxial strain along a pred-defined direction. However, extracting arbitrary 2D strain vectors is critical to monitor motion or deformation of complex structures, including body joints with multiple degrees of freedom like the ankle or the wrist [53, 123, 173].

#### 3.4.2 Design and fabrication of the sensors

##### Design

Orientation and magnitude of uniaxial applied strain could be determined using three strain gauges arranged in a rectangular rosette configuration (Figures 3.17 and 3.18). One of the three sensors, A-B-C, was first stretched along its long axis in order to determine the average gauge factor  $\overline{GF}$  of all three branches in the rosette. After this calibration step, the strain in each sensor A,B and C was determined using

$$e_{A,B,C} = \frac{1}{\overline{GF}} \left( \frac{\Delta R}{R_0} \right)_{A,B,C} \quad (3.6)$$

In the rectangular rosette configuration, the principal strains  $e_1$  and  $e_2$  and their orientation  $\theta$  can be derived from the strains sensed by gauges A, B and C[131]

$$e_{1,2} = \frac{e_A + e_C}{2} \pm \frac{1}{\sqrt{2}} \sqrt{(e_A - e_B)^2 + (e_C - e_B)^2} \quad (3.7)$$

$$\theta = \frac{1}{2} \tan^{-1} \left( \frac{e_A - 2e_B + e_C}{e_A - e_B} \right) \quad (3.8)$$

The angle  $\Phi_1$ , between direction A and  $e_1$ , is determined from  $\theta$  by comparing between  $e_A$ ,  $e_B$  and  $e_C$  (see Appendix A.7 page 127) [174].

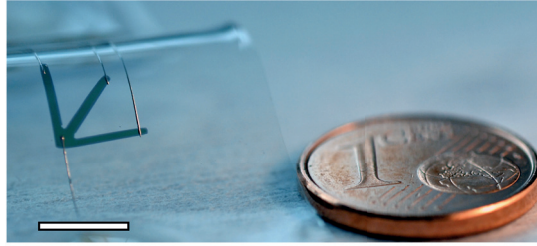


Figure 3.17 – Picture of a rosette made of stretchable gold thin film connected with EGaIn wires. Scale bar is 5 mm.

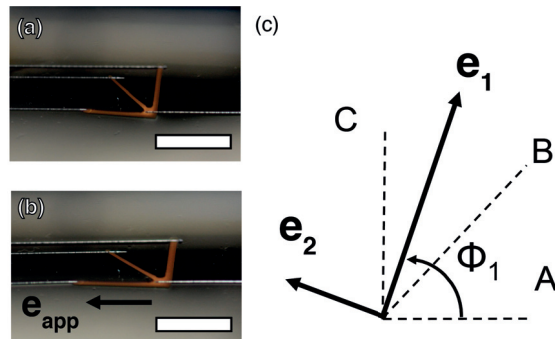


Figure 3.18 – Rosette under (a) 0% uniaxial strain and (b) 50% uniaxial strain. Scale bars are 5 mm. c) Orientation of the two principal strains relative to the three branches of the rosette.

## Fabrication

Three gauge were fabricated according to the process detailed in Appendix sections A.1.1 and A.1.2 page 117. To summarize it briefly, 5/40 nm Cr/Au bilayer was evaporated through a shadow mask on a 120  $\mu\text{m}$  thick PDMS substrate to form the rosette. EGaIn microwires were then deposited to connect each gauge independently. Ag wires were inserted to contact each microwire's end and secured with silicone sealant. Finally, a PDMS encapsulation layer was spin-coated and cured. The total thickness of the integrated rosette was less than 0.5 mm.

### 3.4.3 Detection of uniaxial strain magnitude and orientation

Figure 3.19 presents the outputs of the strain gauge rosette.  $e_2$  was not null but remained smaller than  $e_1/10$  thanks to the small transverse sensitivity of the gauges. When the applied strain was aligned with one of the sensors, the computed angle clearly matched one of the gauge direction (Figure 3.19c). Arbitrary strain orientation was also detected (Figure 3.19f).



### 3.4. Combining micro-cracked gold and micro-plotted liquid metal wires for skin-like multidirectional strain sensors

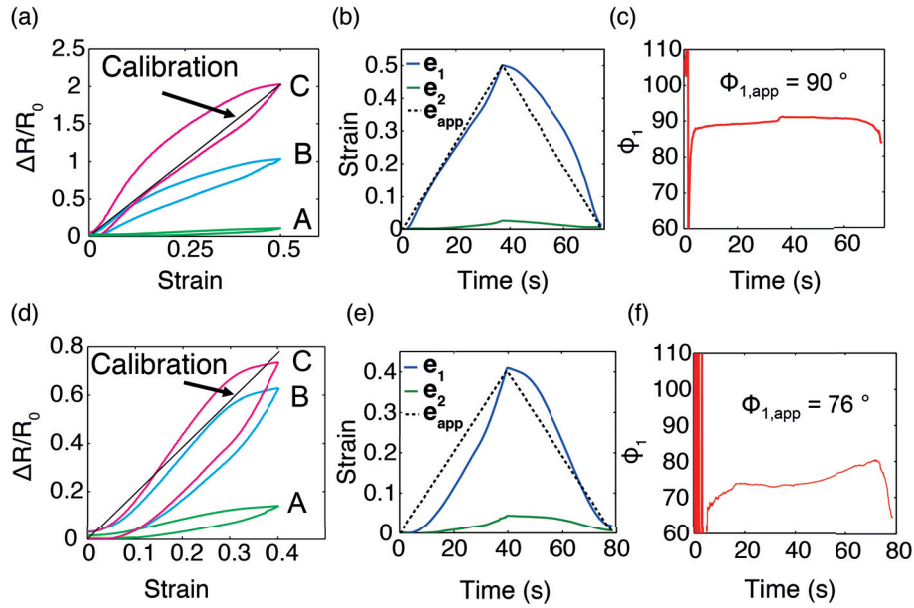


Figure 3.19 – Detection of principal strains magnitudes and directions with a stretchable strain gauge rosette. Relative increase in resistance of branches A,B and C (a), computed magnitude of principal strains (b), and computed orientation of the first principal strain (c), for a 50% maximal applied strain with an angle  $\Phi_{1,app} = 90^\circ$  relative to branch A. Relative increase in resistance of branches A,B and C (d), computed magnitude of principal strains (e), and computed orientation of the first principal strain (f), for a 50% maximal applied strain with an angle  $\Phi_{1,app} = 76^\circ$  relative to branch A.

#### 3.4.4 Detection of isotropic strain magnitude

The soft metal sensor skin could also reliably monitor isotropic strains. A PDMS circular membrane (about 50 mm in diameter) with a strain rosette integrated at its center was attached on top of a mechanical support with a 30 mm diameter hole at its center. The three gold tracks of the rosette were oriented radially from the center of the membrane. The common contact of the rosette was aligned with the center of the hole and the tip of an indenter. A load frame (Criterion C42.503, MTS) was used to control the indentation depth. A small piece of PDMS (1 mm in diameter, 1 mm in thickness) was placed between the hard indenter and the soft membrane in order to minimize undesired local stress concentration at the center of the membrane. Figure 3.20 shows the freestanding circular PDMS membrane with a rosette integrated at its center indented using the load frame.

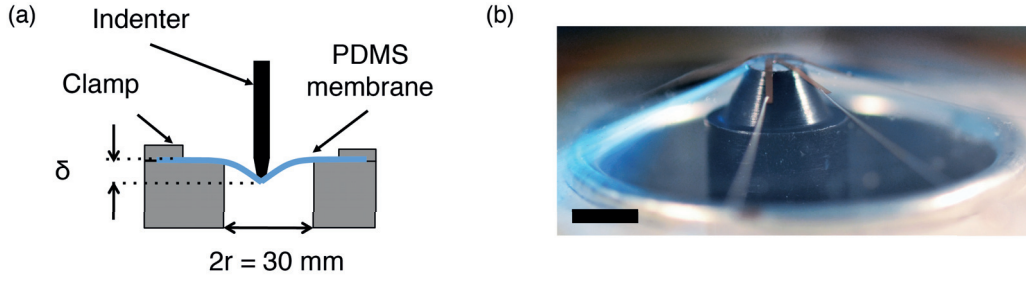


Figure 3.20 – Set-up for isotropic deformation of the rosette. (a) Schematic of the experimental set-up used for inducing isotropic strain in the rosette. (b) Deformation of a PDMS membrane with integrated strain rosette during indentation. Scale bar is 5 mm.

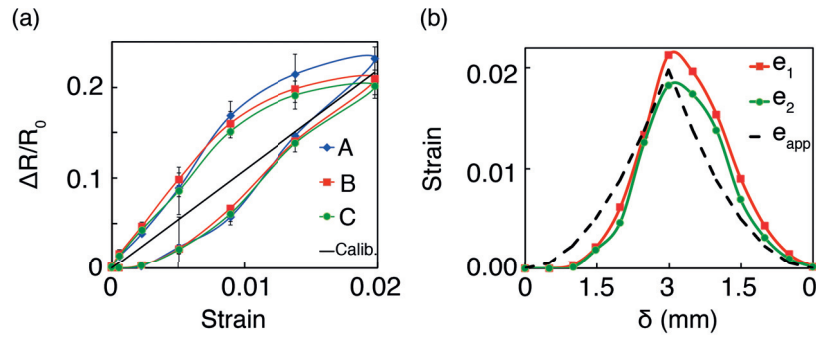


Figure 3.21 – Detection of isotropic strain using with a stretchable strain gauge rosette. a) Relative increase in resistance of gauge A, B and C as a function of approximated applied mechanical strain. Errors bars represent 95% confidence interval. b) Magnitude of principal strains computed from the sensors' outputs as a function of indentation depth  $\delta$ .

An approximation of the strain induced in the membrane was calculated from:

$$e_{app} = \sqrt{1 + \left(\frac{\delta}{r_m}\right)^2} - 1 \quad (3.9)$$

where  $r_m = 15$  mm is the radius of the circular membrane, and  $\delta$  is the indentation depth (between 0 mm and 3 mm). I did not take into account non-linearity in the membrane profile,[175] nor local microscopic strain concentration at the edge of the tip. The relative increase in resistance in the three branches of the rosette were almost identical (Figure 3.21a), thus the magnitude of the two principal strains  $e_1$  and  $e_2$  were similar (Figure 3.21b). In this situation,  $\Phi_1$  remained indeterminate since  $e_A \simeq e_B \simeq e_C$  [174].

### **3.4. Combining micro-cracked gold and micro-plotted liquid metal wires for skin-like multidirectional strain sensors**

---

#### **3.4.5 Conclusion**

In summary, I utilized a combination of stretchable gold thin films and liquid metal microwires to produce soft metal electronic skins capable of detecting multi-axial strains. By arranging the strain sensors in rectangular rosettes and applying the classical strain gauge theory, I was able to measure the magnitude and direction of arbitrary uniaxial strain and to discriminate between uniaxial and isotropic strain fields up to 50% strain.

---

### 3.5 Summary and outlook

I presented applications of stretchable metallizations to localized strain sensing. Strain sensors with custom designs were formed from micro-cracked gold and liquid metal wires to track humanoid robot and human finger flexion and extension. They proved particularly useful to encode grasping in conjunction with soft tactile sensors. Next, I could track finger joints' rotation over using micro-patterned epidermal strain gauges made from biphasic thin films, with an accuracy of below  $8.3^\circ$  over eleven grasping and movement tasks covering most of the range of motion of the human index finger. Finally, the micro-cracked gold films and the liquid metal wires were arranged in a rosette configuration to monitor direction and magnitude of large (up to 50%) uni-axial and multi-axial strains. The extensive characterization and demonstrated stability of the soft sensors let us envision a translation to robotic and therapeutic applications. Beyond their accuracy, the sensors fulfilled the requirements for truly skin-conforming motion sensing: they are unobtrusive, adjustable and can be integrated in a portable system.

For hand tracking applications, further developments could include optimizing the design of the sensors to encode the thumb movement, which has a more complex range of motion due to its saddle joint. Calibration schemes involving no external reference system should also be investigated.

The epidermal strain sensors presented a number of advantages for finger motion encoding since they are unobtrusive and do not rely on vision. For that reason they can be used in a cluttered environment and leave the user's hand free for manipulation tasks. This is especially interesting in a hospital setting where a clinician estimates the impairment of a patient's hand. The sensors are currently being evaluated by our group to monitor the tremors of Parkinson patients at Lausanne university hospital (CHUV).

### 3.6 Contributions

For the work presented in section 3.1, I designed and fabricated the sensors and their readout circuits. I carried out the experiments with the iCub robot, analyzed the data, and wrote the paper together with Prof Lacour.

For the work presented in section 3.2, I designed and fabricated the finger bending sensors in coordination with Dr Aaron P Gerratt (APG) who designed and assembled the soft tactile sensors. I also participated in the readout circuit design and implementation of the compensation scheme. APG and I finally designed and performed the glove characterization experiments, analyzed the data and wrote the paper with Prof Lacour.

For the work presented in section 3.3, I designed and fabricated the sensors together with Séverine de Mulatier (SdM) as part of her master thesis under my supervision. SdM carried

out the uniaxial stretching experiments and normal pressure experiments. We performed the first set of experiment with the video tracking system and wrote the data extraction code together. Laurent Dejace fabricated the second and third epidermal sensors batch and we carried out the corresponding experiments together. I analyzed the data and wrote the paper together with Prof. Lacour.

For the work presented in section 3.4 I designed and fabricated the sensors. I carried out the experiments and analyzed the data. I wrote the paper together with Prof Lacour.



## 4 Tactile sensors and micro-heaters with biphasic film metallization

In section 4.1, I present my contribution to the WiseSkin project aimed at restoring tactile sensation for amputee patients. Section 4.2 reports on stretchable micro-heaters made from biphasic thin films conductors.

Section 4.2 is based on the following publication:

- A. Hirsch, H. O. Michaud, A. P. Gerratt, S. de Mulatier, and S. P. Lacour. Intrinsically Stretchable Biphasic(Solid–Liquid) Thin Metal Films. *Advanced Materials*, 28(22):4507–4512, 2016.

---

## 4.1 Powering skin for miniaturized wireless MEMS pressure sensor nodes

### 4.1.1 Context and motivation for the study

About 3500 and 5200 persons undergo upper limb amputation in Italy and in the UK each year, respectively [176]. Patients can now benefit from motorized myoelectric hand prostheses controlled through muscle command signals recorded on the stump of the user. The most advanced commercial models offer many degrees of freedom and grasp postures (see Figure 4.1). However, they do not provide any sensory feedback to the user who have to rely on vision to assess if they are performing grasps correctly, a very unnatural control strategy. Patients may even prefer to switch back to less advanced solutions such as body-powered hooks that provide a greater sense of body ownership.

In fact, among other factors such as discomfort, the lack of tactile feedback is one of the reasons for upper-limb prosthetics abandonment identified in surveys [96, 177]. Promising steps have been recently demonstrated for restoring tactile sensation in a feedback loop, in particular through mechanical stimulation of the phantom limb or the chest [178, 179], and through electrical stimulation of the peripheral nerves in human amputees [116, 120]. However, those pioneering studies relied only on discrete and/or bulky sensors to encode finger force, limiting the system's relevance for daily use and conveying a limited amount of sensory information.

Innovative approaches are needed to compensate the lack of tactile sensory systems covering a prosthetic hand and providing precise force transduction over a large dynamic range. The aim of the WiseSkin project was to engineer a wearable skin system to restore tactile feedback for upper-limb amputees. The system should be conformable enough to guarantee freedom of movement and comfort for the user. Finally, the system was designed to be scalable to a large number of ultra-low-power (ULP) sensors thanks to wireless communication [180]. The system concept is illustrated in Figure 4.2.

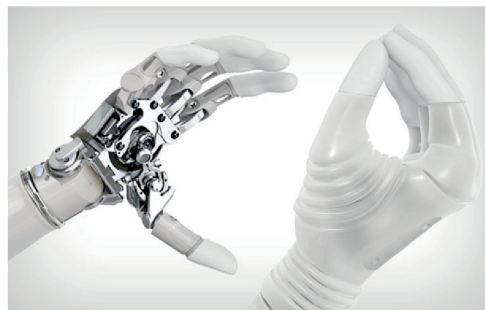


Figure 4.1 – The Otto Bock Michelangelo myoelectric prosthetic hand. Image copyright Otto Bock GmbH.



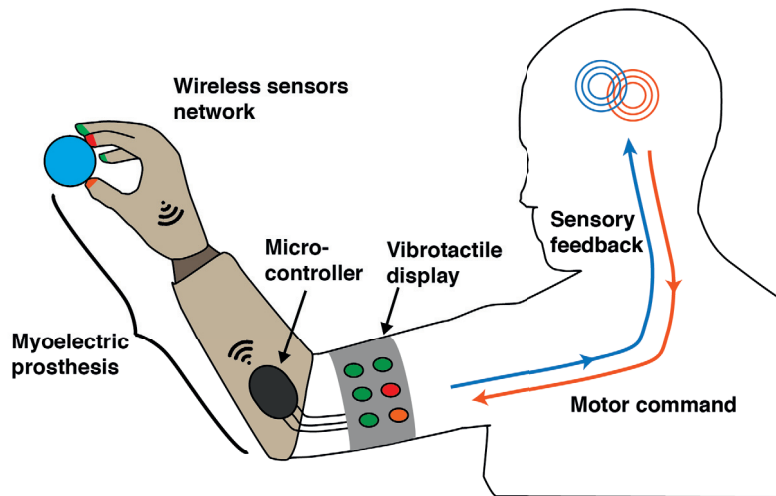


Figure 4.2 – Schematic illustration of the WiseSkin sensory feedback system. A myoelectric upper limb prosthesis is equipped with a wireless tactile sensor network. The network transduces grasping force and sends data to a micro-controller which activates a vibrotactile display on the stump of the amputee. The patient can then adjust his/her grasping force according to received sensory feedback.

My contribution to the WiseSkin project was to engineer a conformal power distribution system, which fulfilled three roles:

- power each sensor nodes.
- act as a waveguide for wireless communication.
- maintain electromechanical integrity when the finger bends.

### 4.1.2 Materials and methods

#### Design of the sensor nodes

The sensor nodes were provided by CSEM SA (Neuchâtel, Switzerland) and are displayed Figure 4.3. The main elements of the sensor nodes were of a barometric MEMS pressure sensor (LPS25H, STMicroelectronics), a microcontrolling unit (MSP430F5528, Texas Instruments) and a radio for Bluetooth Low Energy (BLE) wireless data communication (iCyTRX, CSEM SA). Each node had DC power supply pins on top (3 V) and bottom (ground).

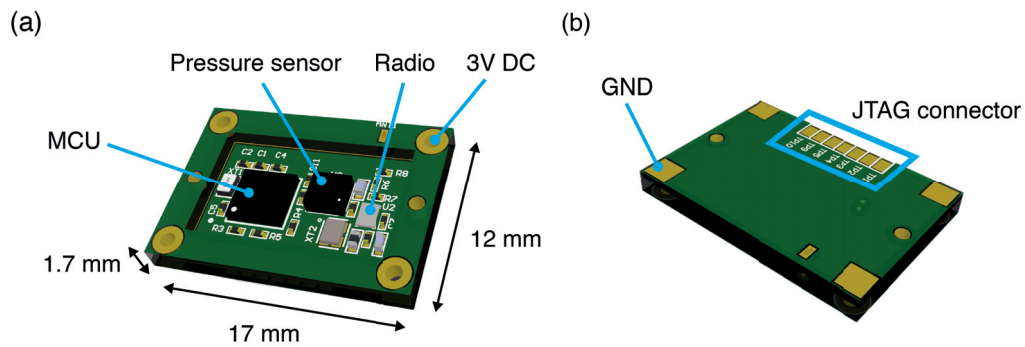


Figure 4.3 – Design of the WiseSkin sensor nodes. a) Top side. b) Bottom side. The sensors feature a MEMS pressure sensor, a micro-controller unit (MCU), a radio for wireless communication, contact pads for 3 V DC voltage powering, and a Joint Test Action Group (JTAG) connector for programming.

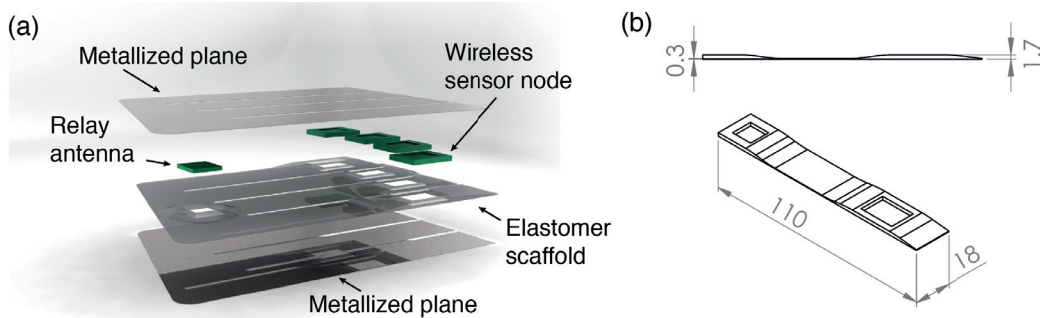


Figure 4.4 – Conformal power distribution system for the WiseSkin project. a) General conceptual view of the power distribution system. Wireless sensor nodes are embedded in a silicone scaffold and sandwiched between two metallized planes that power the sensor nodes and form a wave-guide for wireless communication. b) Side view and isometric view of the fabricated finger-sized scaffold. Dimensions are in mm.

### Design and fabrication of the soft skin

**Design** The concept and design of the power distribution system is presented in Figure 4.4. The skin system was initially designed to fit the palm of the hand prosthesis. Since processing of the stretchable metallization was limited to 100 mm diameter wafers, I designed a proof-of-concept system fitting one finger of the hand. The finger strip fitted a commercial hand prosthesis (Ottobock Digital Twin 8E38=7).

**Fabrication** I fabricated fully elastomeric skin systems fitting one finger using the process flow in Figure 4.5. The scaffold was made from PDMS molded in a custom polyoxymethylene (POM, Angst & Pfister) mold. PDMS planes were cut using a cutting plotter (ROBO Pro, Graph-tec) and metallized with a stretchable biphasic (solid-liquid) thin film pattern composed of

#### 4.1. Powering miniaturized wireless sensor nodes

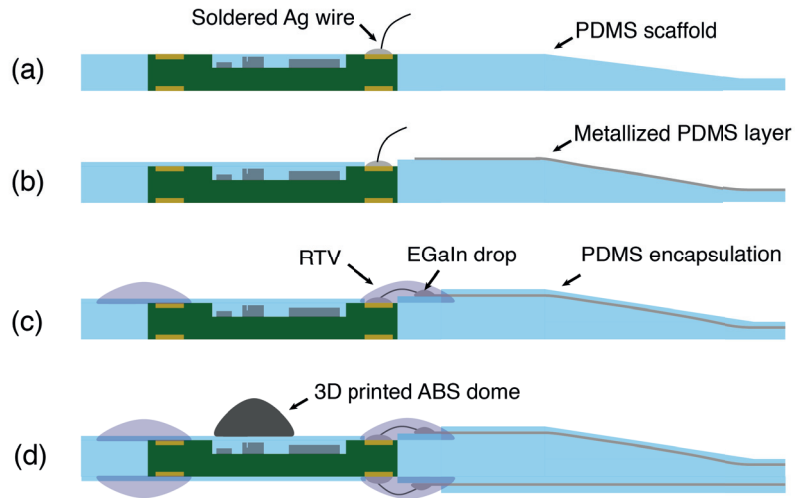


Figure 4.5 – Process-flow for the integration of the WiseSkin sensor node into the soft strip system. a) Soldering of an Ag wire to the powering pad and insertion of the node into the PDMS scaffold. b) Bonding of the metallized PDMS layer on the scaffold. c) Connection of the to the stretchable metallization using an EGaIn drop as buffer, securing and encapsulation with a PDMS layer. d) Connection of the bottom side of the sensor and gluing of the 3D printed ABS dome.

five  $1 \times 75 \text{ mm}^2$  lines separated by 1 mm [125]. The integration process started by soldering a  $75 \mu\text{m}$  silver wires to the connection pads and inserting the sensor node into the scaffold. Then a metallized PDMS plane was bonded using PDMS and RTV silicone sealant (734, Dow Corning) as adhesives between the scaffold and the metallized plane. The electrical connection was then established using a drop of EGaIn (Sigma Aldrich) as a conductive buffer and secured with silicone sealant. Silicone sealant was also used to secure the physical connection between the sensor node and the scaffold. Finally a PDMS encapsulation layer was applied by dip coating. The same operation was repeated to connect the bottom side of the sensor node.

3D printed ABS plastic domes (6 mm in diameter, 2.5 mm in height) were glued on top of the pressure sensors to ensure a single point of contact between the sensor node and the external force applied (see also Figure 4.7a).

After fabrication of the stretchable skin systems, the metallized plane were connected to a 3 V DC battery pack. The soft strip could be manipulated and mounted on the prosthetic hand without failure as displayed in Figure 4.6.

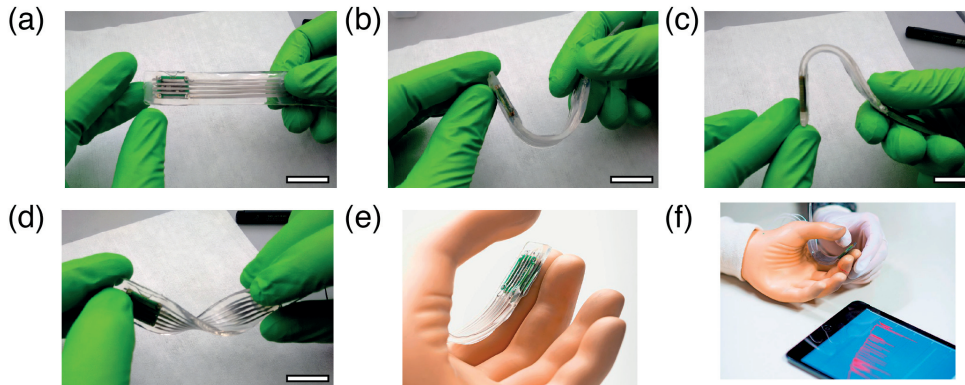


Figure 4.6 – Rigid sensor node integrated in a the soft strip. a-d) Sensor node can be bend in both directions and twisted. e-f) Sensor node mounted on the Ottobock Digital Twin 8E38=7 prosthetic hand. Pictures copyright Matthieu Spohn.

#### Characterization set-up

The skin system was attached to the Ottobock hand prosthesis using tape. I applied a controlled force on the sensors embedded in the skin system using a load frame (Criterion C42, MTS) equipped with a 100 N load cell (MTS). The hand was tied to a stand and positioned with its palm facing the load frame indenter. Pressure data from the sensors nodes was streamed to an iPad via Bluetooth Low Energy (BLE) protocol. A custom LabView interface streamed the data from the iPad to a computer. Acquisition rates were 10 Hz for load cell (force) data and 16.6 Hz for the sensor nodes (pressure) data. The indentation speed was kept constant to  $0.2 \text{ mm s}^{-1}$  while the maximum applied force was varied between 0 N and 20 N.

#### 4.1.3 Results and discussion

As illustrated in Figure 4.7 the sensor integrated in the fully elastomeric skin system had a low hysteresis and a large signal to noise ratio (RMS noise of the ST LPS25H sensor is 1 Pa [181]) in the 0 N to 20 N force range. The sensors also had a very high linearity ( $R^2 > 0.99$ ). Also, as show Figure 4.6, the rigid node circuit board integrated into the soft scaffold could be manipulated without failure of the electrical connection provided by the stretchable metallization.

However, there were a few limitations of the system that are listed below:

- the length of the soft connection tracks was limited. The peak current consumption of a sensor node was 10 mA. For  $50 \times 1 \text{ mm}^2$  tracks with a sheet resistance of  $0.5 \Omega/\text{sq}$ , the resistance per track was  $25 \Omega$ . If two tracks were used in series with the sensor nodes, the total track resistance was then  $50 \Omega$  and the voltage drop in the interconnects at peak current is 0.5 V, which leaves 2.5 V at the nodes terminal. The node component

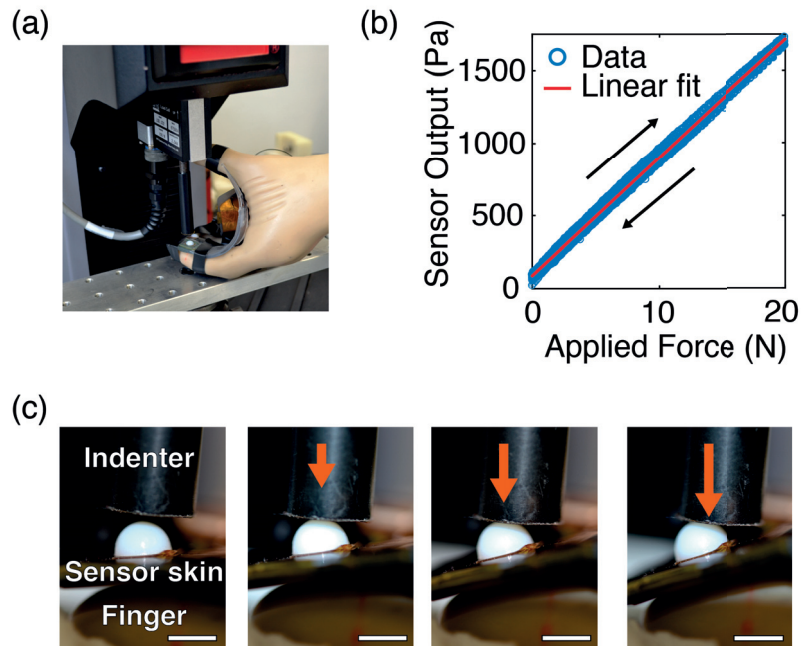


Figure 4.7 – Characterization of the sensor nodes inserted in the power distribution system and mounted on the Ottobock prosthesis. a) Picture of the hand installed in the indenting set-up. b) Output of the sensor integrated in the soft strip as a function of applied force. 10 loading and unloading cycles are represented.  $R^2 > 0.99$  for linear fit. c) Picture of a strip integrated on a finger while applying increasing force using the load frame. The role of the 3D printed dome is highlighted since the finger bent during testing. Scale bars are 5 mm.

requiring the highest supply voltage was the MCU with 1.8 V [182]. Hence, with a 3 V battery, the total track resistance should be maximum 120  $\Omega$ .

- electromigration must be considered as a potential failure mode after long term use.
- it was observed that the sensors were sensitive to temperature, with significant drift (equivalent to more than 500 Pa pressure read) when touched with a finger. Sensitivity to temperature was observed once the MEMS pressure sensor was encapsulated in PDMS, before and after integration into the skin system. This should be compensated by using an embedded temperature probe for instance.

#### 4.1.4 Conclusion

I proposed an conformal power distribution system to provide mechanical support and electrical power to rigid wireless sensor nodes into a soft skin-like. The system consisted in a silicone scaffold for inserting and maintaining the node in place, and two stretchable powering layers. I demonstrated that the skin system could be bent in both directions and twisted while maintaining its electromechanical integrity. Finally, I showed that the integrated sensors could

---

be installed on a prosthetic hand to acquire and transmit normal forces in the 0 N to 20 N range with excellent linearity and no hysteresis.

## 4.2 Skin-like resistive micro-heaters array

### 4.2.1 Context and motivation for the study

When electrical current passes through a conductor, heat is produced. The phenomenon is known as Joule heating. If the conductor is modeled as a resistor  $R$  through which passes a direct current  $I$ , the total thermal power dissipated in the conductor  $P$  is given by:

$$P = RI^2 \quad (4.1)$$

Recent development of micro-fabricated Joule heaters on flexible or stretchable carriers opened opportunities in noninvasive or minimally invasive biomedical mapping by measuring characteristics such as conductivity and heat capacity of the human skin, with application to hydration quantification or treatment of some dermatologic diseases [27]. Micro-heaters were also applied to thermally activated micro-pumps for localized drug delivery in miniturized wireless devices [183], in instrumented probes for wound healing or thermal tumor ablation [184], and in silicone micro-tubes for flow-rate measurement using hot-wire anemometry [185].

In this section, I combined lift-off micro-patterning of biphasic gold-gallium thin films and multilayer assembly methods to fabricate resistive Joule heaters.

### 4.2.2 Materials and methods

#### Design of the micro-heater array

The micro-heaters were arranged in a matrix as shown Figure 4.8. In this study the row and column contacts were manually connected to activate each heater or row/column individually, but a matrix of resistors can be addressed digitally using a micro-controller and multiplexers on row and columns [186].

#### Fabrication

The soft micro-heaters array consisted of two PDMS-biphasic conductors membranes. The bottom membrane was a 40  $\mu\text{m}$  thick PDMS substrate metallized with the biphasic conductors using lift-off patterning described in Appendix section A.1.3 page 118. The top layer was a 90  $\mu\text{m}$  thick PDMS substrate, metallized using lift-off micro-patterning, and further punctured at locations corresponding to the sites of the vias using a hole puncher (Technical Innovations). The top layer was then peeled-off from the PDMS slab, plasma activated, aligned and bonded to the bottom membrane which was previously metallized. Drops of gallium indium eutectic were then deposited in the vias to form a conductive bond between the two

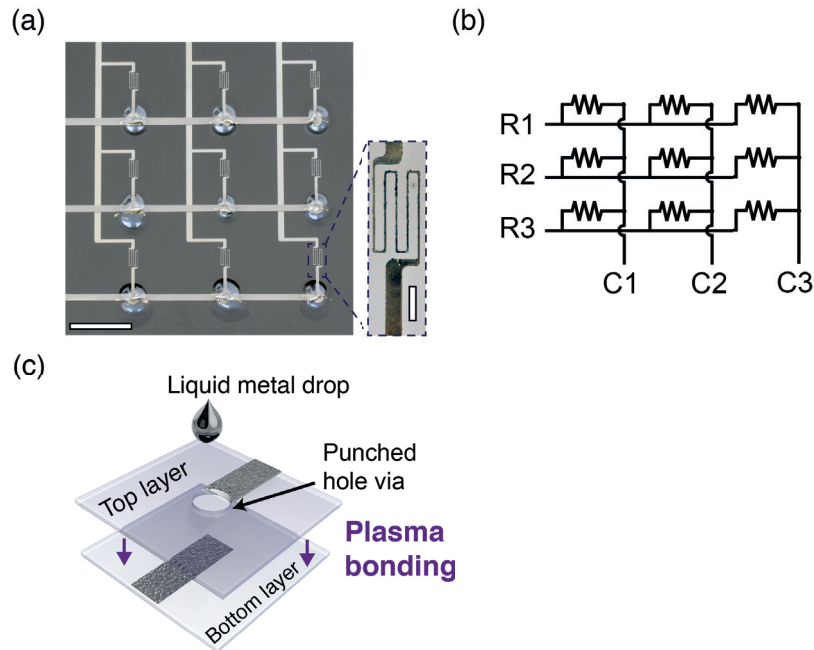


Figure 4.8 – a)  $3 \times 3$  matrix of micro-heaters. Scale bar is 10 mm for matrix view and 1 mm for magnified microheater view. b) Equivalent electrical circuit. c) Schematic description of the method for multilayer electrical connection.

metallized membranes, and encapsulated with RTV silicone sealant (734, Dow Corning). A PDMS encapsulation layer was finally spin-coated with a PDMS and cured. The total thickness of the soft micro-heating membrane was  $330 \mu\text{m}$ .

### Characterization set-up

The heaters were actuated with a direct current (DC) source (2400, Keithley). A thermal camera (A325 sc, FLIR Systems) and close up lens ( $1 \times 25 \mu\text{m}$ , FLIR Systems) was used to monitor the temperature at the surface of the samples in stationary regime. The soft heaters were placed on a plastic support, with observed surface exposed to ambient air during temperature monitoring.

### 4.2.3 Results and discussion

Figure 4.9 presents the results of characterization of the heaters using the infrared camera. I varied the actuation current between 10 mA and 30 mA. At the largest actuation current (30 mA), the micro-heaters generated a surface temperature gradient of more than  $20 \text{ }^\circ\text{C mm}^{-1}$ . The soft epidermal thermal actuators provided a well-controlled heat source on the skin (Figure 4.9). When mounted on a human arm, the soft micro-heating matrix provided localized



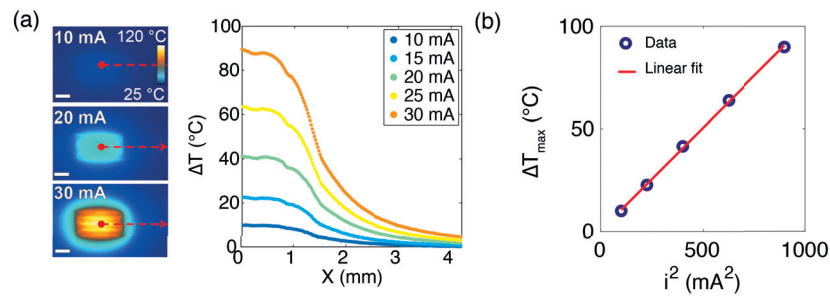


Figure 4.9 – Characterization of a soft micro-heaters matrix. a) Infrared images of a micro-heater actuated with increasing current, and temperature increase along the x-axis indicated by the red arrows. Scale bars are 1 mm. b) Maximum increase in temperature in the soft heater area as a function of the square of the DC current passing in the tracks.  $R^2 > 0.99$  for linear fit.

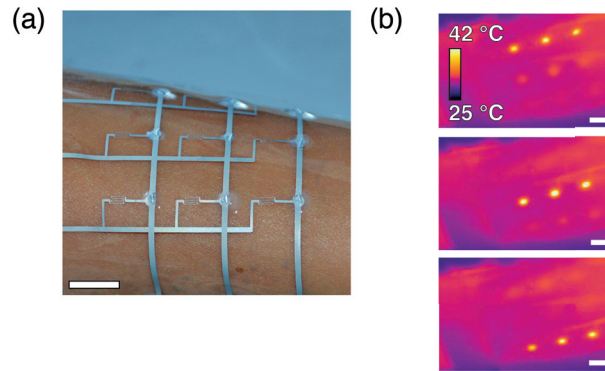


Figure 4.10 – Optical and infrared imaging of the soft heaters matrix. a) Soft matrix of micro-heaters wrapped on a human arm. b) Infrared images of a  $3 \times 3$  matrix of microheaters on the human forearm while sequentially heating one row after the other. Scale bars are 10 mm.

heat sources distributed over a large area as shown Figure 4.10.

The biphasic metal displayed a thermal coefficient of resistance of  $1.43 \times 10^{-3} \text{ K}^{-1}$  (see Appendix A.8 page 128). Monitoring the sensor resistance can be a solution to control the heat produced. However, other sources of resistance variation including stretch should be taken into account or minimized by locally increasing the substrate's stiffness for example [187].

In case of a continuous activation of the heaters, the circuit could fail rapidly due to liquid electromigration generated by the large current densities as exposed section 2.3.6 page 53. The life-time of the device could be extended by using alternative current (AC) actuation as opposed to DC actuation [146, 188].

---

#### 4.2.4 Conclusion

I utilized the multilayer and micro-patterning fabrication processes for biphasic gallium-based thin films to construct a stretchable matrix of individually addressable micro-heaters. The reduction of conductive traces width to 50  $\mu\text{m}$  enabled a localized increase of temperature of up to 80  $^{\circ}\text{C}$ . Thanks to its minimal thickness ( $<350\ \mu\text{m}$ ), the rubber matrix could be easily wrapped around a human arm.

### 4.3 Summary and outlook

In this chapter, I demonstrated two additional applications of the biphasic film technology. In the first one, stretchable biphasic film tracks powered rigid wireless tactile sensor nodes integrated in a silicone scaffold. The sensors were mounted on a prosthetic skin and reliably encoded forces in the 0 N to 20 N range. Then, conformal micro-heating membranes providing localized and controlled heat sources were assembled to provide localized temperature increase.

Both applications relying on DC current powering, the impact of electromigration on long-term circuits durability should be considered. Future improvement for thicker and more uniform films should translate to prolonged lifetime for these devices.

As of today, the WiseSkin collaboration received ethical approval to evaluate the system with patients at Balgrist University Hospital in Zürich. The tests protocol includes passive tactile task where the patient uses the sensory feedback to determine which of his/her fingers is stimulated, and active tactile tasks where he/she manipulates fragile objects and discriminates objects with variable hardness.

### 4.4 Contributions

For the work in section 4.1, I designed and fabricated the scaffold and metallization layers. I integrated the sensor node provided by CSEM SA and performed the characterization experiments.

For the work in section 4.2, I designed, fabricated and characterized the samples. I used the multi-layer process developed by Arthur Hirsch, who also performed the TCR measurements reported in the Appendix.

# 5 Conclusion

## 5.1 Summary and impact of the contribution

Electronic skins are an innovative class of large-area electronics inspired by nature and expected to cover human or artificial limbs and provide unique wearable sensing and actuation capabilities. Applications include quantification of the motion and grasping force of the hand to restore tactile sensation in prostheses' users or to monitor impaired patients. Stretchable circuits are a promising solution to achieve this vision since they can easily conform to moving three dimensional bodies. A critical building block for such systems is the interconnects that carry electrical power and signals. They should accommodate potentially large deformations and be compatible with large area, high throughput production.

In this thesis, I presented the design, implementation and characterization of stretchable metallization techniques enabling:

- the assembly of soft and thin imperceptible transducers.
- the interconnection of standard solid-state electronics in rubber-based matrices.

The developed techniques were then applied to construct thin strain sensors encoding the rotation of finger joints and to power rigid wireless tactile sensors nodes embedded in a rubber scaffold and mounted on a prosthetic hand. The obtained transducers were finally tested in realistic use cases.

### 5.1.1 Stretchable metallization technologies

Two approaches for stretchable electronic conductors were investigated: solid microcracked thin films and liquid metals.

Stretchable microcracked thin metal films were introduced about fifteen years ago and ex-

---

tensively studied to understand the physical mechanism and process parameters allowing for reversible stretchability [189]. In this work, I analyzed the relation between initial film morphology, sheet resistance and gauge factor at large strains. As for thin metal films under microscopic strains, there is a thickness range in which the stretchable thin film have a minimum and well defined gauge factor. Moreover, I showed that a track with a length/width ratio of ten behaved like a conventional metal foil strain gauge with a transverse sensitivity twenty times smaller than longitudinal sensitivity. Thus, a classical equation framework was used to determine uniaxial and isotropic 2D strain directions and magnitude. Combining the micro-cracked thin films with microplotted liquid metal wires allowed for fully stretchable, integrated multi-sensors systems with localized strain sensitivity.

I proposed a novel deposition and patterning method for gallium-based conductors. Gallium was deposited in the vapor phase on silicone substrates pre-coated with solid metal thin films. The interaction between the solid metal phase and the liquid gallium phase created and maintained a continuous metallic film even at very large strains. This film had exceptional electromechanical properties including a low sheet resistance ( $0.5 \Omega/\text{sq}$ ), low gauge factor ( $\approx 1$ ), conduction up to 400% strain and stable electrical properties even after a million cycles at 50% strain. Thanks to the low film thickness ( $<1 \mu\text{m}$  on average), I could developed a lift-off patterning method to achieve centimeter-long lines with width down to  $10 \mu\text{m}$  which maintained conductivity up 70% strain.

An important point is that the liquid metal films were deposited and patterned using standard industrial equipment and processes, guaranteeing straightforward transfer to batch production of large area circuits.

### **5.1.2 Skin-like sensors**

I used the novel stretchable conductor technologies to construct strain and tactile sensors that can be worn on the finger.

A novel combination of skin-like sensors was achieved by mounting stretchable strain gauges on the dorsal side and stretchable pressure sensors on the palm side of a glove. The strain gauges not only to recorded joint motion without movement impediment but also compensated for motion artifacts in the pressure sensors response. Taken together, the two signals provided a richer and more accurate digital encoding of grasping.

I then utilized the unique properties of gallium-based stretchable films to assemble robust and extremely thin stretchable strain gauges ( $<50 \mu\text{m}$ ). It resulted in an extended accessible range of motion for the epidermal strain sensors mounted on a finger. I quantified the accuracy of

the skin-like sensors for encoding joint rotation while performing fine manipulation tasks.

Finally, rigid wireless MEMS pressure sensor nodes were integrated into a rubber scaffold and powered using biphasic film tracks. The hybrid system could encode normal forces in the 0 N to 20 N range with excellent linearity and signal to noise ratio. It demonstrated the applicability of the biphasic thin film not only to build soft transducers but also to interconnect traditional solid-state electronics in skin-like circuits.

A sufficient technology readiness level was achieved to enable the translation of the sensors to the clinic for evaluation by therapists and patients. The epidermal strain gauges are currently used to monitor the tremors of Parkinson patients at Lausanne university hospital (CHUV), while The WiseSkin collaboration received the authorization to test the wireless MEMS pressure sensors with amputee patients at Balgrist university hospital in Zürich.

## 5.2 Future perspectives and challenges

### 5.2.1 Technological improvements

Micro-cracked gold films grow on silicone only under well defined deposition conditions and thickness range, which limits the possible improvement concerning the conductors deposited using this method. In addition, the micro-cracked texture was obtained with no other metals than gold to date. However, stretchability could be enabled by engineering the cracks pattern into conductive films instead of relying on spontaneous formation. A first proof of concept was demonstrated by Shyu *et al.* using a "kirigami" approach where specific patterns were cut into stiff and brittle conductive composites [65]. The patterns allowed the conductive ligaments to buckle out of plane to minimize the local strain and avoid fracture when the devices experienced large macroscopic strain. Similar strategies could be applied to allow reversible elasticity at large strains in any thin metal or semi-conductor films. In particular, silicon could be employed to assemble highly sensitive strain gauges [190].

For biphasic thin films, the larger process window and notably the possibility to tune the deposited quantity of gallium leaves room for further optimization. However, I observed that the sheet resistance saturated around  $0.5 \Omega/\text{sq}$  independently from the additional amount of gallium deposited. This may come from the non-uniform nature of the film, with the additional deposited gallium aggregating into bulges. Investigating strategies to improve the film uniformity, notably by modifying the substrate, could result in a decreased minimum sheet resistance, and consequently in a mitigation of the electromigration thanks to the reduced current densities.

---

The solid-liquid films also had a unusually low gauge factor ( $\approx 1$ ). Indeed, the gauge factor of metal foils or liquid metal gauges is in general higher than 2, which is well described by theoretical geometrical considerations: the conductor is elongated in the direction of the strain and its cross-section surface area is decreased by the Poisson effect [131]. Since the biphasic films possessed distributed reservoirs of conductive material in the form of gallium bulges, flow of gallium under strain resulting in a more uniform gallium distribution could explain the abnormally low strain sensitivity. Experimental measurement such as profilometry of stretched samples should be conducted to verify this hypothesis.

A last noticeable issue concerning the biphasic films only partially addressed in this thesis is the role of the underlayer in the film's behavior under strain. Namely, I showed that films grown with gold or palladium underlayers presented excellent electromechanical performance, whereas cracks developed in films grown with platinum or iridium underlayers, leading to degraded conduction. However, the reason why some elements were suitable as underlayers and not others remains unexplained. The interaction between the underlayer material and gallium needs to be better understood, specifically in terms of wetting and cracks propagation in the solid phase. This could result in high performance films deposited with more cost-effective underlayers.

### **5.2.2 Future applications for stretchable motion and tactile sensors**

The specific concepts of very compliant motion and tactile sensors developed in this work could be easily transferred to biomimetic robotic or prosthetic hands. For instance, the PISA/IIT SoftHand combines a simple actuation scheme, robustness, and high grasping performance but lacks sensory functions [164]. Equipping it with a skin that can encode its position and grasping force would result in more accurate control for the user without adding complexity in the design of the hand itself.

Lower limb prosthetic users and diabetes patients could also benefit from highly conformal sensory systems that can fit inside a prosthetic socket or shoe sole. In fact, instrumented shoes may prevent ulcer formation in the case of diabetes [191], and sensory feedback helps to improve locomotion for lower limb amputees [192].

Soft robotics is a rapidly evolving research and industrial field which gave birth to highly compliant, elastomer-based grippers, robotic hands or tentacle-like end effectors [166, 193, 194]. Most of the actuators are still lacking sensory feedback, and thin and robust sensors able to withstand the extreme deformations imposed by the soft artificial limbs could enable closed-loop control [195, 196].

Finally, consumer electronics is no more restricted to devices such as smartphones or tablets but is reaching more and more parts of the body, from virtual reality headsets to smart-watches. Healthcare, wellness and self-quantification represent a broad range of applications that could benefit from imperceptible and high performance sensors for long-term use.

### 5.2.3 From discrete sensors to distributed network

To realize the vision of a large number of sensors distributed over large areas in a skin-like system, data treatment would have to be distributed to digitalize and share the sensed signal in a network [197]. Although intrinsically stretchable semiconductors have been recently introduced [198, 199], they only offer very modest performance compared to their rigid counterparts in terms of computational power, power consumption and cost-effectiveness. In a foreseeable future, large area sensor networks will still have to rely on traditional integrated circuits for data treatment and communication. This poses some challenges in terms of integration.

While the extremely high conductivity, robustness and patterning possibilities offered by the biphasic films to, the interface between soft interconnects can still be a mechanical, if not electrical, failure point in hybrid circuits. The transition zone must be carefully managed to avoid mechanical rupture or delamination due to interfacial strain concentration [187]. Efforts to enable the large-scale and high throughput integration of various rigid components in a stretchable matrix are still needed.

In terms of data management, the networks should be able to handle large quantities of data and be robust to failure, maintaining functionality even if one node fails for instance. For this, the WiseSkin concept of independent sensor nodes powered by a soft skin and that communicate in a wireless network is an innovative and promising solution.

### 5.2.4 Industrialization

Stretchable electronics technologies are arriving to the market, but the promise of extremely deformable circuits is still not fully addressed. Companies and research centers including MC10 and IMEC have launched products or advanced prototypes featuring stretchable (spring-like plastic) interconnects that allow for an elastic design [200, 201]. But the overall compliance of these devices is limited and the interconnects are sensitive to fatigue and rupture under repeated stress, even at strains <10% [73]. Samsung recently demonstrated a stretchable display based on proprietary patterning of micro-cavities that can stretch to 5% [202]. Stretchable inks are an alternative technology but offer low conductivity and fail around 30% of strain [203]. Finally, textile – fiber-based - interconnects are also explored but high densities of interconnects, connection to components and resistance to wear remain a challenge [204].

---

For now, products compatible with repeated large (>50%) strains are limited to capacitive strain sensors based on textile or carbon electrodes available for example from StretchSense or Parker Hannifin [205, 206].

From our discussions with established businesses and start-up founders, we realized that gallium-based conductors could be a solution to allow new form factors for more compliant wearable devices. In fact, one of the unique features of the technology is the ability to interconnect standard solid-state components into robust stretchable circuits. We set out a spin-off project (Feeltronix), which mission is to commercialize products build upon our proprietary technology platform to stretch the mechanical limits of electronics.







# Appendix

## A.1 Detailed fabrication methods

### A.1.1 Micro-cracked gold thin films deposition on PDMS

PDMS (Sylgard 184, Dow Corning) was mixed with its curing agent in a 10:1 mass ratio. A first layer of PDMS was spin-coated on a silicon wafer at 150 rpm for 1 min and cured for 2 h at 80 °C to form a 700 μm membrane. The support substrate (glass, silicon or PDMS) was then activated for 30 s in an oxygen plasma (Plasma Cleaner, Harrick), and subsequently coated with a release layer of either poly(styrene-4-sulfonate) (PSS) or trichloro(1H,1H,2H,2H-perfluorooctyl)silane (Sigma-Aldrich). In the case of the PSS release layer, PSS was spin coated for 1 min at 1000 rpm. In the case of silane release layer, a monolayer was self-assembled by evaporating the silane under weak vacuum in a desiccator.

Finally, a second layer of PDMS was spin-coated at 500 rpm for 1 min and cured for 2 h at 80 °C to form a 120 μm layer. The next step consisted in aligning the poly(imide) mask (Kapton, Dow Corning) to define conductive tracks. Bi-layers of Cr/Au were then thermally evaporated (Auto 306, Edwards) at a rate of 0.3 Å s<sup>-1</sup> for Cr and 1.0 Å s<sup>-1</sup> for Au. The thickness of Cr was fixed to 5 nm while the thickness of Au was varied between 13 nm and 60 nm. After thermal evaporation, the shadow masks were peeled-off from the PDMS surface.

In the case of the PSS release layer, the wafers were entirely dipped into deionized water for 30 min to dissolve the PSS layer and release the samples. In the case of the silane release layer, samples were cut and manually peeled off the support substrate.

### A.1.2 EGaIn wires micro-plotting

Fast and direct writing of microwires of EGaIn is performed by dispensing in a continuous flow small amount of EGaIn (99.99 %, Sigma Aldrich), preliminarily loaded in a syringe mounted on a computer-controlled three-axis XYZ micro-positioner stage (GX-II Microplotter, Sonoplot). The soft metal wires are plotted directly on a PDMS membrane spun and cured on silicon carrier wafer. The inner diameter of the syringe tip was 360 μm. The pressure inside the

---

syringe reservoir was maintained in the 1–5 kPa range using a fluid dispenser (TS250, OK International) to force the liquid to reach the end of the syringe's tip without forming a droplet. The tip was put in contact with the substrate and then slightly raised vertically (20  $\mu\text{m}$  to 80  $\mu\text{m}$  above the substrate) in order to form a liquid metal meniscus. Next, the tip was moved in the horizontal plane at 200  $\mu\text{m s}^{-1}$ , allowing the liquid metal to flow on the substrate and form wires. Silver wires were put into contact with the terminals of the liquid metal wires and a small drop of curable silver paste or EGaIn was put on top of the contact point to enhance the electrical connection. The contact area was subsequently encapsulated using silicone sealant (732, Dow Corning). Thanks to the good adhesion between the oxide skin that forms around the wires and the PDMS substrate, patterns composed of microwires were encapsulated by spin-coating uncured PDMS at 250 rpm. Finally, the encapsulation layer was cured at 60  $^{\circ}\text{C}$  for 12 hours and the devices were cut and peeled off the support wafer. The total thickness of the integrated devices was below 500  $\mu\text{m}$ .

### A.1.3 Biphasic gallium based thin film deposition and patterning

#### Film deposition

First, 100 mm silicon or float glass wafers were exposed to oxygen plasma (Harrick Plasma cleaner, 200 mTorr, 29 W, 30 s) then coated with a self-assembled layer of trichloro(1H,1H,2H,2H-perfluorooctyl)silane (Sigma Aldrich) in a dessicator. Polydimethylsiloxane (PDMS, Sylgard 184, Dow Corning, mixed at 10:1, w:w, prepolymer:cross-linker) was then spin-coated on the Si wafers (500 rpm for 1 min) and cured at 80  $^{\circ}\text{C}$  for at least two hours in a convection oven. Shadow mask (Kapton, DuPont) patterned with the negative of the conductor layout was laminated on the PDMS substrate. Alternatively, photoresist was deposited and patterned (see next section). 60 nm of gold was sputtered through the mask (DP 650 or AC 450, Alliance Concept). Next, a mass of pure gallium ranging from 0.1 g to 1 g was thermally evaporated (VACO 250, Vacotec or E300, Alliance Concept) on the gold-coated substrate (see Appendix A.3 page 121 for details on the calibration of the evaporator). After evaporation, the mask was removed from the substrate to reveal the desired pattern. We defined the parameter  $\beta$  as the atomic ratio ( $n_{\text{Ga}}/n_{\text{Au}}$ ) in the biphasic film. Before gallium evaporation,  $\beta = 0$ .

#### Lift-off patterning

The PDMS substrate was exposed to oxygen plasma (200 mTorr, 29 W, 30 s) then spincoated with photoresist (AZ-9260, MicroChemicals) at 6000 rpm for 90 s and left at room temperature for 12 h. The resist was then exposed with a 210  $\text{mJ cm}^{-2}$  dose (MJB4 mask aligner with 365 nm UV lamp, SUSS MicroTec), developed in diluted AZ-400-K (4:1 dionized water to developer volume ratio, MicroChemicals) and dried for 15 min at 60  $^{\circ}\text{C}$  on a hot plate. 40 nm of gold was sputtered to form an alloying layer and then 0.2 g of gallium was thermally evaporated. Lift-off was performed in a bath of SVC-14 (Shipley) for 24 h, followed by drying at 60  $^{\circ}\text{C}$  on a hot plate

for 15 min.

---

## A.2 Four-point probe measurement of micro-plotted EGaIn wire

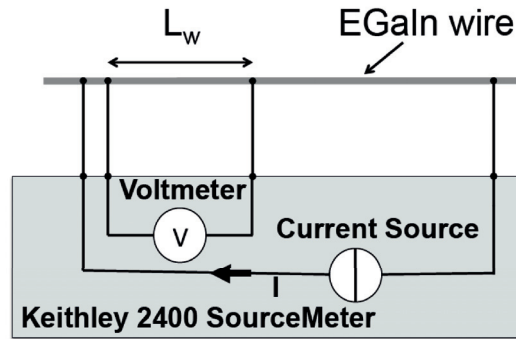


Figure A.1 – Set-up for the measurement of 4-wire resistance.  $L_w$  is the length of the section of the wire under measurement. The EGaIn wire was probed using solid Au wires.

### **A.3 Calibration of the gallium thermal evaporator**

As displayed in Figure A.2, the mass of gallium deposited per wafer was measured as a function of the gallium mass introduced in the thermal evaporator crucible using a precision scale (PB303-L, Mettler Toledo), and  $\beta$  was derived from the mass of sputtered gold ( $8.7 \pm 0.5$  mg per wafer for a 60 nm Au layer, mean  $\pm$  s.d.,  $n = 3$ ).

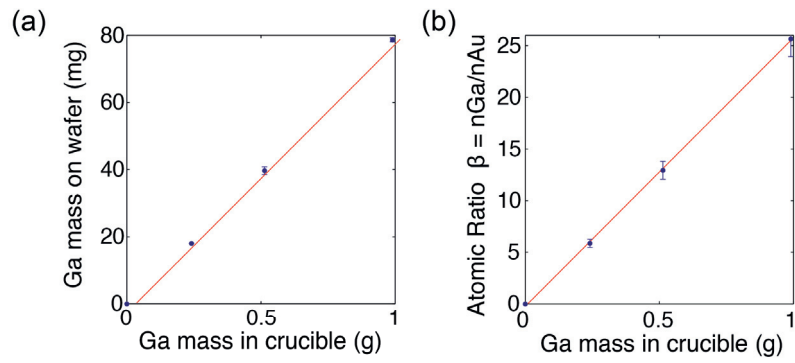


Figure A.2 – Calibration of gallium thermal evaporation and computation of the Ga/Au atomic ratio  $\beta$ . a) Gallium mass on glass wafers coated with 60 nm of sputtered gold as a function of gallium mass introduced in the crucible of the thermal evaporator. ( $n = 3$  for each point, error bars: S.D.). b) Corresponding Ga/Au atomic ratio  $\beta$ . Red lines represent linear fit.



#### A.4 Methodology and additional data for determination of biphasic film thickness

The image processing routine implemented in Matlab (Mathworks) is illustrated Figure A.3. Figure A.4 presents additional data collected using white light interferometry (ContourGT-K, Bruker) to compute the thickness of the biphasic films in the flat regions (without bulges). Lateral resolution was one pixel per micron in x and y direction.

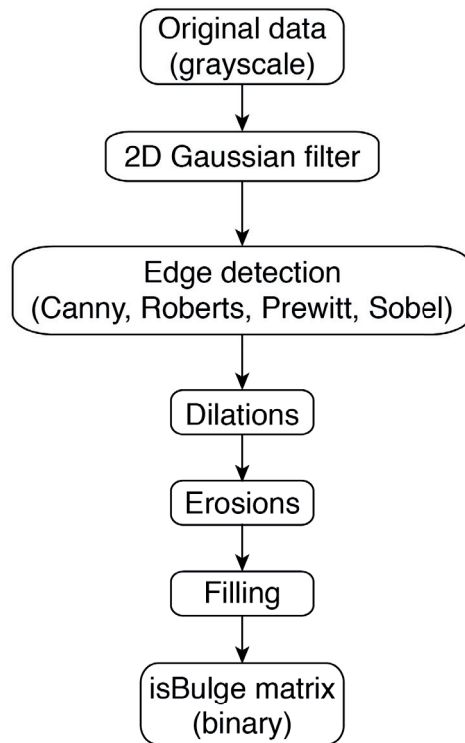


Figure A.3 – Image processing method for bulges detection in biphasic thin films.

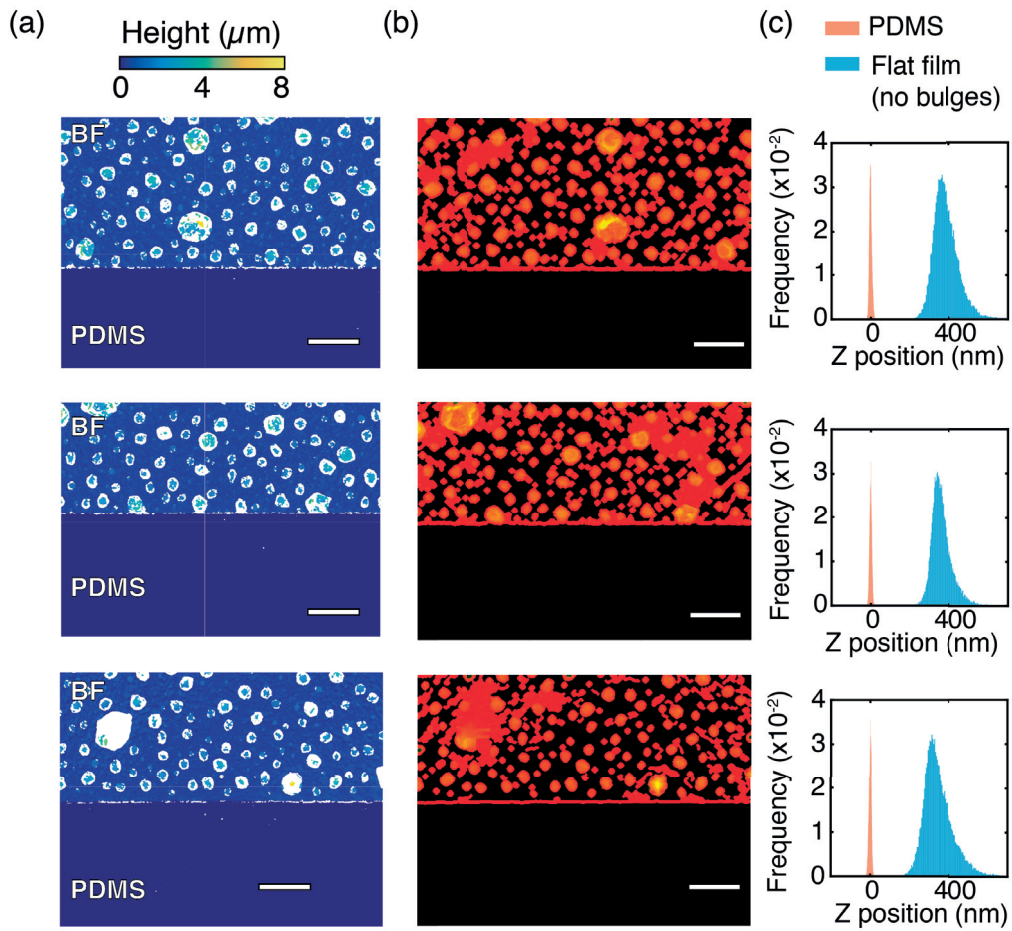


Figure A.4 – Determination of biphasic film thickness at  $\beta = 13$ . a) Topographic images of three zones from white light interferometry measurements. White pixels indicate that no data could be collected due to large slopes. Scale bars are 100  $\mu\text{m}$ . b) Bulges are identified in red on corresponding images. Scale bars are 100  $\mu\text{m}$ . c) Corresponding histograms of PDMS zones topography (red) and biphasic flat film regions (without bulges) topography (blue).

### A.5 Additional plot for electromigration study in biphasic films

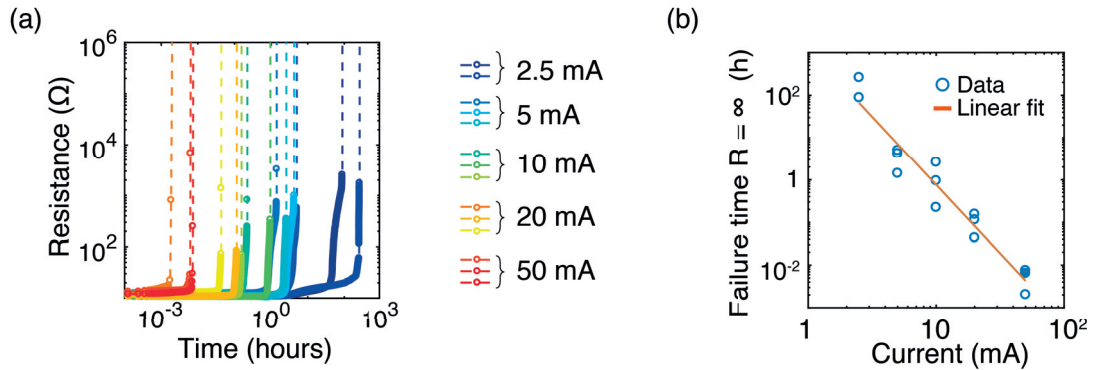


Figure A.5 – a) Resistance of samples as a function of time for DC currents of 2.5 mA to 50 mA. b) Failure time (define as the time when the open circuit condition was reached) as a function of DC current amplitude for the 14 tested samples. Exponent  $n = 3.2$  and  $R^2 = 0.94$  for linear fit.

---

## A.6 Calculation of joints' angles using the camera tracking system

The angle of the MCP joint was derived from the position of the markers identified in Figure 3.14 page 83. We applied the following method to compute the angular position of the finger from the 3D spatial position of the markers. We started by projecting the points  $M_{CMC2}$ ,  $M_{MCP2}$  and  $M_{PIP2}$  on the plane orthogonal to the plane containing  $M_{CMC2}$ ,  $M_{MCP2}$  and  $M_{MCP3}$  and itself containing  $M_{MCP3}$ . The intermediate angle value  $\theta_{MCP}^* \in [0; \pi]$  was computed as:

$$\theta_{MCP}^* = atan2(|\mathbf{P}_{MCP2}\mathbf{P}_{CM2} \times \mathbf{P}_{MCP2}\mathbf{P}_{PIP2}|, \mathbf{P}_{MCP2}\mathbf{P}_{CM2} \cdot \mathbf{P}_{MCP2}\mathbf{P}_{PIP2}) \quad (1)$$

where  $atan2$  is the four quadrant inverse tangent and points P are the projection of the corresponding points M having the same index.

Finally, we computed  $\theta_{MCP} \in [0; 2\pi]$  by looking at the sign of the dot product of the vector  $\mathbf{P}_{MCP2}\mathbf{P}_{CM2}$  with the vector  $\mathbf{n}_1$  orthogonal to the plane containing  $M_{CMC2}$ ,  $M_{MCP2}$  and  $M_{MCP3}$ , and itself containing  $M_{MCP3}$ :

$$\theta_{MCP} = \begin{cases} \theta_{MCP}^*, & \text{if } \mathbf{P}_{MCP2}\mathbf{P}_{CM2} \cdot \mathbf{n}_1 \leq 0 \\ 2\pi - \theta_{MCP}^*, & \text{if } \mathbf{P}_{MCP2}\mathbf{P}_{CM2} \cdot \mathbf{n}_1 > 0 \end{cases} \quad (2)$$

The same scheme was applied to compute  $\theta_{PIP}$ , this time using the plane containing  $M_{CMC3}$ ,  $M_{MCP2}$ , and  $M_{PIP2}$  as a reference for the projection and final determination of the angle.

## **A.7 Determination of orientation angle $\Phi_1$ from angle $\theta$ in the rosette configuration**

$\Phi_1$  is calculated from  $\theta$  using the following algorithm [174]:

- if  $e_A > e_C$  then  $\Phi_1 = -\theta$ .
- if  $e_A < e_C$  then  $\Phi_1 = -\theta + 90^\circ$ .
- if  $e_A = e_C$  and  $e_B < e_A$  then  $\Phi_1 = 45^\circ$ .
- if  $e_A = e_C$  and  $e_B > e_A$  then  $\Phi_1 = -45^\circ$ .
- if  $e_A = e_B = e_C$  then  $\Phi_1$  is indeterminate.

---

## A.8 Thermal coefficient of resistance (TCR) of the biphasic thin films

Biphasic gold-gallium thin film conductors ( $\beta = 6.5$ ) were prepared and clamped in the uni-axial stretcher. Electrical resistance and current running through of the conductor were measured using a 4-point probes method (2400 source-meter, Keithley) and acquired synchronously at 3.8 Hz on a computer running a custom LabVIEW program. In parallel, a thermal camera (A325 sc, FLIR systems) and close up lens ( $1 \times 25 \mu\text{m}$ , FLIR systems) were used to monitor synchronously the temperature at the surface of the samples (sampling rate: 5.6 Hz).

A current of 70 mA was passed through the tracks and the temperature of the track was varied by convective cooling. The TCR  $\alpha$  was determined linear fit Figure A.6, according to the equation  $R(T) = R_0(1 + \alpha(T - T_0))$  where  $R_0$  is the resistance at room temperature  $T_0$ .

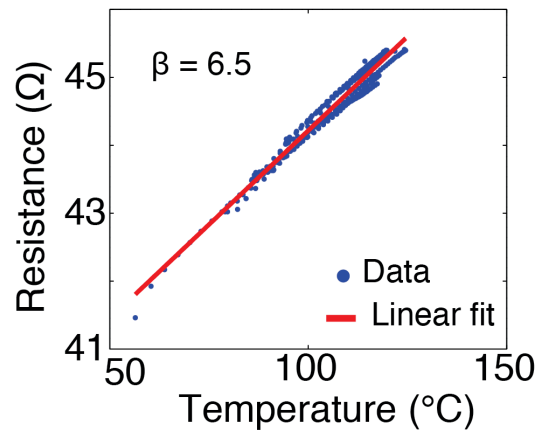


Figure A.6 – Resistance of a self-heated biphasic gold-gallium track as function of temperature of the track. The temperature coefficient of resistance ( $1.43 \times 10^{-3} \text{ K}^{-1}$ ) was computed from linear regression.

# Bibliography

- [1] N. Magnenat-Thalmann, P. Kalra, J. L. Lévêque, R. Bazin, D. Batische, and B. Querleux. A computational skin model: Fold and wrinkle formation. *IEEE Transactions on Information Technology in Biomedicine*, 6(4):317–323, 2002.
- [2] A. Annaidh, M. Ottenio, and K. Bruyère. Mechanical properties of excised human skin. In *6th World Congress of Biomechanics*, 2010.
- [3] A. N. Annaidh, K. Bruyere, M. Destrade, M. D. Gilchrist, and M. Ottenio. Characterising the Anisotropic Mechanical Properties of Excised Human Skin. *ArXiv e-prints*, 2013.
- [4] X. Chen. Making Electrodes Stretchable. *Small Methods*, page 1600029, 2017.
- [5] C. T. McKee, J. a. Last, P. Russell, and C. J. Murphy. Indentation versus tensile measurements of Young’s modulus for soft biological tissues. *Tissue engineering. Part B, Reviews*, 17(3):155–164, 2011.
- [6] S. P. Lacour, G. Courtine, and J. Guck. Materials and technologies for soft implantable neuroprostheses. *Nature Reviews*, 1:16063, 2016.
- [7] V. E. Abraira and D. D. Ginty. The sensory neurons of touch. *Neuron*, 79(4):618–39, 2013.
- [8] A. Patapoutian, A. M. Peier, G. M. Story, and V. Viswanath. ThermoTRP channels and beyond: mechanisms of temperature sensation. *Nature Reviews Neuroscience*, 4(7):529–39, 2003.
- [9] R. Johansson and Å. Vallbo. Tactile sensibility in the human hand: relative and absolute densities of four types of mechanoreceptive units in glabrous skin. *Journal of Physiology*, 286:283–300, 1979.
- [10] E. R. Kandel, J. H. Schwartz, and T. M. Jessell. *Principles of Neural Science*. McGraw-Hill, 2000.
- [11] R. Balasubramanian and V. J. Santos (Eds). *The human hand as an inspiration for robot hand development*, volume 95. Springer, 2014.
- [12] R. Dahiya, G. Metta, M. Valle, and G. Sandini. Tactile Sensing—From Humans to Humanoids. *IEEE Transactions on Robotics*, 26(1):1–20, 2010.

## Bibliography

---

- [13] A. Chortos, J. Liu, and Z. Bao. Pursuing prosthetic electronic skin. *Nature Materials*, 15:937–950, 2016.
- [14] A. Prochazka. Proprioceptive feedback and movement regulation. *Comprehensive Physiology*, 2010.
- [15] M. L. Hammock, A. Chortos, B. C.-K. Tee, J. B.-H. Tok, and Z. Bao. 25th Anniversary Article: The Evolution of Electronic Skin (E-Skin): A Brief History, Design Considerations, and Recent Progress. *Advanced Materials*, 25(42):5997–6038, 2013.
- [16] V. Lumelsky, M. Shur, and S. Wagner. Sensitive skin. *IEEE Sensors Journal*, 1(1):41–51, 2001.
- [17] G. H. Gelinck, H. E. a. Huitema, E. van Veenendaal, E. Cantatore, L. Schrijnemakers, J. B. P. H. van der Putten, T. C. T. Geuns, M. Beenhakkers, J. B. Giesbers, B.-H. Huisman, E. J. Meijer, E. M. Benito, F. J. Touwslager, A. W. Marsman, B. J. E. van Rens, and D. M. de Leeuw. Flexible active-matrix displays and shift registers based on solution-processed organic transistors. *Nature Materials*, 3(2):106–110, 2004.
- [18] T. Someya. *Stretchable electronics*. John Wiley & Sons, 2012.
- [19] R. S. Dahiya and M. Valle. *Robotic Tactile Sensing*. Springer Netherlands, Dordrecht, 2013.
- [20] S. Bauer, S. Bauer-Gogonea, I. Graz, M. Kaltenbrunner, C. Keplinger, and R. Schwödi-a-uer. 25th Anniversary Article: A Soft Future: From Robots and Sensor Skin to Energy Harvesters. *Advanced Materials*, 26(1):149–162, 2014.
- [21] M. McEvoy and N. Correll. Materials that couple sensing, actuation, computation, and communication. *Science*, 347(6228), 2015.
- [22] X. Wang, L. Dong, H. Zhang, R. Yu, C. Pan, and Z. L. Wang. Recent Progress in Electronic Skin. *Advanced Science*, 2:1500169, 2015.
- [23] T. Someya, Z. Bao, and G. G. Malliaras. The rise of plastic bioelectronics. *Nature*, 50:379–385, 2016.
- [24] J. A. Rogers, R. Ghaffari, and D.-H. Kim (eds.). *Stretchable Bioelectronics for Medical Devices and Systems*. Springer International Publishing, 2016.
- [25] C. G. Núñez, W. T. Navaraj, E. O. Polat, and R. Dahiya. Energy-Autonomous, Flexible, and Transparent Tactile Skin. *Advanced Functional Materials*, 2017.
- [26] R. A. Bilodeau, E. L. White, and R. K. Kramer. Monolithic Fabrication of Sensors and Actuators in a Soft Robotic Gripper. In *2015 IEEE/RSJ International Conference on Intelligent Robots and Systems (IROS)*, pages 2324–2329, Hamburg, Germany, 2015.



- [27] R. C. Webb, R. M. Pielak, P. Bastien, J. Ayers, J. Niittynen, J. Kurniawan, M. Manco, A. Lin, N. H. Cho, V. Malyrchuk, G. Balooch, and J. a. Rogers. Thermal Transport Characteristics of Human Skin Measured In Vivo Using Ultrathin Conformal Arrays of Thermal Sensors and Actuators. *Plos One*, 10(2):e0118131, 2015.
- [28] F. Hammond, Y. Mengüç, and R. J. Wood. Toward a modular soft sensor-embedded glove for human hand motion and tactile pressure measurement. In *2013 IEEE/RSJ Intelligent Robots and Systems (IROS)*, pages 4000–4007, 2014.
- [29] D.-H. Kim and J. a. Rogers. Stretchable Electronics: Materials Strategies and Devices. *Advanced Materials*, 20(24):4887–4892, 2008.
- [30] S. Wagner and S. Bauer. Materials for stretchable electronics. *MRS Bulletin*, 37(03):207–213, 2012.
- [31] J. a. Rogers, T. Someya, and Y. Huang. Materials and mechanics for stretchable electronics. *Science*, 327:1603–1607, 2010.
- [32] W. S. Wong and A. Salleo. *Flexible electronics: materials and applications*, volume 11. Springer Science & Business Media, 2009.
- [33] D. Qi, Z. Liu, W. R. Leow, and X. Chen. Elastic substrates for stretchable devices. *MRS Bulletin*, 42(02):103–107, 2017.
- [34] J.-Y. Sun, C. Keplinger, G. M. Whitesides, and Z. Suo. Ionic skin. *Advanced Materials*, 26(25):7608–7614, 2014.
- [35] A. C. M. Kuo. Poly (dimethylsiloxane). In J. E. Mark, editor, *Polymer Data Handbook*, pages 411–435. Oxford University Press, 1999.
- [36] S. Bhattacharya, A. Datta, J. Berg, and S. Gangopadhyay. Studies on Surface Wettability of Poly(Dimethyl)Siloxane ( PDMS ) and Glass Under Oxygen-Plasma. *Journal of Microelectromechanical Systems*, 14(3):590–597, 2005.
- [37] M. Zhang, J. Wu, L. Wang, K. Xiao, and W. Wen. A simple method for fabricating multi-layer pdms structures for 3d microfluidic chips. *Lab on a Chip*, 10(9):1199–1203, 2010.
- [38] T. Adrega and S. P. Lacour. Stretchable gold conductors embedded in PDMS and patterned by photolithography: fabrication and electromechanical characterization. *Journal of Micromechanics and Microengineering*, 20(5):055025, 2010.
- [39] A. Oláh, H. Hillborg, and G. J. Vancso. Hydrophobic recovery of UV/ozone treated poly(dimethylsiloxane): Adhesion studies by contact mechanics and mechanism of surface modification. *Applied Surface Science*, 239(3-4):410–423, 2005.
- [40] E. Verneuil, A. Buguin, and P. Silberzan. Permeation-induced flows: Consequences for silicone-based microfluidics. *Europhysics Letters*, 68(3):412–418, 2004.

## Bibliography

---

- [41] J. N. Lee, C. Park, and G. M. Whitesides. Solvent compatibility of poly(dimethylsiloxane)-based microfluidic devices. *Analytical chemistry*, 75(23):6544–54, 2003.
- [42] I. D. Johnston, D. K. McCluskey, C. K. L. Tan, and M. C. Tracey. Mechanical characterization of bulk Sylgard 184 for microfluidics and microengineering. *Journal of Micromechanics and Microengineering*, 24(3):035017, 2014.
- [43] Dow Corning Corporation. Sylgard 184 Silicone Elastomer Data Sheet, 1998.
- [44] M. Y. Teo, N. Kim, S. Kee, B. S. Kim, G. Kim, S. Hong, S. Jung, and K. Lee. Highly Stretchable and Highly Conductive PEDOT:PSS/Ionic Liquid Composite Transparent Electrodes for Solution-Processed Stretchable Electronics. *ACS Applied Materials & Interfaces*, page acsami.6b11988, 2016.
- [45] X. Yu, B. Mahajan, W. Shou, and H. Pan. Materials, Mechanics, and Patterning Techniques for Elastomer-Based Stretchable Conductors. *Micromachines*, 8(1):7, 2016.
- [46] T. Q. Trung and N.-e. Lee. Recent Progress on Stretchable Electronic Devices with Intrinsically Stretchable Components. *Advanced Materials*, pages 1–29, 2016.
- [47] Y. Qian, X. Zhang, L. Xie, D. Qi, and B. K. Chandran. Stretchable Organic Semiconductor Devices. *Advanced Materials*, 2016.
- [48] D. McCoul, W. Hu, M. Gao, V. Mehta, and Q. Pei. Recent Advances in Stretchable and Transparent Electronic Materials. *Advanced Electronic Materials*, 201500407(2):n/a–n/a, 2016.
- [49] J.-H. So, J. Thelen, A. Qusba, G. J. Hayes, G. Lazzi, and M. D. Dickey. Reversibly Deformable and Mechanically Tunable Fluidic Antennas. *Advanced Functional Materials*, 19(22):3632–3637, 2009.
- [50] M. D. Dickey. Stretchable and Soft Electronics using Liquid Metals. *Advanced Materials*, 2017.
- [51] T. Hansen, K. West, O. Hassager, and N. Larsen. Highly Stretchable and Conductive Polymer Material Made from Poly(3,4-ethylenedioxythiophene) and Polyurethane Elastomers. *Advanced Functional Materials*, 17(16):3069–3073, 2007.
- [52] Y. Wang, C. Zhu, R. Pfattner, H. Yan, S. Chen, F. Molina-Lopez, F. Lissel, J. Liu, N. Rabiah, Z. Chen, J. W. Chung, C. Linder, M. Toney, B. Murmann, and Z. Bao. A highly stretchable, transparent and conductive polymer. *Science Advances*, 3(March):e1602076, 2017.
- [53] M. Park, J. Park, and U. Jeong. Design of conductive composite elastomers for stretchable electronics. *Nano Today*, 9(2):244–260, 2014.
- [54] S. Rosset, M. Niklaus, P. Dubois, and H. R. Shea. Metal Ion Implantation for the Fabrication of Stretchable Electrodes on Elastomers. *Advanced Functional Materials*, 19(3):470–478, 2009.

- 
- [55] F. Xu and Y. Zhu. Highly conductive and stretchable silver nanowire conductors. *Advanced Materials*, 24(37):5117–22, 2012.
- [56] A. Larmagnac, S. Eggenberger, H. Janossy, and J. Vörös. Stretchable electronics based on Ag-PDMS composites. *Scientific reports*, 4:7254, 2014.
- [57] T. Sekitani, Y. Noguchi, K. Hata, T. Fukushima, T. Aida, and T. Someya. A Rubberlike Stretchable Active Matrix Using Elastic Conductors. *Science*, 321:1468–1472, 2008.
- [58] S. P. Lacour, D. Chan, S. Wagner, T. Li, and Z. Suo. Mechanisms of reversible stretchability of thin metal films on elastomeric substrates. *Applied Physics Letters*, 88(20):204103, 2006.
- [59] C. F. Guo, T. Sun, Q. Liu, Z. Suo, and Z. Ren. Highly stretchable and transparent nanomesh electrodes made by grain boundary lithography. *Nature communications*, 5:3121, 2014.
- [60] S. P. Lacour, J. Jones, Z. Suo, and S. Wagner. Design and Performance of Thin Metal Film Interconnects for Skin-Like Electronic Circuits. *IEEE Electron Device Letters*, 25(4):179–181, 2004.
- [61] D.-Y. Khang, H. Jiang, Y. Huang, and J. A. Rogers. A Stretchable Form of Single-Crystal Silicon for High-Performance Electronics on Rubber Substrates. *Science*, 311(January):208–213, 2006.
- [62] M. Kaltenbrunner, T. Sekitani, J. Reeder, T. Yokota, K. Kuribara, T. Tokuhara, M. Drack, R. Schwödiauer, I. Graz, S. Bauer-Gogonea, S. Bauer, and T. Someya. An ultra-lightweight design for imperceptible plastic electronics. *Nature*, 499(7459):458–63, 2013.
- [63] F. Axisa, F. Bossuyt, T. Vervust, and J. Vanfleteren. Laser based fast prototyping methodology of producing stretchable and conformable electronic systems. In *2nd Electronics System Integration Technology Conference*, pages 1387–1390, 2008.
- [64] S. Xu, Y. Zhang, L. Jia, K. E. Mathewson, K.-I. Jang, J. Kim, H. Fu, X. Huang, P. Chava, R. Wang, S. Bhole, L. Wang, Y. J. Na, Y. Guan, M. Flavin, Z. Han, Y. Huang, and J. a. Rogers. Soft microfluidic assemblies of sensors, circuits, and radios for the skin. *Science*, 344(6179):70–74, 2014.
- [65] T. C. Shyu, P. F. Damasceno, P. M. Dodd, A. Lamoureux, L. Xu, M. Shlian, M. Shtein, S. C. Glotzer, and N. a. Kotov. A kirigami approach to engineering elasticity in nanocomposites through patterned defects. *Nature Materials*, 14(8):785–789, 2015.
- [66] Y. Cao, T. G. Morrissey, E. Acome, S. I. Allec, B. M. Wong, C. Keplinger, and C. Wang. A Transparent, Self-Healing, Highly Stretchable Ionic Conductor. *Advanced Materials*, 29(10):1605099, 2016.
- [67] C. Keplinger, J. Sun, and C. Foo. Stretchable, Transparent, Ionic Conductors. *Science*, 2013.

## Bibliography

---

- [68] J.-B. Chossat, Y.-L. Park, R. J. Wood, and V. Duchaine. A Soft Strain Sensor Based on Ionic and Metal Liquids. *IEEE Sensors Journal*, 13(9):3405–3414, 2013.
- [69] Y. Zheng, Z. He, Y. Gao, and J. Liu. Direct desktop Printed-Circuits-on-Paper flexible electronics. *Scientific reports*, 3:1786, 2013.
- [70] S. P. Lacour, S. Wagner, and Z. Suo. Stretchable conductors: thin gold films on silicone elastomer. *MRS Proceedings*, 795, 2003.
- [71] W. H. Yeo, Y. S. Kim, J. Lee, A. Ameen, L. Shi, M. Li, S. Wang, R. Ma, S. H. Jin, Z. Kang, Y. Huang, and J. A. Rogers. Multifunctional epidermal electronics printed directly onto the skin. *Advanced Materials*, 25(20):2773–2778, 2013.
- [72] I. M. Graz, D. P. J. Cotton, and S. P. Lacour. Extended cyclic uniaxial loading of stretchable gold thin-films on elastomeric substrates. *Applied Physics Letters*, 94(7):071902, 2009.
- [73] F. Bossuyt, J. Guenther, T. Löher, M. Seckel, T. Sterken, and J. De Vries. Cyclic endurance reliability of stretchable electronic substrates. *Microelectronics Reliability*, 51(3):628–635, 2011.
- [74] N. Matsuhisa, M. Kaltenbrunner, T. Yokota, H. Jinno, K. Kuribara, T. Sekitani, and T. Someya. Printable elastic conductors with a high conductivity for electronic textile applications. *Nature Communications*, 6(May):7461, 2015.
- [75] K. Tybrandt, F. Stauffer, and J. Vörös. Multilayer Patterning of High Resolution Intrinsically Stretchable Electronics. *Scientific Reports*, pages 1–14, 2016.
- [76] S. W. Jin, J. Park, S. Y. Hong, H. Park, Y. R. Jeong, J. Park, S.-S. Lee, and J. S. Ha. Stretchable Loudspeaker using Liquid Metal Microchannel. *Scientific Reports*, 5(1):11695, 2015.
- [77] S. Zhu, J.-H. So, R. Mays, S. Desai, W. R. Barnes, B. Pourdeyhimi, and M. D. Dickey. Ultrastretchable Fibers with Metallic Conductivity Using a Liquid Metal Alloy Core. *Advanced Functional Materials*, 23(18):2308–2314, 2013.
- [78] S. H. E. E. Jeong. *Liquids Matter in Compliant Microsystems*. PhD thesis, Uppsala University, 2016.
- [79] A. Romeo and S. P. Lacour. Stretchable metal oxide thin film transistors on engineered substrate for electronic skin applications. In *Proceedings of the Annual International Conference of the IEEE Engineering in Medicine and Biology Society, EMBS*, pages 8014–8017, 2015.
- [80] I. R. Mineev, P. Musienko, A. Hirsch, Q. Barraud, N. Wenger, E. M. Moraud, J. Gandar, M. Capogrosso, T. Milekovic, L. Asboth, R. F. Torres, N. Vachicouras, Q. Liu, N. Pavlova, S. Duis, A. Larmagnac, J. Vörös, S. Micera, Z. Suo, G. Courtine, and S. P. Lacour. Electronic dura mater for long-term multimodal neural interfaces. *Science*, 347(6218):159–163, 2015.

- [81] S. Lacour, C. Tsay, and S. Wagner. An Elastically Stretchable TFT Circuit. *IEEE Electron Device Letters*, 25(12):792–794, 2004.
- [82] D. Cotton, I. Graz, and S. Lacour. A multifunctional capacitive sensor for stretchable electronic skins. *Sensors Journal, IEEE*, 9(12):2008–2009, 2009.
- [83] H. Vandeparre, D. Watson, and S. P. Lacour. Extremely robust and conformable capacitive pressure sensors based on flexible polyurethane foams and stretchable metallization. *Applied Physics Letters*, 103(20):204103, 2013.
- [84] A. P. Gerratt, N. Sommer, S. P. Lacour, and A. Billard. Stretchable capacitive tactile skin on humanoid robot fingers—First experiments and results. In *Humanoid Robots (Humanoids), 2014 14th IEEE-RAS International Conference on*, pages 238–245. IEEE, 2014.
- [85] K. M. Musick, J. Rigosa, S. Narasimhan, S. Wurth, M. Capogrosso, D. J. Chew, J. W. Fawcett, S. Micera, and S. P. Lacour. Chronic multichannel neural recordings from soft regenerative microchannel electrodes during gait. *Scientific reports*, 5, 2015.
- [86] R. J. Whitney. The measurement of volume changes in human limbs. *Journal of Physiology*, 121:1–27, 1953.
- [87] M. D. Dickey, R. C. Chiechi, R. J. Larsen, E. a. Weiss, D. a. Weitz, and G. M. Whitesides. Eutectic Gallium-Indium (EGaIn): A Liquid Metal Alloy for the Formation of Stable Structures in Microchannels at Room Temperature. *Advanced Functional Materials*, 18(7):1097–1104, 2008.
- [88] R. K. Kramer, C. Majidi, and R. J. Wood. Masked Deposition of Gallium-Indium Alloys for Liquid-Embedded Elastomer Conductors. *Advanced Functional Materials*, 23(42):5292–5296, 2013.
- [89] D. Kim, J. H. Yoo, Y. Lee, W. Choi, K. Yoo, and J. B. J. Lee. Gallium-based liquid metal inkjet printing. In *Proceedings of the IEEE International Conference on Micro Electro Mechanical Systems (MEMS)*, pages 967–970, 2014.
- [90] M. A. H. Khondoker and D. Sameoto. Fabrication methods and applications of microstructured gallium based liquid metal alloys. *Smart Materials and Structures*, 25(9):093001, 2016.
- [91] M. D. Dickey. Liquid Metals for Soft and Stretchable Electronics. In J. A. Rogers, R. Ghafari, and D.-H. Kim, editors, *Stretchable Bioelectronics for Medical Devices and Systems*, pages 3–30. Springer International Publishing, 2016.
- [92] I. D. Joshipura, H. R. Ayers, C. Majidi, and M. D. Dickey. Methods to pattern liquid metals. *J. Mater. Chem. C*, 3:3834–3841, 2015.

## Bibliography

---

- [93] C. Alcock, V. P. Itkin, and M. K. Horrigan. Vapour Pressure Equations for the Metallic Elements: 298–2500K. *The Canadian Journal of Metallurgy and Materials Science*, 23(3):309–313, 1984.
- [94] G. Kwakkel, B. J. Kollen, J. van der Grond, and A. J. Prevo. Probability of regaining dexterity in the flaccid upper limb. *Stroke*, 34(9):2181–2186, 2003.
- [95] M. Rizzo, O. Hadjimichael, J. Preiningerova, and T. Vollmer. Prevalence and treatment of spasticity reported by multiple sclerosis patients. *Multiple Sclerosis Journal*, 10(5):589–595, 2004.
- [96] E. Biddiss and T. Chau. Upper-limb prosthetics: critical factors in device abandonment. *American journal of physical medicine & rehabilitation / Association of Academic Physiatrists*, 86(12):977–987, 2007.
- [97] S. Furuya, M. Flanders, and J. E. Soechting. Hand kinematics of piano playing. *Journal of Neurophysiology*, 106(6):2849–2864, 2011.
- [98] M.-C. Hepp-Reymond, V. Chakarov, J. Schulte-Mönting, F. Huethe, and R. Kristeva. Role of proprioception and vision in handwriting. *Brain Research Bulletin*, 79(6):365–70, 2009.
- [99] R. W. Young. Evolution of the human hand : the role of throwing and clubbing. *Journal of Anatomy*, 202(1):165–174, 2003.
- [100] H. Zhou and H. Hu. Human motion tracking for rehabilitation-A survey. *Biomedical Signal Processing and Control*, 3(1):1–18, 2008.
- [101] H. Zhou, T. Stone, H. Hu, and N. Harris. Use of multiple wearable inertial sensors in upper limb motion tracking. *Medical engineering & physics*, 30(1):123–133, 2008.
- [102] C.-y. P. C.-y. Park, J.-h. B. J.-h. Bae, and I. M. I. Moon. Development of wireless data glove for unrestricted upper-extremity rehabilitation system. In *ICROS-SICE International Joint Conference 2009*, pages 790–793, Fukuoka, Japan, 2009.
- [103] H. Chen, Q. Wang, and L. Cao. Design of the workstation for hand rehabilitation based on data glove. In *2010 IEEE International Conference on Bioinformatics and Biomedicine Workshops, BIBMW 2010*, pages 769–771, 2010.
- [104] A. Buryanov and V. Kotiuk. Proportions of Hand Segments. *International Journal of Morphology*, 28(3):755–758, 2010.
- [105] F. Lorussi, N. Carbonaro, D. De Rossi, and A. Tognetti. Strain- and angular-sensing fabrics for human motion analysis in daily life. In S. Schneegass and O. Amft, editors, *Smart Textiles: Fundamentals, Design, and Interaction*, pages 49–70. Springer International Publishing, Cham, 2017.

- 
- [106] M. Amjadi, K.-U. Kyung, I. Park, and M. Sitti. Stretchable, Skin-Mountable, and Wearable Strain Sensors and Their Potential Applications: A Review. *Advanced Functional Materials*, 26(11):1678–1698, 2016.
- [107] H. Jin, Y. S. Abu-Raya, and H. Haick. Advanced Materials for Health Monitoring with Skin-Based Wearable Devices. *Advanced Healthcare Materials*, page 1700024, 2017.
- [108] J. T. Muth, D. M. Vogt, R. L. Truby, Y. Mengüç, D. B. Kolesky, R. J. Wood, and J. a. Lewis. Embedded 3D Printing of Strain Sensors within Highly Stretchable Elastomers. *Advanced Materials*, 26:6307–6312, 2014.
- [109] Y.-L. Park, B.-R. Chen, and R. J. Wood. Design and Fabrication of Soft Artificial Skin Using Embedded Microchannels and Liquid Conductors. *IEEE Sensors Journal*, 12(8):2711–2718, 2012.
- [110] R. K. Kramer, C. Majidi, R. Sahai, and R. J. Wood. Soft curvature sensors for joint angle proprioception. In *2011 IEEE/RSJ International Conference on Intelligent Robots and Systems (IROS)*, pages 1919–1926, 2011.
- [111] Y. Menguc, Y.-L. Park, H. Pei, D. Vogt, P. M. Aubin, E. Winchell, L. Fluke, L. Stirling, R. J. Wood, and C. J. Walsh. Wearable soft sensing suit for human gait measurement. *The International Journal of Robotics Research*, 2014.
- [112] N. Lu, C. Lu, S. Yang, and J. Rogers. Highly Sensitive Skin-Mountable Strain Gauges Based Entirely on Elastomers. *Advanced Functional Materials*, 22(19):4044–4050, 2012.
- [113] J.-b. Chossat, Y. Tao, V. Duchaine, and Y.-l. Park. Wearable Soft Artificial Skin for Hand Motion Detection with Embedded Microfluidic Strain Sensing. In *2015 IEEE International Conference on Robotics and Automation (ICRA)*, pages 2568–2573, 2015.
- [114] P. Polygerinos, Z. Wang, K. C. Galloway, R. J. Wood, and C. J. Walsh. Soft robotic glove for combined assistance and at-home rehabilitation. *Robotics and Autonomous Systems*, 73:135–143, 2014.
- [115] D. W. Tan, M. a. Schiefer, M. W. Keith, J. R. Anderson, J. Tyler, and D. J. Tyler. A neural interface provides long-term stable natural touch perception. *Science Translational Medicine*, 6(257), 2014.
- [116] S. Raspopovic, M. Capogrosso, F. M. Petrini, M. Bonizzato, J. Rigosa, G. Di Pino, J. Carpaneto, M. Controzzi, T. Boretius, E. Fernandez, G. Granata, C. M. Oddo, L. Citi, a. L. Ciancio, C. Cipriani, M. C. Carrozza, W. Jensen, E. Guglielmelli, T. Stieglitz, P. M. Rossini, and S. Micera. Restoring Natural Sensory Feedback in Real-Time Bidirectional Hand Prostheses. *Science Translational Medicine*, 6(222):222ra19–222ra19, 2014.
- [117] R. B. Hellman, E. Chang, J. Tanner, S. I. Helms Tillery, and V. J. Santos. A Robot Hand Testbed Designed for Enhancing Embodiment and Functional Neurorehabilitation of Body Schema in Subjects with Upper Limb Impairment or Loss. *Frontiers in Human Neuroscience*, 9(February):1–10, 2015.

## Bibliography

---

- [118] S. M. M. De Rossi, N. Vitiello, T. Lenzi, R. Ronsse, B. Koopman, A. Persichetti, F. Giovacchini, F. Vecchi, A. J. Ijspeert, H. Van Der Kooij, and M. C. Carrozza. Soft artificial tactile sensors for the measurement of human-robot interaction in the rehabilitation of the lower limb. *2010 Annual International Conference of the IEEE Engineering in Medicine and Biology Society, EMBC'10*, pages 1279–1282, 2010.
- [119] N. Sommer, M. Li, and A. Billard. Bimanual compliant tactile exploration for grasping unknown objects. In *Robotics and Automation (ICRA), 2014 IEEE International Conference on*, pages 6400–6407. IEEE, 2014.
- [120] D. Farina and O. Aszmann. Bionic Limbs : Clinical Reality and Academic Promises. *Science Translational Medicine*, 6(257), 2014.
- [121] M. Ying, A. P. Bonifas, N. Lu, Y. Su, R. Li, H. Cheng, A. Ameen, Y. Huang, and J. A. Rogers. Silicon nanomembranes for fingertip electronics. *Nanotechnology*, 23, 2012.
- [122] C.-L. Choong, M.-B. Shim, B.-S. Lee, S. Jeon, D.-S. Ko, T.-H. Kang, J. Bae, S. H. Lee, K.-E. Byun, J. Im, Y. J. Jeong, C. E. Park, J.-J. Park, and U.-I. Chung. Highly Stretchable Resistive Pressure Sensors Using a Conductive Elastomeric Composite on a Micropyramid Array. *Advanced Materials*, 26(21):1521–4095, 2014.
- [123] J. Kim, M. Lee, H. J. Shim, R. Ghaffari, H. R. Cho, D. Son, Y. H. Jung, M. Soh, C. Choi, S. Jung, K. Chu, D. Jeon, S.-T. Lee, J. H. Kim, S. H. Choi, T. Hyeon, and D.-H. Kim. Stretchable silicon nanoribbon electronics for skin prosthesis. *Nature Communications*, 5:5747, 2014.
- [124] H. O. Michaud, J. Teixidor, and S. P. Lacour. Soft metal constructs for large strain sensor membrane. *Smart Materials and Structures*, 24(3):35020, 2015.
- [125] A. Hirsch, H. O. Michaud, A. P. Gerratt, S. de Mulatier, and S. P. Lacour. Intrinsically Stretchable Biphasic(Solid–Liquid) Thin Metal Films. *Advanced Materials*, 28(22):4507–4512, 2016.
- [126] H. O. Michaud and S. P. Lacour. Liquid electromigration under dc current in biphasic thin metal films. *In preparation*, 2017.
- [127] O. Graudejus, P. Görrn, and S. Wagner. Controlling the morphology of gold films on poly(dimethylsiloxane). *ACS applied materials & interfaces*, 2(7):1927–33, 2010.
- [128] O. Graudejus, Z. Jia, T. Li, and S. Wagner. Size-Dependent Rupture Strain of Elastically Stretchable Metal Conductors. *Scripta materialia*, 66(11):919–922, 2012.
- [129] R. L. Parker and a. Krinsky. Electrical Resistance-Strain Characteristics of Thin Evaporated Metal Films. *Journal of Applied Physics*, 34(9):2700, 1963.
- [130] M. R. Neuman. Structural Dependence of Strain Gauge Effect and Surface Resistivity for Thin Gold Films. *Journal of Vacuum Science and Technology*, 6(4):710–713, 1969.



- 
- [131] R. B. Watson. Bonded electrical resistance strain gages. In W. N. Sharpe Jr and W. N. Sharpe, editors, *Springer handbook of experimental solid mechanics*, pages 283–333. Springer, 2008.
- [132] P. Görrn, W. Cao, and S. Wagner. Isotropically stretchable gold conductors on elastomeric substrates. *Soft Matter*, 7:7177–7180, 2011.
- [133] C. Ladd, J.-H. So, J. Muth, and M. D. Dickey. 3D Printing of Free Standing Liquid Metal Microstructures. *Advanced Materials*, 25(36):5081–5, 2013.
- [134] J. W. Boley, E. L. White, G. T.-C. Chiu, and R. K. Kramer. Direct Writing of Gallium-Indium Alloy for Stretchable Electronics. *Advanced Functional Materials*, 24(23):3501–3507, 2014.
- [135] Keithley Instruments Inc. Series 2400 SourceMeter Specifications, 2011.
- [136] D. Zrnic and D. Swatik. On the resistivity and surface tension of the eutectic alloy of gallium and indium. *Journal of Less-Common Metals*, 18:67–68, 1969.
- [137] C. Majidi, R. Kramer, and R. J. Wood. A non-differential elastomer curvature sensor for softer-than-skin electronics. *Smart Materials and Structures*, 20(10):105017, 2011.
- [138] H.-J. Kim. *Stretchable Interconnects Using Room Temperature Liquid Alloy on Elastomeric Substrate*. PhD thesis, Purdue University, 2007.
- [139] V. Simić and Ž. Marinković. Thin film interdiffusion of Au and Ga at room temperature. *Thin Solid Films*, 34(1):179–183, 1976.
- [140] N. Bowden, S. Brittain, and A. Evans. Spontaneous formation of ordered structures in thin films of metals supported on an elastomeric polymer. *Nature*, 393(May):146–149, 1998.
- [141] R. P. Elliott and F. A. Shunk. The Au-Ga (Gold-Gallium) System. *Bulletin of Alloy Phase Diagrams*, 2(3):356–358, 1981.
- [142] D. G. Carlson, J. Feder, and A. Segmüller. Measurement of the liquid-structure factor of supercooled gallium and mercury. *Physical Review A*, 9(1):400–403, 1974.
- [143] M. G. Nicholas and C. F. Old. Liquid metal embrittlement. *Journal of Materials Science*, 14(1):1–18, 1979.
- [144] K. T. Lee, Y. S. Jung, T. Kim, C. H. Kim, J. H. Kim, J. Y. Kwon, and S. M. Oh. Liquid Gallium Electrode Confined in Porous Carbon Matrix as Anode for Lithium Secondary Batteries. *Electrochemical and Solid-State Letters*, 11:A21, 2008.
- [145] C. A. Schneider, W. S. Rasband, and K. W. Eliceiri. Nih image to imagej: 25 years of image analysis. *Nature methods*, 9(7):671, 2012.

## Bibliography

---

- [146] M. Dreyer and P. Ho. Electro- and Stress-Migration in MLM Interconnect Structures. In S. Wilson and C. Tracy, editors, *Handbook of Multilevel Metallization for Integrated Circuits*. Noyes Publications, 1993.
- [147] I. Dutta and P. Kumar. Electric current induced liquid metal flow: Application to coating of micropatterned structures. *Applied Physics Letters*, 94(18):14–17, 2009.
- [148] P. Kumar, J. Howarth, and I. Dutta. Electric current induced flow of liquid metals: Mechanism and substrate-surface effects. *Journal of Applied Physics*, 115(4), 2014.
- [149] S. Talukder, N. Somaiah, and P. Kumar. Effect of substrate surface roughness on electric current induced flow of liquid metals. *Applied Physics Letters*, 102(5), 2013.
- [150] J. Black. Electromigration—A brief survey and some recent results. *Electron Devices, IEEE Transactions on*, 16(4):338–347, 1969.
- [151] D. Young and A. Christou. Failure mechanism models for electromigration. *IEEE Transactions on Reliability*, 43(2):186–192, 1994.
- [152] E. C. Miller. Corrosion of Materials by Liquid Metals. In R. N. Lyon, editor, *Liquid-Metals Handbook*, pages 144–183. US Government Printing Office, Washington D.C., 2 edition, 1952.
- [153] V. K. Andleigh, V. T. Srikar, Y. J. Park, and C. V. Thompson. Mechanism maps for electromigration-induced failure of metal and alloy interconnects. *Journal of Applied Physics*, 86(12):6737–6745, 1999.
- [154] B. Li, J. Gill, C. Christiansen, T. Sullivan, and P. McLaughlin. Impact of via-line contact on CU interconnect electromigration performance. In *2005 IEEE International Reliability Physics Symposium, 2005. Proceedings. 43rd Annual.*, pages 24–30, 2005.
- [155] C. K. Hu, L. Gignac, and R. Rosenberg. Electromigration of Cu/low dielectric constant interconnects. *Microelectronics Reliability*, 46(2-4):213–231, 2006.
- [156] B. K. Liew, N. W. Cheung, and C. Hu. Projecting Interconnect Electromigration Lifetime for Arbitrary Current Waveforms. *IEEE Transactions on Electron Devices*, 37(5):1343–1351, 1990.
- [157] V. Martinez, F. Stauffer, M. O. Adagunodo, C. Forro, J. Vörös, and A. Larmagnac. Stretchable Silver Nanowire–Elastomer Composite Microelectrodes with Tailored Electrical Properties. *ACS Applied Materials & Interfaces*, page 150611145631000, 2015.
- [158] S. P. Lacour, J. Jones, S. Wagner, T. Li, and Z. Suo. Stretchable Interconnects for Elastic Electronic Surfaces. *Proceedings of the IEEE*, 93(8):1459–1466, 2005.
- [159] G. D. Moon, G.-H. Lim, J. H. Song, M. Shin, T. Yu, B. Lim, and U. Jeong. Highly stretchable patterned gold electrodes made of Au nanosheets. *Advanced materials (Deerfield Beach, Fla.)*, 25(19):2707–12, 2013.

- 
- [160] K. Tybrandt and J. Vörös. Fast and Efficient Fabrication of Intrinsically Stretchable Multilayer Circuit Boards by Wax Pattern Assisted Filtration. *Small*, pages n/a–n/a, 2015.
- [161] H. O. Michaud, J. Teixidor, and S. P. Lacour. Soft flexion sensors integrating stretchable metal conductors on a silicone substrate for smart glove applications. In *2015 28th IEEE International Conference on Micro Electro Mechanical Systems (MEMS)*, pages 760–763, 2015.
- [162] A. P. Gerratt, H. O. Michaud, and S. P. Lacour. Elastomeric Electronic Skin for Prosthetic Tactile Sensation. *Advanced Functional Materials*, 25(15):2287–2295, 2015.
- [163] H. O. Michaud, L. Dejace, S. de Mulatier, and S. P. Lacour. Design and Functional Evaluation of an Epidermal Strain Sensing System for Hand Tracking. In *2016 IEEE/RSJ International Conference on Intelligent Robots and Systems (IROS)*, pages 3186–3191, 2016.
- [164] M. G. Catalano, G. Grioli, E. Farnioli, a. Serio, C. Piazza, and a. Bicchi. Adaptive synergies for the design and control of the Pisa/IIT SoftHand. *The International Journal of Robotics Research*, 33(5):768–782, 2014.
- [165] Z. Xu and E. Todorov. Design of a Highly Biomimetic Anthropomorphic Robotic Hand towards Artificial Limb Regeneration. In *Robotics and Automation (ICRA), 2016 IEEE International Conference on*, pages 3485–3492, 2016.
- [166] R. Deimel and O. Brock. A Novel Type of Compliant, Underactuated Robotic Hand for Dexterous Grasping. In *Robotics: Science and Systems*, 2014.
- [167] A. Schmitz, U. Pattacini, F. Nori, L. Natale, G. Metta, and G. Sandini. Design, realization and sensorization of a dextrous hand: the iCub design choices. In *Humanoid Robots (Humanoids), 2010 10th IEEE-RAS International Conference on*, pages 186–191, 2010.
- [168] M. M. A. Yajadda, K. H. Müller, and K. Ostrikov. Effect of Coulomb blockade, gold resistance, and thermal expansion on the electrical resistance of ultrathin gold films. *Physical Review B - Condensed Matter and Materials Physics*, 84(23):1–8, 2011.
- [169] F. Avilès, O. Ceh, and A. I. Oliva. Physical Properties of Au and Al Thin Films Measured by Resistive Heating. *Surface Review and Letters*, 12(1):101–106, 2005.
- [170] M. Mentzel, A. Benlic, N. J. Wachter, D. Gulkin, S. Bauknecht, and J. Gülke. The Dynamics of Motion Sequences of the Finger Joints during Fist Closure. *Handchir Mikrochir Plast Chir*, 43(3):147–154, 2011.
- [171] C. D. Metcalf, S. V. Notley, P. H. Chappell, J. H. Burridge, and V. T. Yule. Validation and application of a computational model for wrist and hand movements using surface markers. *IEEE Transactions on Biomedical Engineering*, 55(3):1199–1210, 2008.
- [172] M. C. Hume, H. Gellman, H. McKellop, and R. H. Brumfield. Functional range of motion of the joints of the hand. *Journal of Hand Surgery*, 15(2):240–243, 1990.

## Bibliography

---

- [173] D.-H. Kim, R. Ghaffari, N. Lu, S. Wang, S. P. Lee, H. Keum, R. D'Angelo, L. Klinker, Y. Su, C. Lu, Y.-S. Kim, A. Ameen, Y. Li, Y. Zhang, B. de Graff, Y.-Y. Hsu, Z. Liu, J. Ruskin, L. Xu, C. Lu, F. G. Omenetto, Y. Huang, M. Mansour, M. J. Slepian, and J. a. Rogers. Electronic sensor and actuator webs for large-area complex geometry cardiac mapping and therapy. *Proceedings of the National Academy of Sciences of the United States of America*, 109(49):19910–5, 2012.
- [174] C. Perry. Data-reduction algorithms for strain-gage rosette measurements. *Experimental Techniques*, 13(5):13–18, 1989.
- [175] K. Liu and B. Ju. A novel technique for mechanical characterization of thin elastomeric membrane. *Journal of Physics D: Applied Physics*, 91:L91–L94, 2001.
- [176] F. Cordella, A. L. Ciancio, R. Sacchetti, A. Davalli, A. G. Cutti, E. Guglielmelli, and L. Zollo. Literature Review on Needs of Upper Limb Prosthesis Users. *Frontiers in Neuroscience*, 10(May):1–14, 2016.
- [177] U. Wijk and I. Carlsson. Forearm amputees' views of prosthesis use and sensory feedback. *Journal of Hand Therapy*, 28(3):269–278, 2014.
- [178] C. Antfolk, A. Björkman, S.-O. Frank, F. Sebelius, G. Lundborg, and B. Rosen. Sensory feedback from a prosthetic hand based on air-mediated pressure from the hand to the forearm skin. *Journal of rehabilitation medicine : official journal of the UEMS European Board of Physical and Rehabilitation Medicine*, 44(8):702–7, 2012.
- [179] M. Anugolu, C. Potluri, A. Ilyas, P. Kumar, S. Chiu, N. Devine, A. Urfer, M. P. Schoen, and S. M. Ieee. A review on sensory feedback for sEMG based prosthetic hands. In *International Conference on Artificial Intelligence*, 2011.
- [180] J. Farserotu, J.-d. Decotignie, J. Baborowski, P. N. Volpe, C. Quiros, V. Kopta, C. Enz, S. P. Lacour, H. Michaud, R. Martuzzi, V. Koch, H. Huang, T. Li, and C. Antfolk. Tactile Prosthetics in WiseSkin. In *Proceedings of the 2015 Design, Automation & Test in Europe Conference & Exhibition (DATE 2015)*, volume 6, pages 1695–1697, 2015.
- [181] STMicroelectronics. LPS25H MEMS pressure sensor datasheet, 2016.
- [182] T. I. Inc. MSP430F552x, MSP430F551x Mixed-Signal Microcontrollers, 2015.
- [183] J. Jeong, J. G. Mccall, Y. Zhang, Y. Huang, M. R. Bruchas, and J. A. Rogers. Soft Microfluidic Neural Probes for Wireless Drug Delivery in Freely Behaving Mice. In *Solid-State Sensors, Actuators and Microsystems (TRANSDUCERS), 2015*, pages 2264–2267, 2015.
- [184] D. H. Kim, S. Wang, H. Keum, R. Ghaffari, Y. S. Kim, H. Tao, B. Panilaitis, M. Li, Z. Kang, F. Omenetto, Y. Huang, and J. a. Rogers. Thin, flexible sensors and actuators as 'instrumented' surgical sutures for targeted wound monitoring and therapy. *Small*, 8(21):3263–3268, 2012.

- [185] D. Maji, S. Member, and S. Das. Simulation and Feasibility Study of Flow Sensor on Flexible Polymer for Healthcare Application. *IEEE Transactions on Biomedical Engineering*, 60(12):3298–3305, 2013.
- [186] G. Canavese, S. Stassi, C. Fallauto, S. Corbellini, V. Cauda, V. Camarchia, M. Pirola, and C. F. Pirri. Piezoresistive flexible composite for robotic tactile applications. *Sensors and Actuators A: Physical*, 208:1–9, 2014.
- [187] A. Romeo, Q. Liu, Z. Suo, and S. P. Lacour. Elastomeric substrates with embedded stiff platforms for stretchable electronics. *Applied Physics Letters*, 102(13):131904, 2013.
- [188] J. R. Lloyd. Electromigration in integrated circuit conductors. *Journal of Physics D: Applied Physics*, 32(17):R109–R118, 1999.
- [189] S. P. Lacour. Stretchable thin-film electronics. In T. Someya, editor, *Stretchable Electronics*, pages 81–109. Wiley-VCH, 2012.
- [190] J. C. Sanchez. Semiconductor strain gauge, 1963. US Patent 3,084,300.
- [191] Z. Pataky, D. Grivon, Y. Civet, and Y. Perriard. Diabète Chaussures intelligentes pour patients diabétiques. *Revue Médicale Suisse*, 50:143–147, 2016.
- [192] R. Fan, M. Culjat, Chih-Hung King, M. Franco, R. Boryk, J. Bisley, E. Dutson, and W. Grundfest. A Haptic Feedback System for Lower-Limb Prostheses. *IEEE Transactions on Neural Systems and Rehabilitation Engineering*, 16(3):270–277, 2008.
- [193] Sof Robotics Inc.
- [194] R. V. Martinez, J. L. Branch, C. R. Fish, L. Jin, R. F. Shepherd, R. Nunes, Z. Suo, and G. M. Whitesides. Robotic tentacles with three-dimensional mobility based on flexible elastomers. *Advanced Materials*, 25(2):205–212, 2013.
- [195] V. Wall, Z. Gabriel, and O. Brock. A Method for Sensorizing Soft Actuators and Its Application to the RBO Hand 2. In *2017 IEEE International Conference on Robotics and Automation (ICRA)*, 2017.
- [196] H. Zhao, K. O’Brien, S. Li, and R. Shepherd. Optoelectronically Innervated Soft Prosthetic Hand via Stretchable Optical Waveguides. *Science Robotics*, 7529(December):1–10, 2016.
- [197] G. Cannata, M. Maggiali, G. Metta, and G. Sandini. An embedded artificial skin for humanoid robots. In *2008 IEEE International Conference on Multisensor Fusion and Integration for Intelligent Systems*, pages 434–438, 2008.
- [198] A. Chortos, J. Lim, J. W. To, M. Vosgueritchian, T. J. Dusseault, T.-H. Kim, S. Hwang, and Z. Bao. Highly stretchable transistors using a microcracked organic semiconductor. *Advanced Materials*, 26(25):4253–4259, 2014.

## Bibliography

---

- [199] J. Xu, S. Wang, G.-J. N. Wang, C. Zhu, S. Luo, L. Jin, X. Gu, S. Chen, V. R. Feig, J. W. To, et al. Highly stretchable polymer semiconductor films through the nanoconfinement effect. *Science*, 355(6320):59–64, 2017.
- [200] R. S. McGinnis, S. Patel, I. Silva, N. Mahadevan, S. DiCristofaro, E. Jortberg, M. Ceruolo, and A. J. Aranyosi. Skin mounted accelerometer system for measuring knee range of motion. In *Engineering in Medicine and Biology Society (EMBC), 2016 IEEE 38th Annual International Conference of the*, pages 5298–5302, 2016.
- [201] R. Verplancke, M. Cauwe, S. Van Put, E. C. Smits, R. Kusters, G. Van Heck, J. Van Den Brand, M. Murata, H. Ohmae, Y. Tomita, H. Nakata, J. Vanfleteren, and H. De Smet. Stretchable Passive Matrix LED Display with Thin-Film Based Interconnects. In *SID 2016 Digest*, pages 664–667, 2016.
- [202] J. H. Hong, J. M. Shin, G. M. Kim, H. Joo, G. S. Park, I. B. Hwang, M. W. Kim, W. S. Park, H. Y. Chu, and S. Kim. 9.1-inch stretchable AMOLED display based on LTPS technology. *Journal of the Society for Information Display*, 25(3):194–199, 2017.
- [203] Dupont. Dupont PE873 Stretchable Silver Conductor, 2014.
- [204] M. Varga. Eletronics Integration. In S. Schneegass and O. Amft, editors, *Smart Textiles*, pages 161–184. Springer International Publishing, 2017.
- [205] D. Xu, A. Tairyach, and I. A. Anderson. Where the rubber meets the hand: Unlocking the sensing potential of dielectric elastomers. *Journal of Polymer Science, Part B: Polymer Physics*, 54(4):465–472, 2016.
- [206] Parker Hannifin Corp. EAPS-50RT/100RT Electroactive Polymer Sensor Evaluation Kit Data Sheet, 2017.

# Glossary

**AC** alternative current.

**ADC** analog-to-digital converter.

**AFM** atomic force microscope.

**BLE** Bluetooth low energy.

**BSE** backscattered electron detector.

**CA** compressed air.

**CHUV** centre hospitalier universitaire vaudois.

**CMC** carpo metacarpal.

**CTE** coefficient of thermal expansion.

**DC** direct current.

**DIP** distal interphalangeal.

**DRG** dorsal root ganglia.

**EDS** energy dispersive spectroscopy.

**EGaIn** gallium indium eutectic.

**ET** Everhart-Thornley detector.

**FA** fast adapting mechanoreceptors.

**GF** gauge factor.

**MCP** metacarpo-phalangeal.

**MEMS** micro electromechanical systems.

## **Glossary**

---

**NW** nanoWire.

**PDMS** polydimethylsiloxane.

**PEDOT:PSS** poly(3,4-ethylenedioxythiophene) polystyrene sulfonate.

**PIP** proximal interphalangeal.

**POM** polyoxymethylene.

**PSS** polystyrene-4-sulfonate.

**PVD** physical vapor deposition.

**RMS** root mean square.

**ROM** range of motion.

**RT** room temperature.

**RTV** room temperature vulcanization rubber.

**SA** slow adapting mechanoreceptors.

**SEM** scanning electron microscope.

**TCR** thermal coefficient of resistance.

**VSI** vertical scanning interferometry.

**XRD** X-ray diffraction.



# Hadrien Michaud

*PhD candidate in Microengineering at EPFL*

Rue de Lyon, 33

1201 Geneva

Switzerland

☎ +41 76 291 98 27

✉ hadrien.michaud@epfl.ch

---

## Education

- 2013–Present **EPFL**, *Graduate student in Microengineering.*
- 2011–2013 **EPFL**, *Master of Science in Microengineering.*
- 2008–2011 **École Polytechnique**, *Diploma in Electrical Engineering*, Palaiseau, France.
- 2006–2008 **Lycée du Parc**, *Intensive undergraduate program*, Lyon, France.

---

## Research projects

- 07.2013–Present **EPFL**, *Doctoral researcher*, Laboratory for Soft Bioelectronic Interfaces.  
Development of stretchable metallization technologies for skin-like transducers, supervised by Prof. Stéphanie Lacour.
- 09.2012–03.2013 **CERN**, *Master thesis*, Geneva, Switzerland.  
Conception and realisation of a microfabrication process to integrate and characterize 3D electrical contacts in silicon interposers for future particle detectors
- 04.2011–07.2011 **CEA-Leti**, *Research intern*, Grenoble, France.  
Characterization of piezoelectric micro-actuators for a technology transfer project to the industry.

---

## Honors and awards

- 2016 Second prize - iMatSci contest for innovation in material science - Phoenix, AZ, USA.
- 2016 Best poster award (3<sup>rd</sup> prize) - nano-tera annual meeting - Lausanne, Switzerland
- 2015 Finalist of nano-tera NextStep entrepreneurial coaching program. 3750 CHF cash prize to attend IDTech Wearable USA business fair.
- 2011-2013 EPFL Excellence Scholarship.
- 2012 Winning team, Lab-in-Tube competition organized by Prof. Stéphanie Lacour.
- 2011 Distinction for research internship, École Polytechnique Physics Department.

---

## Teaching

- 2014–2017 **Electronics II**, *Teaching assistant for exercise sessions, electronics course for 2<sup>nd</sup> year engineering bachelor students. p-n junction, diode, bipolar transistor, current sources, amplifier circuits*, 4 semesters, EPFL.
- 2014–2016 **Electronics II**, *Teaching assistant for laboratory sessions, electronics course for 2<sup>nd</sup> year engineering bachelor students. p-n junction, diode, bipolar transistor, current sources, amplifier circuits*, 3 semesters, EPFL.

- 2012–2012 **General Physics I**, *Teaching assistant for exercise sessions, physics course for 1<sup>st</sup> year engineering bachelor students*, 1 semester, EPFL.
- 2011–2011 **Analysis I**, *Teaching assistant for exercise sessions, analysis course for 1<sup>st</sup> year engineering bachelor students*, 1 semester, EPFL.

---

## Supervised projects

- 2017 **Vias and soft-rigid interfaces for stretchable wearable electronics**, Carlos Nunez Lopez (bioengineering), Master thesis.
- 2016 **Ultra-stretchable strain sensors for soft robotic hands**, Carlos Sanz Caldero (mechanical engineering), Semester project.
- 2015 **Fabrication and characterization of soft strain sensor for finger’s movement analysis**, Séverine de Mulatier (material science), Master thesis.
- 2015 **Additive manufacturing for large scale electronic skin**, Laurent Dejace (material science), Master thesis.
- 2014 **Fabrication and characterization of stretchable conductors based on gold thin films and liquid metal**, Joan Teixidor (microengineering), Semester project.

---

## Publications

### Patent

A. Hirsch, H. O. Michaud, I. R. Minev, and S. P. Lacour, “Method for manufacturing electrical conductors, and electrical conductors manufactured according to same,” EP Patent EP 15 19 2402, 2015.

### Journal articles

A. Hirsch\*, H. O. Michaud\*, A. P. Gerratt, S. De Mulatier, and S. P. Lacour, “Intrinsically Stretchable Biphasic (Solid–Liquid) Thin Metal Films,” *Advanced Materials*, vol. 28, no. 22, pp. 4507–4512, 2016.

A. P. Gerratt\*, H. O. Michaud, and S. P. Lacour, “Elastomeric electronic skin for prosthetic tactile sensation,” *Advanced Functional Materials*, vol. 25, no. 15, pp. 2287–2295, 2015.

H. O. Michaud\*, J. Teixidor, and S. P. Lacour, “Soft metal constructs for large strain sensor membrane,” *Smart Materials and Structures*, vol. 24, no. 3, p. 035020, 2015.

F. Casset\*, H. Michaud, T. Ricart, G. Le Rhun, M. Cueff, J. Abergel, P. Ancey, D. Faralli, A. Devos, S. Fanget *et al.*, “Optimization of electrodes design for PZT thin-film actuated membranes,” *Procedia Engineering*, vol. 47, pp. 108–111, 2012.

### Articles in conference proceedings

H. O. Michaud\*, L. Dejace, S. De Mulatier, and S. P. Lacour, “Design and functional evaluation of an epidermal strain sensing system for hand tracking,” in *Intelligent Robots and Systems (IROS), 2016 IEEE/RSJ International Conference on*. IEEE, 2016, pp. 3186–3191.

H. O. Michaud\*, J. Teixidor, and S. P. Lacour, “Soft flexion sensors integrating stretchable metal conductors on a silicone substrate for smart glove applications,”

in *2015 28th IEEE International Conference on Micro Electro Mechanical Systems (MEMS)*. IEEE, 2015, pp. 760–763.

J. Farserotu\*, J.-d. Decotignie, J. Baborowski, P. N. Volpe, C. Quiros, V. Kopta, C. Enz, S. P. Lacour, H. Michaud, R. Martuzzi, V. Koch, H. Huang, T. Li, and C. Antfolk, “Tactile Prosthetics in WiseSkin,” in *Proceedings of the 2015 Design, Automation & Test in Europe Conference & Exhibition (DATE 2015)*, vol. 6, 2015, pp. 1695–1697.

J. Abergel\*, M. Allain, H. Michaud, M. Cueff, T. Ricart, C. Dieppedale, G. Le Rhun, D. Faralli, S. Fanget, and E. Defay, “Optimized gradient-free PZT thin films for micro-actuators,” in *2012 IEEE International Ultrasonics Symposium*. IEEE, 2012, pp. 972–974.

### **Oral presentations**

H. O. Michaud\*, A. Hirsch, S. De Mulatier, A. P. Gerratt, and S. P. Lacour, “Liquid-solid gold-gallium thin films for high performance micro-structured stretchable interconnects and sensors,” in *2016 MRS Spring Meeting*, march 2016.

A. P. Gerratt\*, H. O. Michaud, and S. P. Lacour, “Stretchable electronic skin based on distributed flexion and pressure sensors mounted on a textile glove,” in *2015 MRS Spring Meeting*, april 2015.

G. Le Rhun, J. Abergel, M. Allain, H. Michaud, M. Cueff, T. Ricart, C. Dieppedale, A. Suhm, L. Colombo, D. Faralli, M. Fusi, P. Ferrarini, S. Fanget, and E. Defaÿ, “Optimized gradient-free PZT films for micro-actuators on 200mm silicon wafers,” in *3rd International PiezoMEMS Workshop, PiezoMEMS 2013*, april 2013.

J. Abergel\*, M. Cueff, H. Michaud, M. Allain, T. Ricart, C. Dieppedale, A. Suhm, R. Kessels, S. Tiedke, G. Le Rhun, S. Fanget, M. Aid, , and E. Defaÿ, “Direct and indirect piezoelectric characterization of PZT thin films for MEMS applications,” in *2nd International Workshop on Piezoelectric MEMS, PiezoMEMS 2011*, september 2011.

